GRAPHENE-SUPPORTED ULTRATHIN TWO-DIMENSIONAL MATERIALS AND THEIR APPLICATIONS

NG Sze Wing

PhD

The Hong Kong Polytechnic University

2019

The Hong Kong Polytechnic University

Institute of Textiles and Clothing

GRAPHENE-SUPPORTED ULTRATHIN TWO-DIMENSIONAL MATERIALS AND THEIR APPLICATIONS

NG Sze Wing

A Thesis Submitted in Partial Fulfillment of the

Requirements for the Degree of Doctor of Philosophy

June 2018

Certificate of Originality

I hereby declare that this thesis is my own work and that, to the best of my knowledge and belief, it reproduces no material previously published or written, nor material that has been accepted for the award of any other degree or diploma, except where due acknowledgement has been made in the text.

______________________________ *(Signed)*

Sze-Wing NG

June 2018

To my parents and friends for their endless support.

ABSTRACT

The flexible and wearable technology has attracted tremendous attention from research field and commercial market in recent years. To ensure the users comfort, wearable devices are preferable to be lightweight and thin, and they are more likely to be built or attached to relatively soft and rough substrates, such as polymeric films, textiles and papers. Unfortunately, most of these flexible materials would deform under high temperature, be contaminated or damaged during chemical treatments. Therefore, two-dimensional (2D) transferrable and functional materials are important for building up the wearable electronics nowadays. Starting from 2004, there has been a number of reports on transferring mono-to-few layers graphene films on different electronic devices as flexible electrodes. Also, functional graphene surface with specific biological and chemical reactivity have been tailor-made via various modifications.

This thesis focuses on describing several approaches to fabricate polymer-free transferable, ultrathin and flexible graphene-supported 2D materials. The statement of challenges and objectives of this research is presented in the beginning, followed by a comprehensive literature review on graphene properties and preparation methods, and the modifications that have been done on graphene as well as their applications. For the content about the experiments in this research project, Chapter 4 introduces the grafting of polymer brushes on graphene surface via non-covalent interaction and their application on surface wettability control and biomolecules immobilization. Chapter 5 states the graphene-assisted gold (Au) film transfer and detail characterization of the graphene-mediated grown gold layers. Chapter 6 describes the patterning and transfer processes of the Au@graphene (Au@G) films with their application on photovoltaic devices. Chapter 7 discusses the fabrication and transfer of graphene-supported metal oxide layer, and the micro-supercapacitor supported by the metal oxide@graphene bilayer. Finally, Chapter 8 provides conclusions and future outlooks.

Firstly, by adopting a pyrene-group bearing initiator which interacts with graphene basal plane non-covalently through π-π interaction, four kinds of polymer brushes with distinct functionalities were grafted on the chemical vapor deposited (CVD) graphene via self-initiated atomic transfer radical polymerization (SI-ATRP). Copolymer designed with desired functional group with pyrene group as termini was also synthesized and successfully anchored on graphene surface. These fabricated polymer@graphene 2D objects are transparent, flexible, transferrable on various substrates with good stability, and are patternable into different structures.

Secondly, ultrathin Au films with various thicknesses were thermally deposited on CVD graphene. The ultrathin Au@G films are transferable without protection and achieve relatively high smoothness and mechanical stability when compared with pure Au films. An unexpected hcp phase Au structure was also discovered from the graphene-mediated grown Au layer. These extraordinary behaviors of graphene-supported Au films were discussed with density functional theory (DFT) stimulation results. Moreover, Au@G meshes were fabricated in aids with photolithography. As the Au@G meshes could be patterned with high optical transmittance and possessed high flexibility, they were integrated in organic solar cells as the top electrode.

Moreover, the growth and wet-transfer of metal oxide layers with graphene support were demonstrated. This is the first report on transferable silicon dioxide (SiO_2) layer fabricated through plasma-enhanced chemical vapor deposition (PECVD) on CVD graphene. The resulted SiO_2@graphene films were found to be highly transparent, thus making it an ideal ultra-thin insulating building block for transferable, transparent thin-film electronics. A planar micro-supercapacitor was built on these SiO_2/graphene bilayers and was transferred on various substrates with good stability and flexibility.

In conclusion, ultrathin graphene-supported functional organic layers, graphene-supported metal and metal oxide layers were fabricated. Given that these three kinds of graphene-supported ultrathin materials all have their own distinctive properties and functions, the work presented here is expected to have significant impact on physical, chemical, material, biological and engineering fields.

LIST OF PUBLICATIONS

Related Journal Publications

1. **Sze-Wing Ng,** Nuruzzaman Noor , Zijian Zheng, "Graphene-based two-dimensional Janus materials.", *NPG Asia Materials*, 2018, 1.

2. Tingting Gao†, **Sze-Wing Ng**†, Xuqing Liu, Liyong Niu, Zhuang Xie, Ruisheng Guo, Chaojian Chen, Xuechang Zhou, Jun Ma, Wei Jin, Ying-San Chui, Wenjun Zhang, Feng Zhou, Zijian Zheng, "Transferable, transparent and functional polymer@graphene 2D objects" *NPG Asia Materials*, 2014, 6.9: e130. († equal contribution)

Papers in preparation

1. **Sze-Wing Ng**, Mingzi Sun, Guangming Zhao, Yaokang Zhang, Matthew Daly, Horacio D. Espinosa, Ye Zhu, Bolong Huang, Zijian Zheng, "Graphene mediated electron-epitaxial growth of ultrathin Gold layers"
2. **Sze-Wing Ng**, Yaokang Zhang, Zijian Zheng, "Graphene-supported Gold transfer for optoelectronics"
3. **Sze-Wing Ng**, Hao Yu, Yaokang Zhang, Hang Zhou, Zijian Zheng, "Ultrathin, flexible and transferable graphene-supported mirco-supercapacitor"

Conference Presentations

Oral presentation:

"Transferable, Transparent and Functional Polymer@Graphene 2D Objects", The 2nd International Conference on Advances in Functional Materials 2016 (AFM 2016), August 8 - 11th, 2016, ICC Jeju, Jeju, Korea.

Poster presentation:

1. **Sze-Wing Ng**, Tingting Gao, and Zijian Zheng, "Transferable, Transparent and Functional Polymer@Graphene 2D Objects", Young Giants of Nanoscience 2016, 29th, May – 2nd, June, 2016, The Hong Kong Polytechnic University, Hong Kong SAR.

2. **Sze-Wing Ng**, Tingting Gao, and Zijian Zheng, "Transferable, Transparent and Functional Polymer@Graphene 2D Objects", The 2nd International Conference on Two-Dimensional Layered Materials (2DLM 2016), 7 – 9th, Jan, 2016, The Hong Kong Polytechnic University, Hong Kong SAR.

Awards

Outstanding Poster Award, Sze-Wing Ng, Tingting Gao, and Zijian Zheng, "Transferable, Transparent and Functional Polymer@Graphene 2D Objects", Young Giants of Nanoscience 2016, 29th, May – 2nd, June, 2016, The Hong Kong Polytechnic University, Hong Kong SAR.

ACKNOWLEDGEMENTS

I would like to express my greatest gratitude to my project supervisor, Prof. Zijian Zheng, for giving me the opportunity to join his research group. I feel so grateful for all his caring and support, his constant guidance and priceless encouragements given on both my research work and attitude. Everything he has taught me is the treasure that I will carry throughout my life's journey, like the way of thinking, planning, adjusting the mindset and even the way of communicating with different people. I am extremely grateful to have such a brilliant, enthusiastic and inspiring supervisor.

I would also like to acknowledge my colleagues in Prof. Zheng's group who are very supportive and passionate during these 4 years: Dr. Xuechang Zhou, Dr. Zhilu Liu, Dr. Ruisheng Guo, Dr. Tingting Gao, Dr. You Yu, Dr. Hongyu Zhen, Dr. Zhuang Xie, Dr. Liyong Niu, Dr. Lina Chen, Dr. Yu Yang, Dr. Jian Chang, Dr. Guoqiang Liu, Dr. Ting Xiao, Dr. Dongrui Wang, Dr. Dongdong Chen, Dr. Zhongwei Wu, Dr. Lei Yao, Dr. Qi Gan, Dr. Zhijun Ma, Dr. Yaokang Zhang, Mr. Chaojian Chen, Ms. Kate Yip, Ms. Casey Yan, Mr. Xiang Xiao, Ms. Younseon Wang, Ms. Qiyao Huang, Mr. Shuaichen Wang, Mr. Peng Li, Mr. Xi Lu, Mr. Jian Shang, Ms. Yujing Zhu and Mr. Chuan Xie. They have always been reliable partners and sincere friends. In the meantime, I would like to thank my coworkers, Dr. Ye Zhu and Mr. Guangming Zhao in the Department of Applied Physics, and Dr. Bolong Huang and Ms. Mingzi Sun in Department of Applied Biology and Chemical Technology; Prof. Hang Zhou and Dr. Hao Yu from Thin Film Transistor and Advanced Display Lab in Peking University Shenzhen Graduate School, and Prof. Horacio D. Espinosa and Dr. Matthew Daly from Department of Mechanical Engineering in Northwestern University. I also gratefully acknowledge the financial support from the Hong Kong Polytechnic University (1-ZVK1).

Moreover, I would like to express my deep gratitude to my parents for their love, understanding and endless support. Also, I want to thank my dearest friends. The postgraduate study was always tough and frustrating in these 4 years, but at least I can relax a bit and face the challenges positively with their company.

TABLE OF CONTENTS

CHAPTER 1 INTRODUCTION

CHAPTER 2 LITERATURE REVIEW

CHAPTER 3 METHODOLOGY

CHAPTER 4 GRAPHENE-SUPPORTED UNLTRATHIN FUNCTIONAL POLYMER FILMS

CHAPTER 5 GRAPHENE MEDIATED GROWTH AND TRANSFER OF ULTRATHIN GOLD LAYERS

CHAPTER 6 GRAPHENE-BASED FLEXIBLE AND TRANSPARENT ELECTRODES

CHAPTER 7 ULTRATHIN, FLEXIBLE, TRANSFERABLE GRAPHENE-SUPPORTED MICRO-SUPERCAPACITOR

CHAPTER 8 CONCLUSIONS AND OUTLOOK

LIST OF FIGURES

Figure 2.4 Schematic illustration showing covalent surface modifications of graphene with diazonium salts. **a)** (Top) Spontaneous grafting of aryl groups to graphene basal plane via reduction of 4-nitrophenyl diazonium (NPD) tetrafluoroborate. (Bottom) FTIR spectrum of NP-functionalized graphene. **b**) Single-side and two-side aryl diazonium functionalization on monolayer and bilayer graphene film.

Figure 2.5 Modifications of graphene film via polymer grafting. **a)** Transmittance spectra of the graphene modified by PBASE. Inset: schematic diagram. **b)** Combined UPS and IPES spectra, **c)** and **d)** XPS C 1s and N 1s core-level spectra of PBASE modified graphene, respectively. **e)** Thermosensitive graphene nanocomposites formed using pyrene-terminal polymers made by RAFT polymerization.

Figure 2.6 Asymmetrically modified-graphene decorated with metal and metal oxide nano-particles. **a)** Schematic diagram showing the fabrication procedure of the asymmetrical functionalized graphene film with ZnO and Au NPs. **b)** (i-iii) Deposition procedure of spherical ZnO NPs and cubic Au NPs on patterned graphene sheets. iv) AFM image showing the selective attachment of ZnO NPs on plasma-treated area of graphene sheet. v) AFM and vi) TEM images showing the ZnO NPs deposited in the plasma treated area, and the large cubic Au NPs with small spherical ones attached in the ZnO/plasma-free region of the modified graphene sheet. Scale bars: iv) 1 mm; v) 2 mm; vi) 100 nm.

Figure 2.7 Patterning on fluorinated graphene (FG) film via large-area ink-jet printing method. **a)** Schematic diagram of depositing PDMS barriers on graphene films through direct inkjet printing. **b)** Microscopic image of patterned PDMS barrier on a FG film (scale bar = 50 μm). The aligned growth of stem cells on **c)** unmodified graphene, **d)** partially fluorinated graphene and **e)** fluorinated graphene with PDMS barriers prtined on top (scale bar = 100 μm). **f & g)** Microscopic image of MSCs attached on the FG strips, with their F-actin aligned (red) and expressing neural specific markers—Tuj1 and MAP2 (green) (scale bar = 50 μm). **h)** The percentage of immune-reactive cells for

Tuj1 and MAP2 on unpatterned and patterned FG strips. The patterned FG strips induced a higher expression of Tuj1 and MAP2 in the absence of retinoic acid. ($n = 6$, $p < 0.05$)

Figure 2.8 GNM FET biosensor. **a)** Schematic diagram of the fabricating procedure of the GNM FET biosensor. **b)** Digital image of a GNM FET biosensor built on a thin and flexible PDMS substrate attached on human skin. Enlarged view is the corresponding structure of the biosensor. **c)** Transfer characteristics of a solution gated GNM FET biosensor in response to HER2 protein concentrations ranging from 0.0001 to 200 ng ml^{-1}. The V_d is set at a fixed value of −0.1 V. **d)** Magnified curve of (c) in the Vg range of −0.2 to 0.1 V. **e)** Current change (ΔI_d, HER2) versus HER2 concentration (CHER2). The error bars present the standard deviations of three measurements.

Figure 2.9 a) SEM image showing the cross-section of the rGO film (scale bar: 1 μm). **b)** schematic diagram of the asymmetric plasma treatments on the rGO film with hexane and oxygen. Insets: the surface wettability of the corresponding face after treatment. The water contact angles for the hexane plasma treated side is 90°, while that for the oxygen plasma treated side is 15°. **c)** The curvature change of the asymmetrically-modified rGO strip as a function of applied CV potential within ±1.2 V. Insets: digital images showing the status of the rGO strip when the applied potential was 1.2, 0, and 1.2 V, respectively.

Figure 2.10 Schematic diagram showing different common routes for functional graphene-based 2D objects.

Figure 3.1 Structural characterization of thin film by X-ray diffraction (XRD).

Figure 4.1 a) Schematic diagram of the fabrication and transfer process of polymer brushes@ CVD graphene objects. **b)** Chemical structures of the macro-initiator and polymer brushes.

Figure 4.2 Digital images of transferred PMMA@G objects on different substartes, including **a)** SiO_2 wafer; **b)** cotton fabric; **c)** Au wafer and **d)** PTFE film.

Figure 4.3 Characteristics of polymer brushes@G films transferred on SiO_2 substrate. **a)** ATR-FTIR spectrum, **b)** Raman spectrum and **c)** graph showing thickness and roughness of the series of polymer brushes@G films transferred on SiO_2 substrate. **d)** Transmittance of light of the series of polymer brushes@G films transferred on 125 μm PET substrate.

Figure 4.4 Optical images of **a)** PMMA@G and **b)** PGMA@G films t, **c)** PMETAC@G film transferred onto Au coated Si wafer, and **d)** POEGMA@G film ransferred on SiO_2 wafer. Insets: water contact angle of the corresponding samples.

Figure 4.5 a-b) Optical images and **c)** AFM images of patterned PMMA@CVD graphene films transferred on Si substrate.

Figure 4.6 a & b) Fluorescent microscopic images of the fluorescence intensity of 5'-NH2, 3'-TET-modified ss-DNA bounded with PGMA@G with **c)** the corresponding cross-section analysis. **d & e)** Fluorescent microscope images of fluorescence intensity after hybridization with 5'-TAMRA-labeled complementary probes with **f)** the corresponding cross-section analysis. (The inserted scale bars equal to 200 μm.) **g)** Molecular structure illustration of the DNA binding and hybridization process on the layer of PGMA brushes. **h)** Microscope image of immobilized DNA arrays on the surface of PGMA@G film transferred on a 125 μm PET substrate.

Figure 4.7 Schematic diagram of the fabrication and transfer process of copolymer@ CVD graphene films.

Figure 5.5 TEM analysis of Au@CVD graphene film. **a & b)** TEM images of ~10nm thick Au@CVD graphene film. **c)** HRTEM image of a small region of the Au@CVD graphene film along [100] zone axis, as indicated in the SAED in **d)**. **d)** SAED pattern of the Au, showing diffraction rings for the Au layer along [100] zone axis. **e)** Model of the atomic arrangement of hcp structure corresponding to **c)**.

Figure 5.6 XRD patterns of **a)** 10 nm, **b)** 20 nm, **c)** 50 nm, and **d)**100nm Au layers directly deposited on Si substrates, wet-transferred on Si wafer with and without CVD graphene support.

Figure 5.7 a) Sheet resistance changes of Au films (with and without CVD graphene support) transferred on 125 μm PET substrates within 10000 bending cycles with a bending radius of 2.5 mm. Microscopic images of 100 nm Au film **b)** with and **c)**without graphene support captured after 10000 bending cycles. SEM images of 20 nm Au films **d)** with and **e)** without graphene support taken after 10000 bending cycles. All the bending cycles consisted with a bending radius of 2.5 mm.

Figure 5.8 Local view of even layers and odd layers of Cu-Graphene-Au multilayer structures.

Figure 5.9 a) Formation energies of different number of layers. **b)** Comparison PDOS of Au atoms in odd layers and even layers structured films.

Figure 5.10 PDOS of all Au atoms on Layer 6.

Figure 5.11 PDOS of all Au atoms on Layer 5.

Figure 5.12 Schematic diagram of Au atoms growth on graphene.

Figure 7.3 a) Corresponding plot showing the relationship of areal capacitance of the electrode versus the electochemical deposition time of MnO_2. **b)** CV curves of the electrode at 80 s-MnO_2-deposition at different scan rates. SEM images of the deposited MnO_2 layer on top of patterned Au electrodes with different electochemical deposition time: **c)** 5 s, **d)** 50 s and **e)** 150 s, and the exposed SiO_2 area in between the electrode fingers. All scale bars equal to 500μm .

Figure 7.4 CV curves of the micro-supercapacitor at different scan rates **a)** 10 mV s^{-1} to 500 mV s^{-1}, and **b)** 1 V s^{-1} to 20 V s^{-1}. **c)** GCD curves of the supercapacitor device with different current densities (0.02 mA cm^{-2} to 0.2mA cm^{-2}). **d)** Nyquist plot of the micro-supercapacitor. **f)** Cycling performance of the device during 8000 cycles at a scan rate of 0.02 mA cm^{-2}.

Figure 7.5 CV curves of the finer micro-supercapacitor at different scan rates **a)** 10 mV s^{-1} to 500 mV s^{-1}, and **b)** 1 V s^{-1} to 50 V s^{-1}. **c)** GCD curves of the supercapacitor device with different current densities (0.08 mA cm^{-2} to 0.4mA cm^{-2}). **d)** Nyquist plot of the micro-supercapacitor.

Figure 7.6 Digital images of μSCs transferred onto **a)** PI tape, **b)** cotton fabric and **c)** A4 paper. **d)** SEM image of μSC transferred onto PI tape. **e)** Digital image of the bent μSC on PI tape and **f)** CV curves of the μSC on PI tape at flat and bending state.

LIST OF TABLES

LIST OF ABBREVIATIONS

AFM	Atomic force microscope
ATR-FTIR	Attenuated total reflectance Fourier transform infrared spectroscopy
ATRP	Atom transfer radical polymerization
CVD	Chemical vapor deposition
DCM	Dichloromethane
DFT	Density functional theory
DMF	Dimethylformamide
DMSO	Dimethyl sulfoxide
ELD	Electroless deposition
FRET	Forster resonance energy transfer
GO	Graphite oxide
HRTEM	High-resolution transmission electron microscopy
ITO	Indium tin oxide
LED	Light-emitting diode
μSC	Micro-supercapacitor
P3HT	Poly(3-hexylthiophene-2,5-diyl)
PCBM	[6,6]-phenyl-C_{61}-butyric acid methyl ester
PCE	Power conversion efficiency
PDMS	Polydimethylsiloxane
PDOS	Partial density of states
PECVD	Plasma-enhanced chemical vapor deposition
PEDOT: PSS	Poly(3,4-ethylenedioxythiophene): Polystyrene sulfonate
PEI	Polyethylenimide
PET	Poly (ethylene terephthalate)
PGMA	Poly (glycidyl methacrylate)
PI	Polyimide

PMETAC	poly[(2-(methylacryloyloxyl)ethyl) trimethylammonium
PMMA	poly (methyl methacrylate)
POEGMA	poly(oligo(ethyleneglycol) methacrylate)
PPMA-PMETAC	poly (1-pyrenemethylmethacrylate)-poly[2-(methacryloyloxy)ethyltrimethyl- ammonium chloride]
PTFE	Polytetrafluoroethylene
SAED	Selected area electron diffraction
SEM	Scanning electron microscopy
SI-ATRP	Self-initiated atomic transfer radical polymerization
SPM	Scanning probe microscope
TAMRA-cDNA	5’-TAMRA-labeled complementary DNA oligonucleotide
TEM	Transmission electron microscopy
TET-ssDNA	5’-amino-modified, 3’-TET-labeled single strand DNA oligonucleotides
TRT	Thermal release tape
UV-Vis	Ultraviolet-visible spectroscopy
XPS	X-ray photoelectron spectroscopy
XRD	X-ray diffraction

CHAPTER 1 INTRODUCTION

1.1 Background and challenges

The emerging interest of flexible and wearable technology has dominated the research field and commercial market in past decades. Numerous attempts have been made for fabricating flexible electronics such as sensors, display devices and portable energy storage devices. Instead of the currently adopted rigid building blocks such as glass or other silicon-based substrates, soft materials like very thin plastic films, textiles or even papers are required as supporting materials for the next generation electronics. Unfortunately, there were large obstacles on the fabrication process while adopting these flexible materials as device building block – they would lose their flexibly due to deformation under high temperature, which is always involved in physical vacuum deposition process of metal electrodes; or damaged by acidic environment or solvents during the solution-process functionalization. In this situation, mechanical transfer of functional layers or whole devices is the only solution for building the electronics on flexible but fragile materials. However, conventional transfer printing technology always required flat and rigid substrates as the transferred components were pressed onto them via external force, or specific chemical interactions. Hence, it is highly essential to fabricate transferrable, functional two-dimensional (2D) materials and develop a transfer technology to integrate the thin-film components onto arbitrary flexible substrates.

Among the state of art technology, mono-to-few layer graphene film is one of the most promising flexible and ultrathin two-dimensional (2D) materials. Ever since the first electrical measurement of monolayer graphene was published in 2004[1], graphene has been a rapid rising star in the field. The graphene layer is now well known for its one-atomic-thick structure composed with sp^2 carbon atoms hexagonally arranged into a honeycomb lattice. More importantly, it was found to possess a series of fascinating behaviors in different aspect, including its extraordinary high mechanical strength, flexibility, optical transparency, and electrical and thermal conductivity[2-5]. Under the protection of a spin-coated polymeric layer or few-ten-nanometer metal layer, a complete graphene film could be transferred onto various substrates and electronic devices as electrodes.[6-9]

However, the chemical inertness of graphene lamentably leads to an obstacle for incorporating graphene films into devices or matrices in sensing and actuating areas, which requires biochemical sensitivities and reactivity. There is no functional group on pure graphene surface; surface modifications are therefore necessary for introducing specific functional groups on the graphene basal plane. Scientists have investigated numerous surface modifications on graphene; and modified-graphene layer with specific biological and chemical reactivity has been tailor-made via grafting different small molecules and polymers on the graphene surface[10-14]. However, plenty of the modifying strategies depend on the covalent bond formation in between the foreign molecules and graphene film, which would damage the conjugation of the basal plane and sacrifice the electronic merits of graphene. For this reason, a versatile modifying strategy, which allows the grafting of a wide range of functional groups onto the graphene films via non-covalent modification, is largely demanded. To avoid any further protection coated on top of the functional layer which will lead to further cleansing process, the grafted organic layer should also be dense enough to protect the supporting graphene film.

From an electronics point of view, pristine graphene film was not applicable to all kinds of electronic devices as, for example, the zero-bandgap structure always avoids applying graphene as logic circuits components such as transistor. [15-17]. The relatively low conductivity of graphene also limited the performance of devices that were fabricated with pristine graphene as electrode, when compared with other flexible conductive materials such as the conductive polymer and metal nanowire networks[18-20]. In this situation, instead of pristine graphene film, transferable and highly conductive graphene-supported 2D materials are preferable as the electrodes for high-performance electronic devices. In addition to transferable functional and conductive thin films, transferable graphene-supported devices are the goal for integrating the electronics on the daily-wear materials.

1.2 Research objectives

This study focuses on the fabrication of transferrable and highly flexible graphene-supported ultrathin 2D materials via non-covalent approaches. In detail, the objectives are listed as follows:

1. To fabricate graphene-supported ultrathin functional polymer films via non-covalent interaction between graphene basal plane and pyrene-group bearing initiator for polymerization.
2. To fabricate graphene-supported metal thin film and metal mesh via physical deposition.
3. To characterize the graphene-supported metal in detail after transfer process and do comparisons between pure metal film and the graphene-mediated grown metal layer.
4. To fabricate a graphene-based transparent building block for transferrable devices by depositing ultra-thin, dense and flat protective layer on graphene.

1.3 Research originality

In this research project, all the fabricated ultrathin 2D materials were grown on and supported by mono-to-few layer graphene films. The main originality associated with the studies is the graphene-assisted transfer technology, which opened the avenue of attaching quasi, flexible and ultrathin 2D materials on arbitrary substrates, including the functional organic layers, metal and metal oxide layers, as well as ultrathin electronic devices.

At first, investigations have been performed on the graphene-supported functional organic films, which introduced the chemistry and methodology for grafting polymer brushes on graphene sheets via non-covalent interaction. This approach enabled a robust route for fabricating ultrathin, transferable functional 2D organic materials when compared with the conventional methods. As various kinds of polymer brushes with different functional groups possess unique properties, the graphene supported organic layer could be tailor made for specific reactivity-required applications.

Furthermore, via the simple thermal deposition of Au layer on CVD graphene film, it came to the first discovery that the Au layer with hcp phase could be achieved by graphene-mediated growth; such Au layers supported by graphene films could be patterned and transferred onto various target substrates without any protection on top. Good flexibility with satisfactory conductivity makes them very suitable for being applied as electrodes for flexible electronics.

This study also contributes to the first discovery of wet-transferable ultrathin silicon dioxide/graphene bilayer (< 25 nm), as well as the first wet-transfer of micro-supercapacitor (< 150 nm) adopting the bilayer as basal material. The silicon dioxide/graphene bilayer obtains a high transmittance of visible light region and attaches well on various substrates such as papers, textiles and polymeric films. As a result, it is a promising building block for semitransparent or transparent electronics.

1.4 Outline of the thesis

Chapter 1 introduces the importance of transfer technology for thin-film materials, the background of graphene, and current challenges of applying graphene in various aspects. The research objectives and the original contributions of the study are also stated.

Chapter 2 gives a brief introduction to the properties and fabrication process of graphene and its derivatives, and the surface modifications, including the covalent and non-covalent ones, which have been done on the graphene-based materials based on different objectives.

Chapter 3 elaborates the methodology of this research project, including the materials, general wet-transfer process of graphene-supported 2D materials, and adopted characterization techniques.

Chapter 4 includes the chemistry and results of polymer brushes grafted on the top side of CVD graphene film via non-covalent π-π interaction, as well as the application of polymer brushes grafted graphene film on surface wettability control and biomolecules immobilization.

Chapter 5 discusses the graphene-assisted Au layers transfer. The morphology, mechanical stability and crystallographic structure of the thermal-deposited Au layer on CVD graphene were studied. In addition, the mechanism of the unique graphene-mediated Au growth was elaborated through stimulation results.

Chapter 6 reports the fabrication of patterned Au@graphene films via photolithography; their application as flexible and transferable electrode for optoelectronic was demonstrated.

Chapter 7 demonstrates the first wet-transfer of silicon dioxide (SiO_2) layer on arbitrary substrates via mono-to-few-layer graphene support, and the fabrication and transfer of an ultrathin micro-supercapacitor supported by such SiO_2@graphene bilayer.

Lastly, Chapter 8 concludes the whole research project, with some future outlooks suggested.

CHAPTER 2 LITERATURE REVIEW

2.1 Introduction to graphene

In 2004, Geim and Novoselov et al. reported the intentional empirical discovery of isolated monolayer graphene through mechanical exfoliation of graphite[2]. Such pristine graphene sheet, which is a one-atomic-thick honeycomb structure composed with sp^2 carbon atoms, was found to possess ultra-high mechanical flexibility and durability (Young's modulus: ~1 TPa; intrinsic tensile strength: 130 GPa)[21], superb optical transparency (~97% transmittance to visible and infra-red light)[22] and thermal conductivity (~ 5000 mK^{-1})[23], and a high stability in air and moisture below 300 °C. Monolayer graphene also obtains a zero-bandgap, where there is a tiny overlap between its valence and conduction bands.[2,5] In addition, graphene also has a pronounced ambipolar electric field effect, which allows the continuous tuning of charge carriers between electrons and holes in concentrations as high as 1013 cm^{-2}, which resulted in an extremely high charge carrier mobility of graphene (~100,000 $cm^2V^{-1}s^{-1}$), as well as its quantum hall effect under ambient conditions. Furthermore, all of these electronic properties of graphene were proved as quality-dependent on the graphene film, the atmospheric condition is therefore not a factor influencing graphene properties[24-26].

Because of all these fascinating and unique properties of graphene, intensive investigation about the fabrication of graphene were conducted. Moreover, due to the zero-band-gap as well as the biological and chemical-inertness of graphene, modification techniques of graphene with adequate atoms and functional groups were also widely studied.

In order to produce graphene sheets with high efficiency, chemically derived graphene from graphite oxide (GO) by chemical oxidation of graphite is regarded as an important method. After Ruoff's group first demonstration on producing single-layer graphene through solution-based process in 2006[27], oxidative treatments on graphite that based on the three principle methods by Brodie, Hummers and Staudenmeier[28], have become the most routine approach for GO production. All of these methods achieve the oxidation of graphite to various levels by adopting strong acids and oxidants, and the Hummers method has been regarded as the most common and widespread route, which the oxidation of graphite is driven by an anhydrous mixture of sulfuric acid, sodium nitrate and potassium permanganate. Different from pristine graphene film, there are abundant oxygenated, hydroxyl and epoxide functional groups on the basal planes of GO sheets; while carbonyl and carboxyl groups located at the edges. As the presence of these functional groups makes the GO sheets strongly hydrophilic, allowing them to readily swell and disperse in water. On the other hand, the oxygen groups on GO could be removed via the aqueous reduction process, giving reduced GO (rGO) sheets as the product[11,12].

In contrast, non-chemical exfoliation is regarded as the main routes to achieve graphene without the oxidation process. Liquid-phase exfoliation of graphite is based on exposing the materials to a solvent with a surface tension that favors an increase in the total area of graphite crystallites[29]. Generally, there are two methods for the liquid phase exfoliation of graphite into graphene: using high surface tension solvents or using aqueous solutions with surfactant or polymers in water as stabilizers[30]. Through the sonication of graphite in these solutions, graphite splits into individual platelets and yields a significant fraction of monolayer graphene flakes in the suspension[31,32].

Importantly, large area and uniform graphene films can be readily synthesized via scalable methods including chemical vapor deposition (CVD)[33-35], plasma-enhanced chemical vapor deposition (PECVD)[36,37] and graphitization of carbon-containing substrate. Up to date, the most typical and readily accessible approach for producing high quality graphene is the CVD approach, which generally involves the decomposition of gaseous carbon source such as methane[38], hexane, toluene[39,40] and ethanol[41] over a transition or polycrystalline metal substrate typically held at high temperature around 1000°C[42-44]. The single to few-layer CVD graphene films are commonly grown on polycrystalline metals such as Ni[45] and Cu foils[8,46], and CVD of graphene on transition metal substrates such as Pt[47], Ru[48,49], Ir[39,50] had also been explored. Large area CVD graphene sheets grown up to 30 inches which exhibited a low sheet resistance ~125 Ω/sq, high optical transmittance (~97.4%) and mobilities up to 7350 $cm^2 V^{-1} s^{-1}$ at low temperature were reported in the literatures[51]. energy-related materials[52]. Moreover, to enable the CVD-graphene fabrication at a lower temperature, the PECVD was introduced to the field in 2010[36]. As reported by Wang et al., assisted by the remote-discharged radio-frequency plasma beam source (13.5 MHz), the deposition of monolayer graphene could be done on Cu foil in less than 5 minutes at a relatively low temperature (~650 °C) when compared to the traditional thermal CVD process. In contrast, wafer-size single-to-few layer graphene films were also achieved on carbon containing substrate like silicon carbide (SiC) (0001). Such graphene films were fabricated via the sublimation of silicon atoms and graphitization of remaining carbon atoms by annealing at a higher temperature (1000-1600°C) when compared to the two methods mentioned above[53].

For the applications of these large-area, flexible, conductive and transparent graphene films, the reliable methods of isolating and transferring them onto arbitrary substrates remains a critical step. The most commonly used methods included the wet transfer process, where a polymeric protection layer was spin-coated on top of graphene, followed by etching of growth substrate underneath[9,54,55], this allows the transfer of CVD graphene film onto three different classes of substrates: substrates covered with shallow depressions, perforated substrates, and flat substrates[9]. Dry transfer is another method which is similar to the wet process, but an additional soft polydimethylsiloxane (PDMS) stamp was attached to the protective layer on top of graphene (Figure 2.1). Moreover, to ease the transfer process to be carried out in an industrial scale, the face-to-face transfer method was developed recently[56].

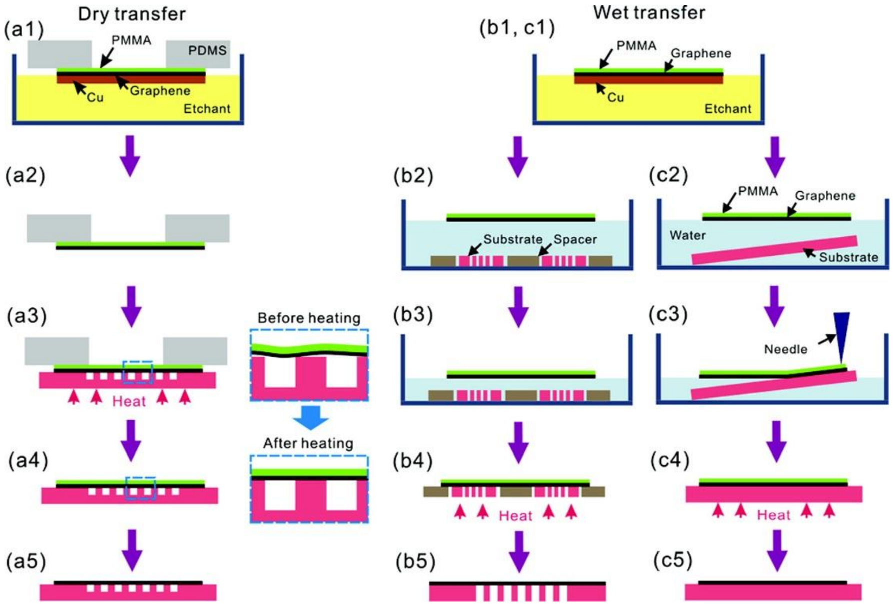

Figure 2.1 Schematic diagram of transfer processes for CVD graphene film. **a)** Dry transfer of the graphene layer onto shallow depressions. **b)** Wet transfer of graphene film onto perforated substrates and **c)** flat substrates. The boxes in dashed lines show magnified views of (a3) and (a4) [57].

Since graphene and its derivatives could be produced from the laboratory scale to large scale nowadays, together with the unique and festinating properties of graphene films, scientists have been doing several modifications on graphene for widening their application in various aspects in the recent 14 years. While the single-to-few-layer graphene possess most of the ideal theoretical properties and could be produced in large area at the same time, it has been adopted as building blocks for plenty nano-, micro- and macro-scale 2D materials through selective surface modifications. These modification strategies have significantly expanded the potential of graphene and its derivatives to a wide range of applications including energy storage[58-63], field effect transistors[15,17,64] photovoltaic devices[65-70], catalysis[71,72], sensors and actuators[16,46,73-75].

In the following parts of this chapter, various interests, strategies and respective impacts of surface modifications on graphene, as well as the application of various 2D graphene-based functional materials would be discussed.

2.2 Theoretical understanding of atomic-scale modification on graphene

The earliest interest in graphene modification was based on opening and tuning bandgap of graphene. Starting from ten years ago, a series of computations based on atomic-scale surface grafting on graphene, such as surface hydrogenation and halogenation were conducted. Zhou et al. reported the first simulation on grafting hydrogen atoms on graphene basal plane in 2009 via the DFT calculation[76]. With both sides of the graphene grafted with hydrogen atoms, ‘graphane’ film will be achieved. On the other hand, ‘graphone’ film would be resulted if all hydrogen atoms on same side of ‘graphane’ were removed. And surprisingly, graphone was proved as a ferromagnetic semiconductor that obtains a small indirect gap (0.46 eV), while both graphane and graphene are nonmagnetic. The major reason for such ferromagnetism of graphone is the half-hydrogenation broke the delocalized π-bonding network of graphene, that the electrons in the unhydrogenated carbon atoms were localized and unpaired. Based on the calculation, the magnetic moments at these sites couple ferromagnetically under an estimated Curie temperature between 278 - 417 K, hence making graphone an infinite magnetic sheet with structural integrity and magnetic homogeneity.

Later, Xiang et al. further studied the graphone by combining the results achieved via cluster expansion method with the DFT calculation[77]. They found that the hydrogen atoms grafted on graphene films tend to form a one-dimensional (1D) chains. This lead to a competition between elastic strain energy and electronic kinetic energy along the graphene film, and ripples would be formed between the sp^2 carbon atoms. Interestingly, such large strain was further proved to avoid the phase separation between the sp^3 carbon and sp^2 carbon basal plane. Therefore, single-sided covalent functionalization might be a preferable way to tune the electronic properties of graphene while preserving its lattice structure.

Instead of a homogenous plane grafted with hydrogen atoms, Haberer et al. demonstrated the first single-side, partial hydrogenation on graphene. Via hydrogen plasma treatment on CVD graphene transferred on gold substrates, a 'C_4H' configuration was achieved [78]. The resulted product obtained a wide band gap (3.5 eV), thus expected as a functional layer for optoelectronics working in the UV light range. As an extension of this work, Li et al. further stimulated a series of 1D C_4H structure via DFT calculations, for example, the C_4H nanotubes and C_4H nanoribbons[79]. According to their results, we know that a symmetric, double-side hydrogenated graphene layer was impossible to be achieved, as the alternative double-side graphene-embedded structure is more energetically preferred.

Other than grafting hydrogen atoms on graphene films, the grafting of halogen atoms have also been widely investigated[80,81]. Singh et al. predicted a range of hydrofluorinated graphene (HFG) structures in 2011[82]. According to their calculation, the most stable HFG structure is the chair conformer one, where the graphene film was one-side grafted with H atoms while the other side bonded with F atoms. Together with the other structure that each side of graphene is heterogeneously bonded with H and F atoms, the HFG was expected to obtain the bandgaps with size ranging from 3.34 - 5.25 eV. Based on this work, Li et al. also pointed out that there should be a strong interfacial interaction among the HFG layers due to the abundant hydrogen bondings in between them (C-H···F-C). Beyond their expectation, these interactions would lead to the stacking of the semiconducting HGF layers and resulted in a metallic bilayer[83].

Afterwards, in 2012, Yang et al. reported a stable charge-transfer complex yielded from the adsorption of photogenerated chlorine atoms on single side of graphene via DFT calculation. This one-side halogenation lead to a p-type doping of graphene while the sp^2 hybridized carbon skeleton was remained.[81] Such charge-transfer complex might not stable in the early stage, and they would undergo further alternative transformations: either covalently bonding of adsorbed chlorine atoms to the para-site carbons, or combination of two adjacent chlorine atoms would occur. By taking all the possible situation in account, the band structures of various chlorinated graphene structures were calculated, and the bandgap of these chlorinated graphene complex was ranging from

0 to 1.3 eV. To extend their work, instead of graphene modification with a single species, asymmetric modification of graphene with two kinds of atoms were also reported by the group in 2013 as shown in Figure 2.2 a[84].

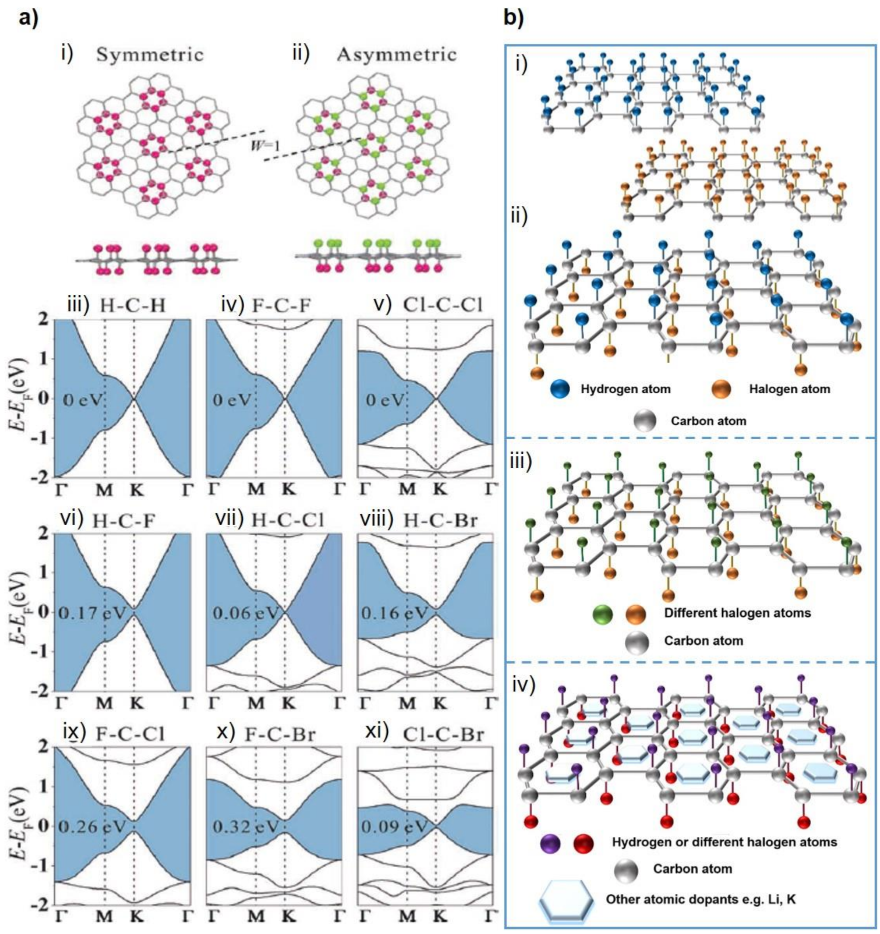

Figure 2.2 a) Schematic diagrams of (i) symmetric and (ii) asymmetric modified-graphene films. (iii-xi) Band structures for various symmetric and asymmetric modified-graphene films, showing with their band gaps values.[84] **b)** Theoretically favorable asymmetrically-modified graphene: (i) single-side hydrogenated graphene (graphone) and single-side halogenated graphene, (ii) hydro-halogenated graphene, (iii) graphene film modified with different halogen atoms on opposite sides, and (iv) hydro-halogenated graphene combined with dopants.

A series of Janus structures, which refers to asymmetrically modified films, were fabricated through grafting various combinations of halogen (F, Cl or Br) and hydrogen atoms on the two sides of graphene sheets. According to their results, when the two different elements on the opposing sides are further apart from each other in the periodic table, the modified graphene would achieve a larger bandgap[84].

On the other hand, in addition to the H and halogen atoms, Ong et al. further stimulated the configurations of graphene doped with Li or K atoms (Figure 2.2 b), and discovered the piezoelectric properties possessed by these modified-graphene[85]. Also, in another report released later from this group further suggested that, if the monolayer graphene grafted with two various kinds of dopants on its opposite side, they would possess strong piezoelectricities which were comparable to those of existing bulk piezoelectric materials (e.g. wurtzite BN and GaN) [86]. If such nanoscale piezoelectric materials with outstanding flexibility could be realized, they would play a key role in the development of energy conversion device and flexible electronics[87].

2.3 Hydrogenation and halogenation on graphene

After a number of calculations and theoretical predictions of modified graphene were conducted, different experimental researched have been done on graphene and its derivatives. For realizing the halogenated graphene, graphene samples were preferable to be placed under mild atmosphere filled with halogen atoms instead of common plasma practice, as the one-atom thick graphene layer could be damaged by ion bombardment. In 2010, via exposing a gold substrate supported graphene under a XeF_2 atmosphere, a fluorinated graphene structure was achieved by Nair et.al. [88]. Through the decomposition of XeF_2, the graphene was exposed to atomic F and bonded with the F atoms.

Not until 2011, the synthesis of single-side chlorinated graphene was reported by Wu et al. [89]. In this work, three kinds of graphene films were adopted: the mechanically exfoliated graphene, CVD graphene, and graphene nanoribbons. All the graphene samples were first transferred on a SiO_2/Si substrate followed by exposing to Cl_2 plasma. Importantly, if the exposure time of graphene under the plasma is short enough, which is less than one minute, the graphene layers were successfully p-doped without any structure destruction. Moreover, it was proved that the conductance of such Cl-functionalized graphene was higher than the original graphene sheets. For more detailed studies on the halogenation based on this short-time plasma approach, the group also demonstrated the production of H- and F- functionalized graphene under the F_2 or H_2 plasma treatments respectively.

Zhang et al. then reported the asymmetrically modified graphene films via photohalogenation[90]. In their experiment, mechanically exfoliated graphene and CVD graphene films were transferred on Si/SiO_2 wafer and were exposed to an atmosphere filled with Cl_2/N_2 gas mixture. In aids with a xenon lamp (0.9 W/cm^2), the chlorine molecules split into highly reactive chlorine radicals, which consequently grafted on the basal plane of graphene through the free radical addition reaction (Figure 2.3 a-d). Furthermore, by spin-coating a poly (methyl methacrylate) (PMMA) layer on top for the chlorinated side of graphene, the whole film could be peeled off from the substrate, which allowed the bottom pure carbon side to be further modified. The Janus functionalized graphene films fabricated by this approach were found to exhibit different wettability on the different sides as shown in figure 2.3 e.

Instead of the predictions which were done on monolayer graphene as mentioned above, Yuan et al. set up a calculation on H and F grafted graphene on a bilayer graphene. Interesting, by grafting H and F atoms on opposite sides of the bilayer, a special configuration with repeating unit denoted as H–C2 and F–C2 was achieved, which is similar to a diamondol structure (a 2D hydroxylated diamond layer, formed by compressing two monolayer graphene monolayers with topmost layer covered with hydroxyl groups) [91,92]. Interestingly, according to their calculations, the number of sp^3–hybridize C atoms were different between the two graphene layers. The first graphene layer would be fully sp^3–hybridize while only half of the carbon atoms in the second layer is sp^3–hybridized. And due to the presence of those non-hybridized states, the modified bilayer graphene achieved the extraordinary ferromagnetic properties.

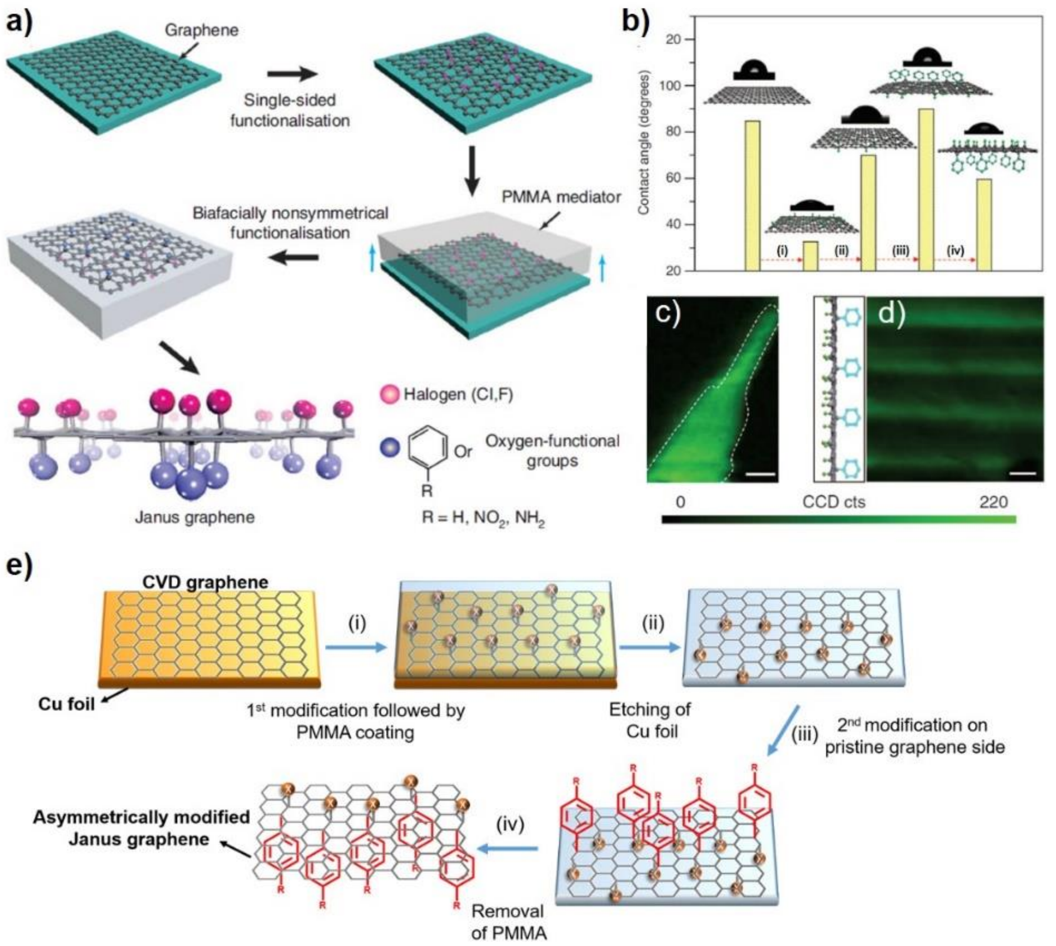

Figure 2.3 Synthesis of asymmetrically modified (Janus) graphene films. **a)** Schematic diagram of the bifacially nonsymmetrical functionalization on CVD graphene via PMMA-assisted transfer process. **b)** Wettability of the nonsymmetrical modified graphene surface through different fabrication procedures: (i) single-sided photochlorination on graphene film; (ii) exposure of unmodified side; (iii) single-sided phenylation; (iv) asymmetrically modified graphene. The insets images include to the schematic diagrams of the asymmetric film surfaces with corresponding wettability test images. **c)** Intensity map showing D band for Janus graphene. The white dotted indicated the boundary of the graphene flake. **d)** D-band mapping for a Janus graphene film with functional groups patterned with designed pattern, as illustrated on the left. (Scale bars = 5µm).[90] **e)** Schematic diagram showing the general fabrication routes and of asymmetrically modified graphene film.

2.4 Surface modification on graphene with small molecules

2.4.1 Covalent modification with small molecules

So far, most of the covalent modifications have been done on graphene with small molecules, were achieved with diazonium salts. The reaction is initialized by the spontaneous transfer of electrons from the graphene layer and its substrate to the diazonium salts. To these days, the diazonium salts have already been widely applied on grafting acryl groups onto the surface of sp^2-hybridized carbon materials, such as glassy carbon[93], HOPG[94], and CNT [95,96].

In 2008, Bekyarova et al. prepared a 4-nitrophenyl diazonium (NPD) tetrafluoroborate modified graphene layer which was epitaxially grown on SiC substrate (Figure 2.4 a)[10]. The aryl groups of the NPD tetrafluoroborate attached the conjugated carbon atoms and changed the graphene samples from near-metallic to semiconducting. Obviously, the changes on electronic properties of graphene is due to the covalent bonding between carbon atoms of graphene film with the foreign species, which finally lead to the conversion of carbon centers from sp2 to sp3, as well as a saturation of conjugated electronic structure. Therefore, the changes in graphene conductivity should be indirectly proportional to the degree of such modification. As pointed out by Sinitskii et al., the conductivity of a monolayer graphene nanoribbon (GNR) decreased with the prolonged diazonium treatment with 4-nitrobenzene diazonium tetrafluoroborate, which covalently bonded to the carbon atoms on GNR through the 4-nitrophenyl groups[97]. Nonetheless, the changes on electronic properties of graphene caused by the diazonium salt modification also depends on the functional group in the para position to the phenyl group, as well as the doping effect they would bring to the graphene layer. As reported by Farmer et al. that, no conductance changes had been recorded for their graphene device at the neutrality point after the graphene film was modified with a 4-bromobenzene diazonium salt[98].

In 2014, Bissett et al. further modified the opposite sides of the monolayer and bilayer CVD graphene films with diazonium salts which possessed different aryl groups

(Figure 2.4 b) [99]. As the first step of their experiments, graphene films transferred on SiO_2 substrates were immerses into an electron donating (n-type) dopant 4-methoxybenzenediazonium tetrafluoroborate (MBD) solution, that the MBDs were grafted on top of graphene surface covalently. Subsequently, the reacted side was protected by PDMS, and the unreacted side was exposed and bonded with the 4-nitrobenzenediazonium tetrafluoroborate (NBD), which is an electron withdrawing (p-type) species.

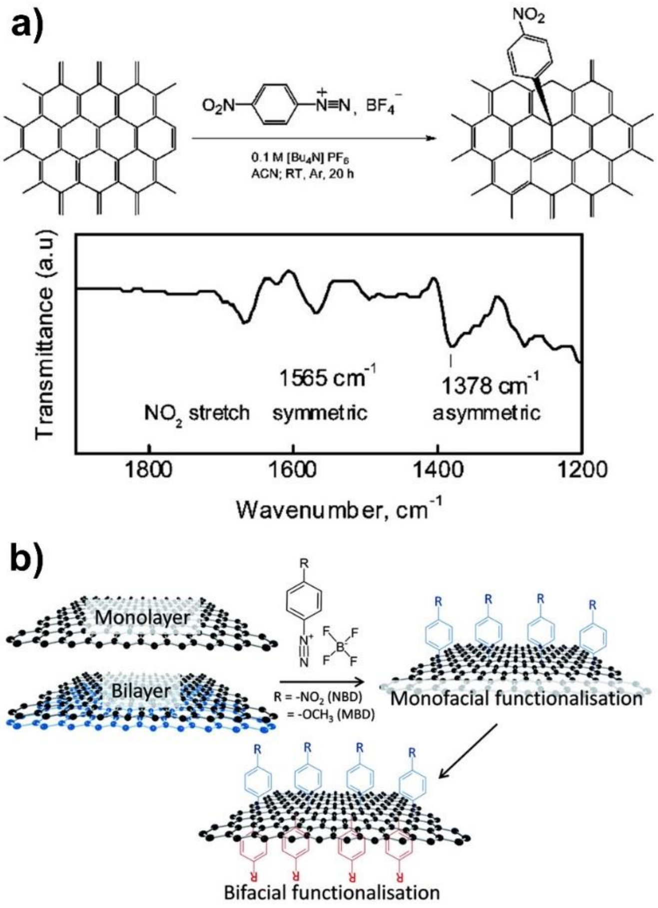

Figure 2.4 Schematic illustration showing covalent surface modifications of graphene with diazonium salts. **a)** (Top) Spontaneous grafting of aryl groups to graphene basal plane via reduction of 4-nitrophenyl diazonium (NPD) tetrafluoroborate. (Bottom) FTIR spectrum of NP-functionalized graphene.[10] **b**) Single-side and two-side aryl diazonium functionalization on monolayer and bilayer graphene film.[99]

Interestingly, after the non-symmetrical modification on graphene opposite sides with n-type and p-type dopants respectively, the net doping of the modified graphene was found to be p-type. In another word, there were more NBDs covalently bonded to the graphene surface. As the grafting of NBDs was the second modification step on such Janus graphene film, the increase in graphene reactivity determined that the reactivity of the bare graphene surface could be altered by the modified side at its back. Moreover, the as-fabricated Janus graphene films showed a significantly higher doping level when compared with the single-side and symmetrically functionalized graphene; the asymmetric functionalization hence allowing an electronic structure control of both monolayer and bilayer graphene in a larger range.

2.4.2 Non-covalent modification with small molecules

Different from covalent functionalization, non-covalent modification of graphene is an approach of functionalization the graphene surface while leaving its natural sp^2 carbon conjugated structure unaffected. In general, non-covalent modifications on graphene mainly depend on the Van der Waals force[100-102], electrostatic interaction[12,103,104], hydrogen bonding[105,106], coordination bonds[107,108] and π–π stacking interactions[13,109-112]. As there are extended π-conjunction on the graphene surface, graphene modification with small molecules possess relatively large non-polar aromatic rings through π–π interaction is versatile and promising, and such modification could be easily achieved over a large-area graphene surface in a uniform way. Up to these days, π-orbital-rich groups which have been adopted on graphene sheets modification via π-π stacking interaction include the followings: pyrene [109,112,113] and π-orbital rich aromatic molecules such as benzopyrene[114], 1-pyrenebutyrate[115], and dopamine[116].

As a typical example, a band structure tuning method for graphene layer was achieved in a non-covalent way as reported by Coletti et al. in 2010[117]. By functionalizing the graphene layer epitaxially grown on SiC (0001) with tetrafluorotetracyanoquinodimethane (F4-TCNQ) molecules, the bandgap of graphene could be tailored. As the cyano groups of the F4-TCNQ molecules tend to remove electrons from the graphene layer, a charge-transfer complex was formed between graphene and the F4-TCNQ molecular overlayer, as well as leading to the charge neutrality for monolayer graphene.

2.5 Surface grafting with functional polymers

To date, as the polymers could be synthesized with various chemical structures and high-density functional groups, there have been plenty modifications on graphene achieved with polymers. Such modifying process could be categorized into two main approaches: The 'grafting-from' and 'grafting-to' method. The 'grafting-from' method refers to the polymerizations which take graphene as the initiation site; while the 'grafting-to' approach refers to the modification achieved via coupling between graphene and polymers through chemical reaction.[11]

2.5.1 Covalent grafting of polymers

As there are abundant oxygen-containing groups present on graphene oxide sheets, researchers have demonstrated enormous covalent grafting of polymers on the GO-based 2D materials via in-situ polymerization reactions.

In particular, self-initiated photo-grafting and photo-polymerization (SIPGP) is the most commonly adopted polymerization method, in which styrene, maleic anhydride, and several acrylate-type monomers[118,119]. As these activated monomers could be excited by free radicals under UV radiation, they are able to abstrac hydrogen radicals from hydroxyl and epoxy groups on GO sheets, thus creating radical sites and initiate polymerization reactions [120]. For example, Steenackers et al. demonstrated the grafting of styrene-bearing polymers on CVD graphene film and epitaxial graphene grown on SiC via SIPGP. The resultant Raman spectroscopy data revealed that such photopolymerization only occurred on pre-existing defect sites on the graphene layers. Therefore, this modification would not disrupt the original basal plane structure of graphene[14].

On the other hand, asymmetrically modified GO nanosheet were prepared via a covalent “grafting to” method as reported by Wu et al. in 2015[121]. Monolayer GO sheets were first coated onto the wax microspheres through the wax-in-water Pickering emulsion process, followed by surface grafting of an amino-containing polymer – poly (propylene glycol) bis(2-aminoproryl ether) carried out on the surface of GO sheets. After the polymerization was completed, single-side modified GO sheets could be released and collected by simply dissolving the wax core with chloroform.

2.5.2 Non-covalent grafting of polymers

To modify graphene with polymer via non-covalent way, π-π stacking is the major strategy, which always includes the synthesis of polymer chains with pyrene group on one end.

For tuning the surface wettability of CVD graphene film without degrading its electronic properties, Wang et al. demonstrated a non-covalent conductive polymer coating on graphene in 2009. Wang et al. and his co-worker modified CVD graphene with self-assembled layer of pyrene buanoic acid succidymidyl ester (PBASE) as shown in figure 2.5 a, which could stack on the graphene surface in uniform manner via the pyrene group[69].

Reversible addition fragmentation chain transfer (RAFT) polymerization is another useful tool for grafting polymers on graphene with well-controlled architectures.[122-127] In recent studies, Liu et al. synthesized a well-defined thermoresponsive pyrene terminated poly(N-isopropylacrylamide) (PNIPAAm) through RAFT polymerization, and attached them onto the basal plane of graphene sheets via π-π stacking interactions (Figure 2.5 e)[128]. Similarly, Bai et al. functionalized CVD graphene films with conjugated polymer sulfonated polyaniline (SPANI), which is soluble in water with good air stability and electrochemical activity[111].

Xiao et al. also demonstrated a non-covalent grafting of polymer brushes onto CVD graphene films in 2013[129]. A patterned NH_2-terminated pyrene derivative layer (Py-CH_2NH_2) was successfully transferred on the graphene scaffold via micro-contact printing, and the organic layer successfully anchored on the graphene layer via π-π stacking interaction. As there are amino groups on the outer face, further photo-polymerization could be carried out.

Apart from pyrene groups, due to the non-specific stickiness of dopamine to a wide variety of surfaces, polydopamine is also widely used for non-covalent surface treatment on low surface energy materials. Since the polydopamine layer is highly hydrophilic, polymers that do not normally wet pristine graphene could be readily deposited after the polydopamine deposition. For example, Kim et al. depositied a thin layer of neutral poly(styrene-ran-methylmethacrylate) (P(S-*r*-MMA)) on a polydopamine-modified CVD graphene layer through simple spin coating process. Further covalent reaction between the hydroxyl groups of the copolymer and the catechol groups of the polydopamine was achieved via a thermal annealing step.[130]

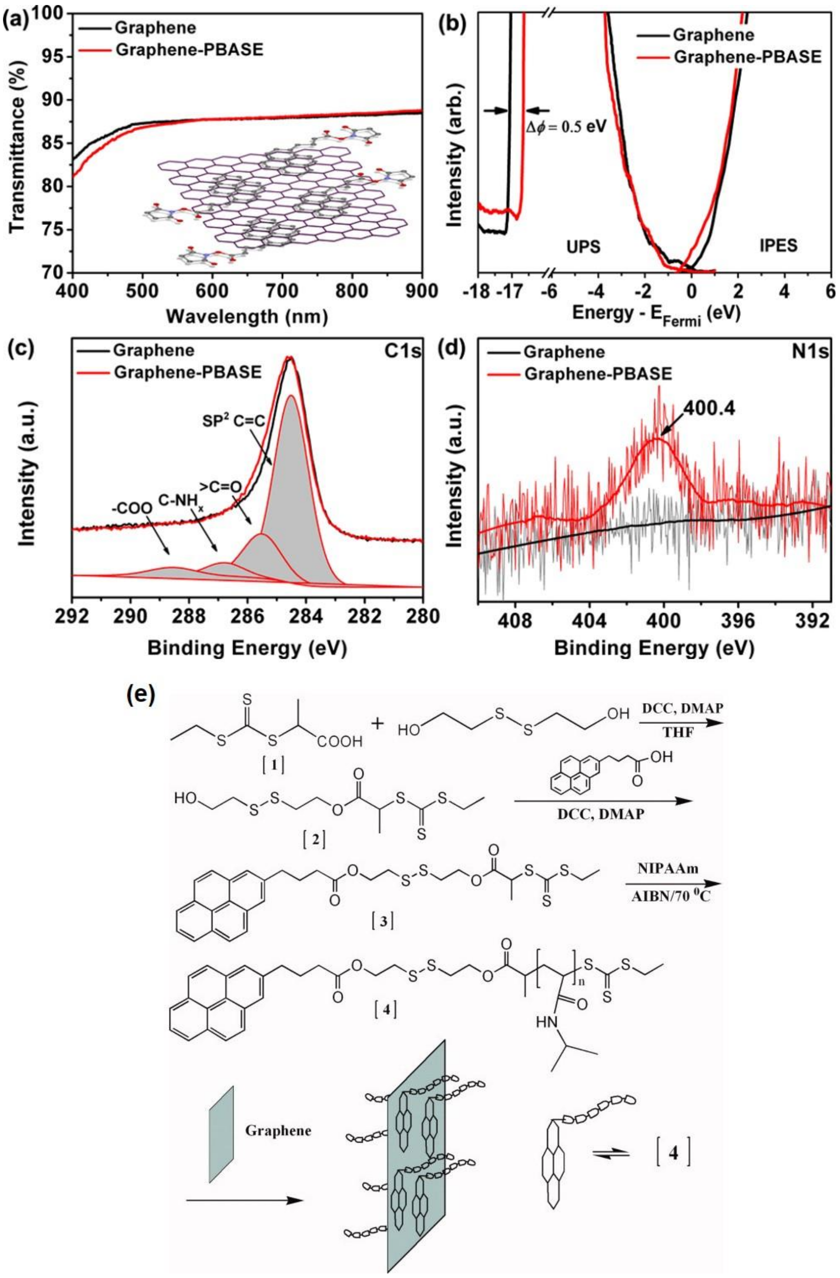

Figure 2.5 Modifications of graphene film via polymer grafting. **a)** Transmittance spectra of the graphene modified by PBASE. Inset: schematic diagram. **b)** Combined UPS and IPES spectra, **c)** and **d)** XPS C 1s and N 1s core-level spectra of PBASE modified graphene, respectively.[69] **e)** Thermosensitive graphene nanocomposites formed using pyrene-terminal polymers made by RAFT polymerization.[128]

2.6 Deposition with metals and metal oxides

2.6.1 Vacuum deposition of ultrathin films

Besides the graphene surface functionalization achieved with organic moieties, metal and metal oxides could offer graphene films other specific electrical and chemical properties that could not be achieved with organic substances. For the graphene decoration with an ultrathin layer (<10 nm) of metal or metal oxides, physical vacuum deposition is always the most straightforward approach, especially for depositing metals (e.g. Au, Ag and Cu), which are important conductive materials in wide range of electronics[131]. These resulted film structures were largely dependent on the deposition conditions and the topography of graphene layer. For example, it was found that the grain size of thermal deposited Au layer (<5 nm) increased with the increasing number of graphene layers, but the grain density decreased at the same time[132]. While by Au sputtering process, Au particle size (< 2 nm in diameter) could be precisely controlled by adjusting the rate of deposition, operation angle, applied current[133]. On the other hand, atomic layer deposition (ALD) is a valuable tool for the deposition of uniform and ultrathin (Å) metal or metal oxide layers on graphene surface with precise control in thickness[134,135]. However, additional chemical treatment on graphene films is needed before ALD to take place, as pristine graphene layer is inert to the nucleation of inorganic particles in the ALD process. For example, gaseous phase pretreatment with 3,4,9,10-perylene tetracarboxylic acid (PTCA) [135], NO_2 [136], or ozone [136] is required before the nucleation of the Al_2O_3 on graphene's basal plane.

2.6.2 Solution deposition of metal nanoparticles

Instead of physical vapor deposition, nanoparticle-decorated graphene sheets are widely synthesized via the solution-based chemical approaches. As there are abundant oxygen-containing groups present on chemically exfoliated and modified graphene sheets, metal oxide nanoparticles (NPs) could easily anchor on graphene by simple immersion step as demonstrated by Yu et al.[137]. With protection under a spin-coated PMMA layer, the ZnO-attached graphene sheets could be lifted off, exposing the bare graphene surface for further modification. An asymmetrically modified graphene sheet with the spherical ZnO and cubic Au NPs deposited on the opposite surfaces was then resulted in this experiment (Figure 2.6), which are potentially applicable in optoelectronic nano-devices.

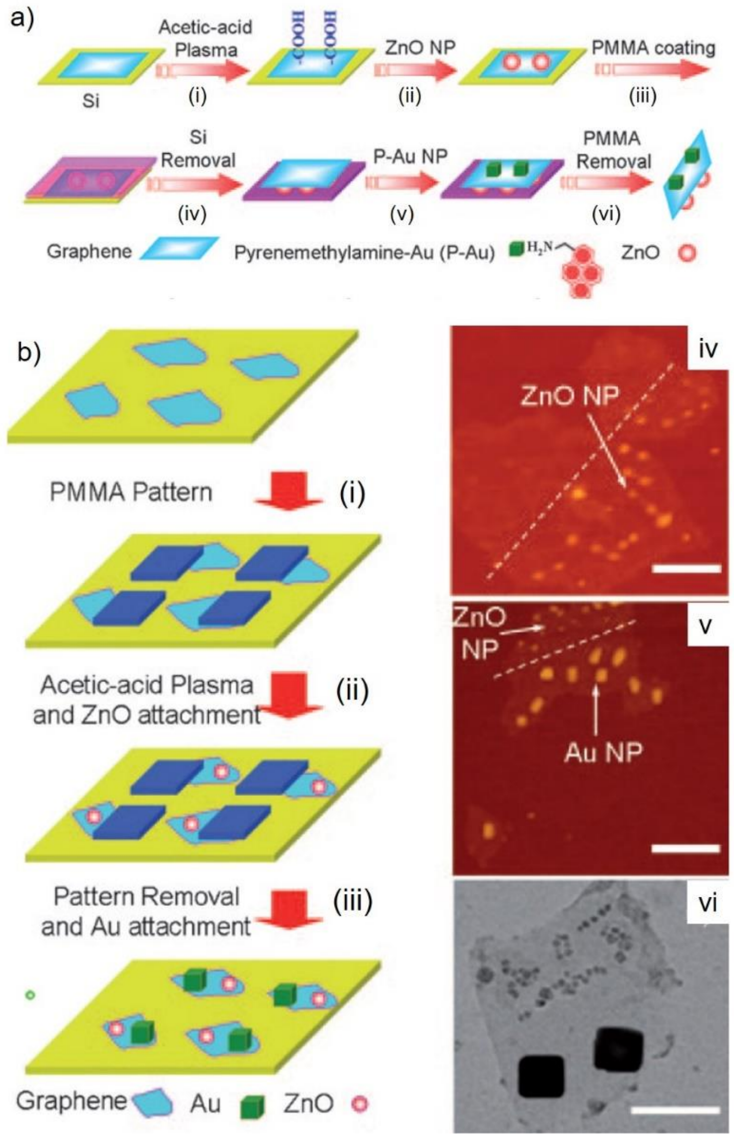

Figure 2.6 Asymmetrically modified-graphene decorated with metal and metal oxide nano-particles. **a)** Schematic diagram showing the fabrication procedure of the asymmetrical functionalized graphene film with ZnO and Au NPs. **b)** (i-iii) Deposition procedure of spherical ZnO NPs and cubic Au NPs on patterned graphene sheets. iv) AFM image showing the selective attachment of ZnO NPs on plasma-treated area of graphene sheet. v) AFM and vi) TEM images showing the ZnO NPs deposited in the plasma treated area, and the large cubic Au NPs with small spherical ones attached in the ZnO/plasma-free region of the modified graphene sheet. Scale bars: iv) 1 mm; v) 2 mm; vi) 100 nm.[137]

Later in 2015, a noble metal (Au, Pt, Pd) NPs decorated CVD graphene with was fabricated by Toth et al. through the in-situ galvanic displacement[138]. In their work, CVD graphene supported with Cu foil was immersed into the precursor solution of the noble metals. Galvanic displacement of metal NPs (Au, Pt, Pd) occurred on the upper surface of CVD graphene, where the Cu foil acts as an electron donor that transfers electrons to the precursor salts ($AuCl_4^-$, $PdCl_4^{2-}$, and $PtCl_4^{2-}$)[139].

2.7 Preparation of functional graphene-based thin films

Other than functionalized mono-to-few layer graphene, numerous modified graphene-based thin films composed of solution exfoliated graphene nanosheets, GO, reduced GO (rGO) were also fabricated[140,141]. In principle, the modification procedure discussed above are all applicable to the surface modification in this section. However, covalent modification is the dominated modifying approach, as most of the graphene-based thin films are made up of GO and rGO sheets, which are rich in oxygen-containing groups.

In 2014, Xiao et al. reported the large-area growth of delicately patterned polymer brushes layer over GO sheets deposited on Si substrate[142]. Since there are strong supramolecular hydrogen bonding presented between GO nanosheets and the HO-terminated surface, GO sheets could be micro-contact-printed by using a PDMS stamp. As there are plenty photoactive site on the GO surface, polymer brushes layer following the well-designed patterns could be achieved via SIPGP. In their experiments, a nearly defect-free polystyrene (PS) brushes layer was successfully grafted onto micro-patterned GO films with a well-controlled height (~60 nm) in a large feature space (10 μm). Furthermore, by immersing the PS decorated samples in an aqueous KOH solution, the polymer brush@GO films were released from the Si surface and transferred on other substrates.

Other than pure GO films deposited on a substrate, a freestanding hybrid sheets composed with GO and chitosan were prepared by Han et al. in 2014[143]. Since the GO nanosheets carry negative charges, that can form stable complex with positively charged polyelectrolytes, they would assemble with the positively charged chitosan in aqueous solution and spread as a composite membrane. To further functionalized the hybride film, the hybrid sheets were functionalized by grafting two polymer brushes: polystyrene (PS) and poly(2-(dimethylamino) ethyl methacrylate) (PDMAEMA) brushes on the two faces respectively. Since the surface wettability of these two kinds of polymer brushes layer are largely different from each other, a membrane with contrasting hydrophilicity on the top and bottom sides was created.

In addition, Xiao et al. have demonstrated the fabrication of two-side functionalized patterned carbon-based hybrid film via a micro-contact printing and life-off process[144]. CNT/GO films were first deposited on SiO_2/Si wafer as starting material, and the PDMAEMA brushes were grafted on top via SIPGP. By etching the SiO_2 layer on the wafer, the CNT/GO films were released as a free-standing film and the unreacted side could be exposed. In this way, the polymer-grafted side is an insulating carpet while the leaving the carbon side conductive; thus, forming a flexible and miniature electric carpet with potential applications for the localized heating of micro-/nano-devices.

Other than the organic functionalization, modifications with inorganic particles and layers were also demonstrated on the graphene-based 2D materials. As graphene is conductive in nature, electrochemical deposition of is a feasible and effective approach for depositing metal and metal oxide on graphene surface. In 2010, Wu et al. and co-workers reported a series of metal oxide deposition on rGO thin films which supported by PET film, including the ZnO nanorods, p-type and n-type Cu_2O films [145,146]. As the modified rGO films could be released from the substrate, this one-side modified rGO film could act as conductive transparent electrode (rGO side) as well as active absorbers (semiconducting metal oxides layers side) when transferred on a photovoltaic device.
Moreover, as demostarted by McGrail et al., pH-responsive GO platelets was fabricated via functionalized on side of the GO sheet with polystyrene (PS), and the other side with poly(acrylic acid) (PAA).[147]. Acrylate functionalities were first appended to both

faces of GO through an acidic aqueous treatment with acrylonitrile, which gave Acr-GO-Acr as the product. Since these product platelets would align at the interface between oil and water phases, they were introduced into an interface between water layer with water-soluble PAA5-SH and a toluene layer with oil-soluble PS40-SH. PS40-GO-PAA5 Janus GO sheets was then yielded from the double thiolene reaction, which could stabilize the emulsions at high pH. However, under acidic conditions (pH~2), PS40-GO-PAA5 could no more stabilize the emulsions as the protonation of carboxylic acid moieties occurred and decreased the solubility of the PAA in water.

2.8 Applications of functional graphene-based Materials

2.8.1 Surface functionalization

In general, by taking advantages of the ultrathin thickness of these 2D graphene-based functional objects, one of the major applications is to transfer them onto target substrate for modifying the surface wettability and reactivity. They are always lifted off from the original substrate through wet-etching process, and then fished onto a target substrate. As a routine practice, a PMMA sacrificial layer is needed to protect the very thin 2D objects (e.g. <10 nm) in the transfer process. For example, Zhang et al. synthesized a Janus graphene layer with the PMMA-assist transfer, that after one side of the CVD graphene film was modified by chlorination, the chlorinated-side was protected of PMMA layer and turn up-side-down, allowing the other side to be modified with phenyl group[90]. This resulted Janus graphene exhibited different surface wettability on its two faces: the contract angle was 89.9° on the phenylated side and 59.6° on the chlorinated side. As shown in figure 2.7, Wang et al. reported a fluorinated graphene (FG) transferred on SiO_2/Si and quartz substrates[148], which was obtained after removing the PMMA protection on the transferred CVD graphene followed by an exposure to XeF_2 in an inert atmosphere. Such FG layer was favorable for mesenchymal stem cells (MSCs) adhesion, growth and proliferation. In aids with the patterned PDMS layer printed on top, the cell neurogenesis was further enhanced with channel-confined cell elongation.

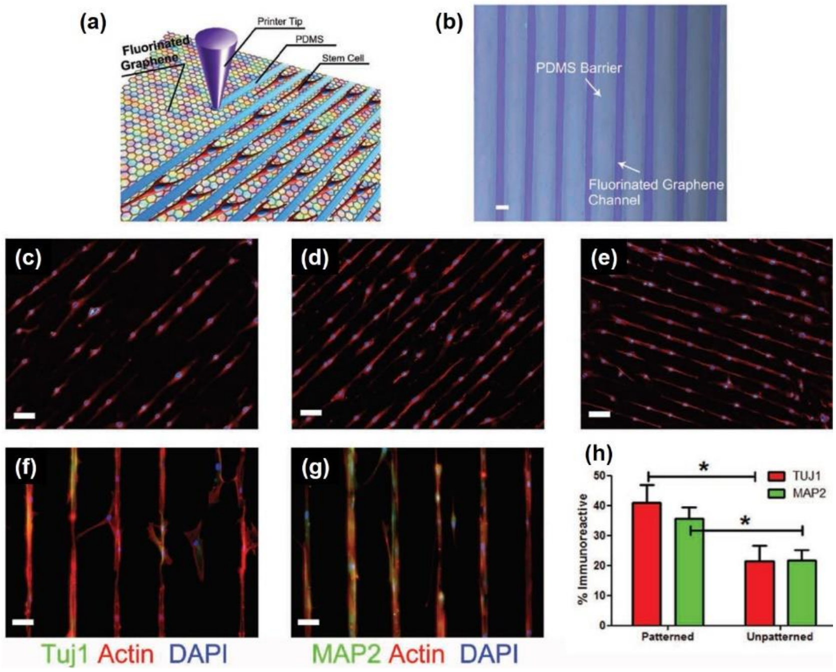

Figure 2.7 Patterning on fluorinated graphene (FG) film via large-area ink-jet printing method. **a)** Schematic diagram of depositing PDMS barriers on graphene films through direct inkjet printing. **b)** Microscopic image of patterned PDMS barrier on a FG film (scale bar = 50 μm). The aligned growth of stem cells on **c)** unmodified graphene, **d)** partially fluorinated graphene and **e)** fluorinated graphene with PDMS barriers prtined on top (scale bar = 100 μm). **f & g)** Microscopic image of MSCs attached on the FG strips, with their F-actin aligned (red) and expressing neural specific markers—Tuj1 and MAP2 (green) (scale bar = 50 μm). **h)** The percentage of immune-reactive cells for Tuj1 and MAP2 on unpatterned and patterned FG strips. The patterned FG strips induced a higher expression of Tuj1 and MAP2 in the absence of retinoic acid. ($n = 6$, $p < 0.05$)

More recently in 2015, Singh et al. developed a surface plasmon resonance (SPR) immunosensor with high efficiency with a single-side modified graphene film transferred on Au substrate[149]. In order to amplify the SPR signal and to control the immobilization of biotinylated cholera toxin antigen, they modified the CVD graphene surface with copper coordinated nitrilotriacetic acid (NTA) synthesized with a terminal pyrene groups. And the results showed the graphene-functionalized SPR sensor performances increased by 80% compared to the graphene-devoid setup.

2.8.2 Field-effect transistors (FETs)

As mentioned in previous sections, it is very difficult to apply pure graphene in the FETs due to its a zero-bandgap, which makes it a semimetal and could lead to a high leakage currents and ready power dissipation of the device[150]. Although they are several available covalent modification methods that could tune the graphene's bandgap efficiently, the basal plane of graphene was destroyed at the same time, and lost their original high electronic conductivity and mobility. To avoid such damage, Sarkar et al. develop a bandgap tuning modification graphene via mono-hexahapto (η^6)-chromium complexation. The η^6-mode of bonding is distinct from those conventional covalent σ-bond formation, there are no of sp^3 carbon centers would be created in the graphene lattice. The functionalized carbon atoms therefore remaining a part of the electronic band structure, and the high mobility of graphene could be preserved. Furthermore, this modification on graphene was proved to be effective as the FETs made with this functionalized graphene films showed an enhanced on/off ratio to 5~13[151].

On the other hand, a non-covalently functionalized graphene film was used as a biomolecules reactive layer in a highly sensitive FET biosensor. As demonstrated by Yang et al., the pyrene-modified HER2-specific aptamer was immobilized on a graphene nanomesh (GNMs) via the π-π interaction[152]. As the interactions between the aptamer and HER2 protein can vary the charge-carrier density on the surface of the GNMs, a label-free detection of the protein could be achieved by using a FET configuration. As a proof-of-concept, a real-time detection of breast cancer cells by this graphene-based sensor was also demonstrated (Figure 2.8).

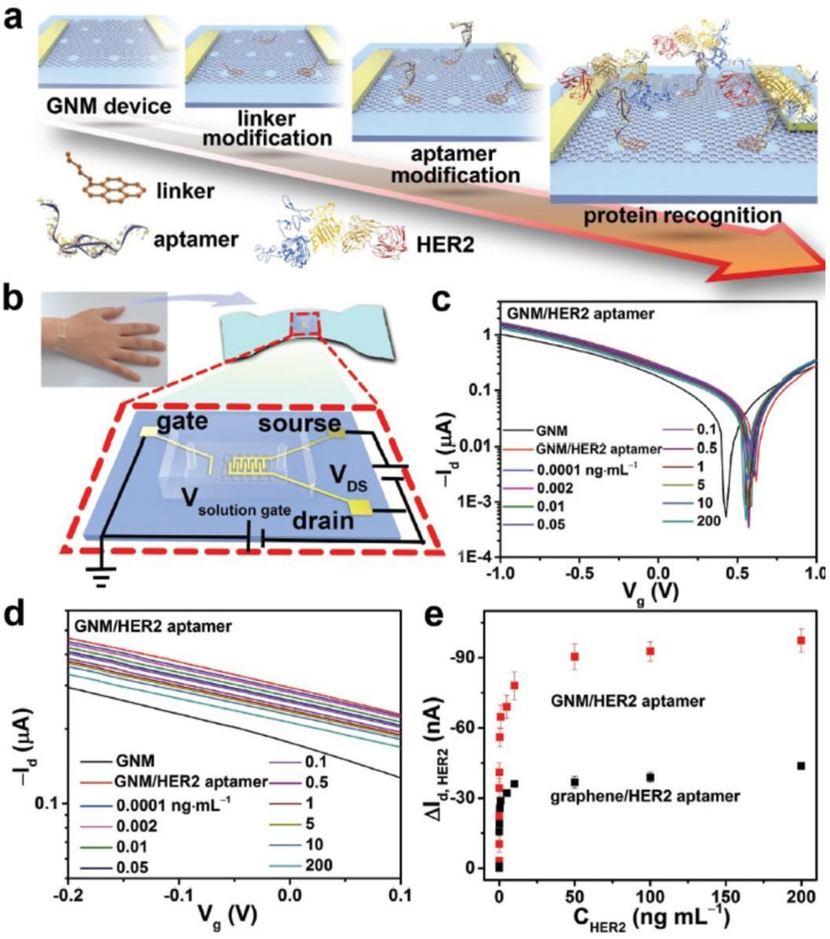

Figure 2.8 GNM FET biosensor. **a)** Schematic diagram of the fabricating procedure of the GNM FET biosensor. **b)** Digital image of a GNM FET biosensor built on a thin and flexible PDMS substrate attached on human skin. Enlarged view is the corresponding structure of the biosensor. **c)** Transfer characteristics of a solution gated GNM FET biosensor in response to HER2 protein concentrations ranging from 0.0001 to 200 ng ml^{-1}. The V_d is set at a fixed value of −0.1 V. **d)** Magnified curve of (c) in the Vg range of −0.2 to 0.1 V. **e)** Current change (ΔI_d, HER2) versus HER2 concentration (CHER2). The error bars present the standard deviations of three measurements[152].

2.8.3 Actuators

Through asymmetric surface modification on graphene-based sheets, the two sides of such 2D materials would behave in an unbalance way when they were exposed under specific external stimuli at the same time. Therefore, changes in shape and movement of the 2D sheets could be realized by designing the stress/strain response on each side.

For example, by fabricating a graphene films with two faces possessing contradictive hydrophilicity, an actuator responsive to moisture could be achieved. In this case, the Janus graphene-based electrochemical actuator developed by Xie et al. would be a typical example[153]. Via direct hexane and O_2 plasma treatments, a rGO film (thickness ~ 4-5μm) with its two sides obtaining significant difference in hydrophilicity was created as shown in figure 2.9. The rGO face treated with hexane plasma became hydrophobic that can limit the accessibility of electrolyte ions; while the O_2 plasma treated side became relatively hydrophilic. Therefore, bending motions of the asymmetrical rGO sheet could be triggered by the contrasting responses of each side under the electrochemical charge/discharge process, and the degree of bending could be controlled by adjusting the applied voltage. In consequent, the modified graphene strip bent towards the hexane plasma treated side at negative bias and vice versa.

More recently, Mu et al. and co-workers fabricated a walking device with a asymmetrically modified GO-based paper[154]. In that work, polydopamine (PDA) grafted GO nanosheets were deposited onto rGO paper via filtration. In aids with a filtration mask, a patterned GO-PDA/rGO bilayer could be achieved. When the modified free-standing graphene-based film was immersed in hydroiodic acid, the GO areas covered by GO-PDA protected from reduction, thus keeping its hydrophilic nature, while the uncovered GO parts were reduced in the acid and became hydrophobic. The hydrophilic regions could readily absorb water and swell, and the hydrophobic rGO parts remain unchanged to the moisture variation. As the GO swelling could be restricted when exposed to the infrared (NIR) radiation, the patterned GO-PDA/rGO papers could be bend and unbend under an on-and-off NIR light, and were fabricated as a walking device and an artificial hand.

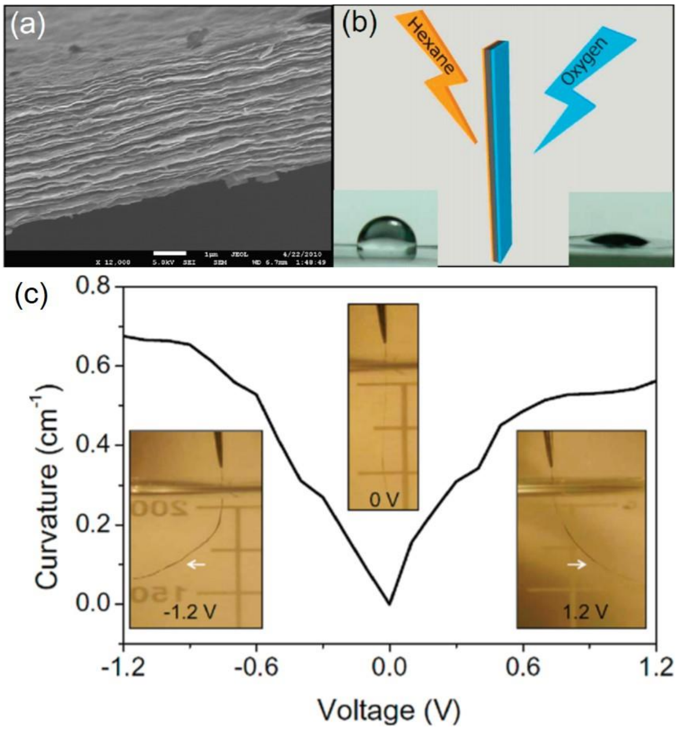

Figure 2.9 a) SEM image showing the cross-section of the rGO film (scale bar: 1 μm). **b)** schematic diagram of the asymmetric plasma treatments on the rGO film with hexane and oxygen. Insets: the surface wettability of the corresponding face after treatment. The water contact angles for the hexane plasma treated side is 90°, while that for the oxygen plasma treated side is 15°. **c)** The curvature change of the asymmetrically-modified rGO strip as a function of applied CV potential within ±1.2 V. Insets: digital images showing the status of the rGO strip when the applied potential was 1.2, 0, and 1.2 V, respectively. [153]

2.9 Conclusions and summary of research gaps

In this chapter, we have reviewed the fundamental theory, structure simulation, materials preparation (Figure 2.10), and applications of modified graphene-based 2D materials. To highlight, the major applications of 2D graphene-based materials falls into two areas: flexible and lightweight semi-conducting/ conducting materials in micro-scale electronics, and moisture driven actuators with amphiphilic structures.

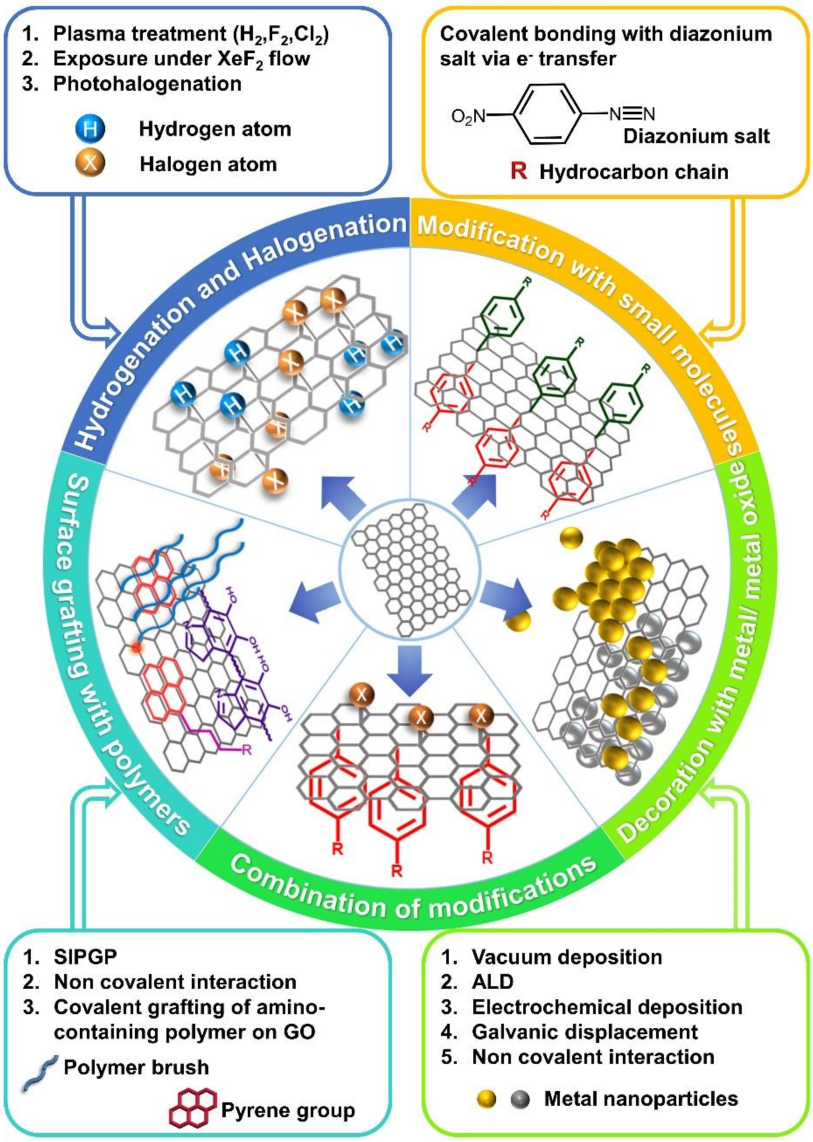

Figure 2.10 Schematic diagram showing different common routes for functional graphene-based 2D objects.

In conclusion, a wide range of functional graphene-based materials with different shapes, sizes, and compositions can be customized and fabricated via surface functionalization on graphene and its derivative. All the modifications mentioned above did enrich the surface functionality of the biologically- and chemically-inert pure graphene, as well as enhanced its electronic performance. These allowed the assembly and use of graphene systems in a wide range of applications, e.g., sensing, cell manipulation actuators and electronic devices.

From the chemical point of view, band structure of graphene can be modified through the atomic functionalization, such as the insertion of hydrogen and halogen atoms on graphene planes, and the chemical reactivity of graphene surface could also be managed by covalent grafting with ligands or polymers. However, there is an unsolved drawback for these covalent fabrication approach towards functional graphene-based materials, which is the damage towards the natural conjugated structure as well as sacrificing electronic merits of pristine graphene

The research gaps of the fabrication and application of ultrathin graphene-based materials are listed as follow:

1. When the applications were demonstrated with modified graphene sheets were based on GO or rGO instead of graphene, superior transparency, conductivity, and few-atoms thickness of graphene could not be realized. But the applications of modified single-to-few layer CVD graphene are still limited.

2. The fabrication of chemically reactive graphene-based materials via covalent modifications destroys the conjugation of the basal plane, which sacrificed the major electronic merits of graphene. Although there have been several efficient covalent routes developed for transforming graphene into a desire functional state that suitable for a specific application, such technologies are not suitable for sensitive device which require conductive substrates. Therefore, facile non-covalent

approaches are needed for modification of graphene, such as the modification realized via π-π interaction between pyrene groups and graphene's basal plane, or Van der Waal's force between graphene and metal particles physically deposited on top.

3. As polymeric protection layer on top of CVD graphene is always needed for dry or wet-transfer of graphene, the transferred modified graphene samples could be contaminated by any unremoved polymeric substance. Consequently, the resulted reactivity and electronic performance of the modified graphene layer would be lowered. Hence, extra and comprehensive rinsing steps are required. As the polymer layer is always spin-coated on top of graphene, they still sacrificed the nano-scale thickness of the graphene film even conductivity is not a concern of some cases.

4. The transparent CVD graphene film shows a great potential as the top electrode for flexible thin-film optical electronics. However, it obtains a relatively low conductivity among the transparent electrodes including metal meshes and conductive polymers. A combination of graphene with the others could be used to fabricate transferrable and highly conductive transparent electrodes for efficient devices.

CHAPTER 3 METHODOLOGY

3.1 Transfer of modified-CVD graphene films.

Copper (Cu) foil was etched away by placing the modified CVD graphene@Cu sample onto the surface of $FeCl_3$/deionized water solution (50 mg/ml) for 2 hours. The freely floated modified graphene films were fished by a glass slide, and transferred onto the deionized water for rinsing to remove any residue left after the Cu etching process. After three times of rinsing, the modified graphene films were fishes by the target substrate and allowed to be dried via 65 °C heating on a hot plate for 10 minutes.

3.2 Optical Microscopy

Optical microscopy adopted in this research refers to the light microscope, magnifies the image of samples by adopting groups of lenses under visible light. In aids with a 10X ocular lens, the final magnifications of the optical microscopy ranges from 50X to 2000X.

3.3 Atomic Force Microscopy (AFM)

AFM is a type of high-resolution scanning probe microscope (SPM), which images a surface by scanning through with a sharp tip with nanoscale radius fixed on one end of the cantilever, and it is well-controlled by coping with computerized feedback mechanisms and imaging software. When the tip approaches to the sample surface, the tip and cantilever will be pulled by the sample when they are close enough, which resulted in the atomic attractive force. While the tip getting closer to the surface, the repulsive force will also increase dramatically, and pushes the tip away. Also, there is a laser always focusing on the cantilever, that the reflected beams are recorded by a position-sensitive photodetector. Therefore, the surface topography of the samples are recorded by the variation of the reflected light spot.

In these days, there are three basic modes of AFM: the contact mode, which the tips contact the sample surface during whole scanning process; the non-contact mode, which the photodetector records the vibration of the cantilever caused by the attractive force between tip and sample; for the tapping mode, the tip is oscillating at a given frequency away from the surface.

3.4 Attenuated Total Reflectance Fourier Transform Infrared Spectroscopy (ATR-FTIR)

Fourier transform infrared spectroscopy (FTIR) is a useful tool for charactering the chemical composition of materials. But traditional FTIR with transmission method which require measuring sample in powder (tablet) form is insufficient for bulk solid samples, fibres, surface coatings or samples that do not pulverized easily. To overcome these problems, attenuated total reflectance (ATR) accessory of FTIR was developed in 1980s. When a light beam travels from a more reflective medium to less refractive medium and the angle of incidence is larger than the critical angle, the light beam will be 'totally reflected'. Critical angle refers to θc:

$$\theta c = sin^{-1} \eta 2 / \eta 1 \tag{1}$$

where $\eta 1$ is reflective index of more refractive medium and $\eta 2$ is refractive index of less refractive medium.

The ATR technique involves a highly refracting prism which would be bought into an intimate contact with the measured sample. An IR light beam is then directed to the prism/sample interface at incident angle larger than the critical angle. In this case, the evanescent wave travel into the surface layer of the sample, the absorptions signals are therefore shown in the reflection spectrum. Therefore, the ATR-FTIR obtains the surface chemical information from the signals of internally reflected IR beam which meets the sample surface.

3.5 Ultraviolet-Visible Spectroscopy (UV-Vis)

Ultraviolet-visible spectroscopy (UV-Vis) refers to the absorption and reflectance of light by the samples in range of visible light to ultraviolet light. UV-Vis is widely adopted in analytic chemistry for quantitative characterization. For example, to determine the color and concentration of metal ion solutions, as this characterization method obey the Beer-Lambert law, which refers to the absorbance of samples is directly proportional to the concentration of the light absorbing species. Also, conjugation degree of organic compounds, and the optical transmittance thin film materials are always determined by UV-Vis via comparing the intensity of the light passing through the reference with that pass through the samples.

3.6 Scanning Electron Microscopy (SEM)

Scanning electron microscopy (SEM) is a tool that obtain sample image via scanning a high energy focused electron beam over the sample surface. The incident electron beam scattered in the sample, both elastically and inelastically, which generate a variety of signals, such as the secondary electrons that are generated from the collision between incoming electron with the loosely bounded outer electron on the sample surface; backscattered electrons which is the escaped incident light retarded by the electro-magnetic field of the nucleus and scatted with an angle > 180°; and X-rays emitted from the samples during bombardment by an electron beam.

Through the secondary electron detector equipped in the SEM, the surface profile of the sample can be determined by counting the collected electrons. Such interaction volume directly proportional to the acceleration voltage but indirectly proportional to the atomic number of the sample. The resolving power of average instruments is in the range of 1-5 nm. Most of the modern SEM nowadays is equipped with energy dispersive x-ray spectroscopy (EDS), which detects X-rays emitted from the samples to characterize the elemental composition of the analyzed volume.

3.7 Raman Spectroscopy

Raman spectroscopy is non-destructive and non-contact tool that widely used in identifying specific structures of molecules by inelastic scattering of monochromatic light, which is usually a laser in a range of visible light to near ultraviolet light. Under the illumination of laser beam, the vibrational, rotational and other low-frequency modes could be revealed, via the energy shift of the laser photons.

3.8 X-Ray diffraction (XRD)

X-Ray diffraction (XRD) characterize a sample by measuring the X-ray scattering from crystalline materials. The X-ray beams reflected by the atomic plane of a crystal always interfere with one another as shown in Figure 1.1, like the two parallel incident rays 1 and 2 make an angle (θ) with the planes.

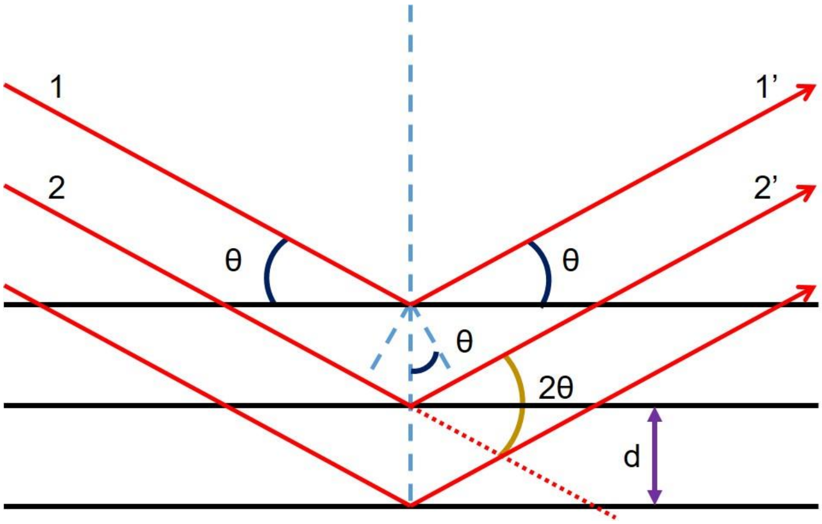

Figure 3.1 Structural characterization of thin film by X-ray diffraction (XRD)

Reflected beam with maximum intensity will be resulted only if the waves 1' and 2' are in phase. The difference in path length between 1 and 1', or between 2 and 2' must be an integral number of wavelength (λ). This relationship could be expressed mathematically in Bragg's Law:

$$2\mathrm{d} \sin \theta = n \lambda \tag{2}$$

Where the variable d is the distance between atomic layers in crystal, and λ is the wavelength of the incident X-ray beam, n is an integer.

The angle of the reflected beam leaving the planes is set as angle θ, and extend to 2 θ as the angle between the reflected light and original path of the incident beam. The possible d-spacing defined by the indices h, k, l are determined by the shape of the unit cell:

$$\sin\theta = \lambda/2d \tag{3}$$

The possible 2 θ value are determined by the unit-cell dimensions, while the intensities of the reflections are determined by the electron distribution in the unit-cell. Therefore, each material produces a unique fingerprint of X-ray intensity versus scattering angle, determined by its crystalline atomic structure. Hence, conducting qualitative analysis of each material is possible by comparing its XRD pattern to the corresponding patterns in the XRD library.

3.9 Transmission electron microscopy (TEM)

Transmission electron microscopy (TEM) is an efficient and versatile technique for the characterization of materials, it has the ability to obtain full morphological (grain size, grain boundary and interface, phase distribution and defects etc.) data from the samples. Detailed analysis of materials about the crystallography, atomic structure, electronic structure and coordination number could also be obtained by using TEM

For the TEM imaging, there are two major principle kinds: diffraction contrast imaging, and phase contrast or high-resolution imaging (HRTEM). Diffraction imaging includes the bright field and dark field imaging, which use transmitted or diffracted beam respectively and remove all other beams from the image by the use of objective aperture. On the other hand, the phase contrast imaging approach makes use of a large object aperture, combining phase and intensity of diffracted and non-diffracted beams to form a phase contrast image.

3.10 Current-Voltage (I-V) Characterization of Solar Cells

To measure the photovoltaic performance of a solar cell under the irradiation of light, and to determine its corresponding diode characteristics under dark state, a sourcemeter equipped with a solar stimulator was used to measure the *I-V* curves of the device. In this research project, the areal power rate of the simulated sunlight from is set as 100 mW/cm^2, when the sourcemeter applies a bias on the solar cell from negative to positive or vice versa, the current that passes through the solar cells is recorded in form of the I-V curves.

CHAPTER 4 GRAPHENE-SUPPORTED UNLTRATHIN FUNCTIONAL POLYMER FILMS

Different modifications that have been done on graphene to fabricate functional surface as well as free-standing 2D objects were discussed in Chapter 2. And the short comings of implying covalent functionalization on graphene were mentioned. In this chapter, a new strategy of fabricating a functional organic 2D material, the polymer@graphene 2D objects, were introduced. Various kinds of polymer brushes were tethered on graphene sheets via the non-covalent π-π interaction. The functionalities, patterning and applications of these graphene based organic 2D materials were also demonstrated.

4.1 Introduction

2D organic materials like 2D polymers, especially for quasi-2D polymers were investigated continuously for their great potential on surface modification as well as high feasibility on various chemical and biological applications such as separation membranes, smart surfaces, sensors, catalysis, and drug delivery[155-164]. Previous approaches to fabricate quasi 2D polymers include the layer-by-layer assembly[165,166], Langmuir–Blodgett[167,168], self-assembly of block copolymers[169-171], interfacial polymerization[172-174], and spin-casting method[175,176], which are rely on the cross linking of polymer thin films, making the quasi 2D polymers undesirable for sensitive response to external stimuli; obtaining high- density functional groups or patterning. Recent studies show that polymer brushes are more suitable materials for quasi-2D polymers. The strategy is to anchor polymer brushes on an ultrathin and soft substrate, such as Au and crosslinked self-assembled monolayers, via covalent bonds. But such a covalent strategy leads to limitation in the flexibility of materials synthesis, functionalization, and patterning. As a result, there is still a large room for further investigation of effective production of quasi 2D materials as well as their practical applications[159].

In contrast, mono-to-few layer CVD graphene is well-known of its few-atom-thick thickness, excellent optical transparency and flexibility, while could be transferred on arbitrary upon polymeric protection layer, and it is patternable via several lithography or laser approaches.

Therefore, here we combined the polymer layers and CVD graphene to fabricate the polymer@graphene 2D objects, which is a transferable, ultra-thin, transparent and flexible graphene based 2D organic film. A series of homogenous and patterned graphene based 2D polymer films were fabricated via the strong and non-covalent interaction approach, which relied on π-π interactions between the basal plane of graphene and functional group on the polymers layers, e.g. pyrene groups on the atom transfer radical polymerization (ATRP) initiator and co-polymer layers. We believed that the resulted polymer@graphene 2D objects could help to develop a more flexible, transferrable and pattern capable bio- and chemical reactive materials comparing to the existing ones. From the abundant choice of possible monomers, we demonstrated the fabrication of four different polymer@graphene 2D objects with tunable polymer thickness and functionality.

4.2 Experimental section

4.2.1 Materials preparation

CVD-grown graphene sheets grown on Cu foil were supplied by Apex Graphene Technology CO., LTD. Macro-initiator was supplied by Prof. Feng ZHOU from Lanzhou Institute of Chemical Physics.

Iron (III) chloride ($FeCl_3$), copper(I) bromide (CuBr), 2, 2’-bipyridyl (bipy), monomers including: methyl methacrylate (MMA), glycidyl methacrylate (GMA), (2-(methylacryloyloxyl) ethyl) trimethylammonium chloride (METAC), poly (ethylene glycol) methyl ether methacrylate (OEGMA), 1-pyrenemethanol, trimethylamine and methacryloyl chloride (98%), 2-methoxyethanol (anhydrous) and ammonium tetrachloropalladate (II) (97 %) were purchased from Sigma-Aldrich.

Cupric sulfate ($CuSO_4 \cdot 5H_2O$), sodium hydroxide (NaOH), potassium sodium tartrate and formaldehyde (HCHO) were purchased from Uni-chem.

Organic solvents such as acetone, ethanol, isopropanol, methanol and N, N-dimethylformamide (DMF) were used as rinsing medium.

4” Silicon (Si) wafers and 300 nm silicon dioxide (SiO_2) deposited-Si substrates were purchased from Semiconductor Wafer, Inc., Au (300nm) substrate were fabricated via thermal deposition on Si wafer. Poly (ethylene terephthalate) (PET) film, polytetrafluoroethylene film (PTFE) were supplied by DuPont Teijin Films.

DNA oligonucleotides were purchased from Takara (Dalian, China). The target sequence was 5’-NH2-(CH2)6-CAT GAT TGA ACC ATC CAC CA-TET-3’ and the probe sequence was 5’-TAMRA-TGG TGG ATG GTT CAA TCA TG-3’.

4.2.2 Macro-initiator assembly on CVD graphene

The macro-initiator was first dissolved in dimethylformamide (DMF) (2 mg/ml), and the Cu foil supported CVD graphene film was immersed in the solution for 24 hours in the dark at room temperature. The graphene sample was then rinsed with DMF and acetone to remove physically adsorbed macro-initiator, and allowed to dry under N_2 gas flow.

4.2.3 Surface-initiated Atom Transfer Radical Polymerizations (SI-ATRP)

All the SI-ATRPs were performed in Schlenk tubes. Polymerization recipes for the six kinds of polymer: poly (glycidyl methacrylate) (PGMA), poly (methyl methacrylate) (PMMA), hydrophilic poly[(2-(methylacryloyloxyl)ethyl) trimethylammonium chloride] (PMETAC), poly(oligo(ethyleneglycol) methacrylate) (POEGMA), were listed as follows:

1. For PGMA: Deionized water/methanol mixture (30 ml, 1/4 v/v) was added to GMA (6 ml) in a Schlenk tube, under the nitrogen (N_2) gas flow, CuBr (63 mg) and bipy (0.17 g) were added and dissolved. After the solution changed into dark-brown color, which indicated the start of polymerization, the solution was then transferred into a 50-ml centrifuge tube, heated in a water bath ~37 °C for 50 minutes. The graphene

sample was then rinsed with methanol and deionized water, and dried with compressed air.

2. For PMMA: Deionized water/methanol mixture (30 mL, 1/4 v/v) was added to MMA (6 ml) in a Schlenk tube, under the nitrogen (N_2) gas flow, CuBr (0.14 g) and bipy (0.3 g) were added and dissolved. After the solution changed into dark-brown color, the solution was then transferred into a 50-ml centrifuge tube, heated in a water bath ~30 °C for 45 minutes. The graphene sample was then rinsed with methanol and deionized water, and dried with compressed air.
3. For PMETAC: Deionized water/methanol mixture (9 ml, 2/7 v/v) was added to METAC (6.9 g) in a Schlenk tube, under the nitrogen (N_2) gas flow, CuBr (0.135 g) and bipy (0.36 g) were added and dissolved. After the solution changed into dark-brown color, the solution was then transferred into a 15-ml centrifuge tube, placed in room temperature overnight. The graphene sample was then rinsed with methanol and deionized water, and dried with compressed air.
4. For POEGMA: Deionized water/methanol mixture (12 ml, 1/3 v/v) was added to OEGMA (4 ml) in a Schlenk tube, under the nitrogen (N_2) gas flow, CuBr (70 mg) and bipy (0.156 g) were added and dissolved. After the solution changed into dark-brown color, the solution was then transferred into a 50-ml centrifuge tube, heated in a water bath ~40 °C for 50 minutes. The graphene sample was then rinsed with methanol and deionized water, and dried with compressed air.

4.2.4 Monomer Assembly for Copolymer Synthesis

The 1-pyrenemethyl methacrylate (PMA) monomer was first synthesized through an alcoholysis reaction. Briefly, 1.16 g 1-pyrenemethanol and 0.55 g triethylamine were dissolved in 40mL dichloromethane (DCM), followed by adding 0.5 g methacryloyl chloride into the solution drop wise. The reaction was proceeded overnight at 0 °C under vigorous stirring. The solution was washed three times by 2 M hydrochloric acid (HCl) solution, saturated sodium bicarbonate ($NaHCO_3$) solution and deionized water, separately. Finally the solvent was evaporated and the co-polymer product (green solid) was dried under vacuum.

4.2.5 Synthesis of copolymer solution

The poly (1-pyrenemethylmethacrylate)-poly[2-(methacryloyloxy)ethyltrimethyl-ammonium chloride] (PPMA-PMETAC) copolymer was synthesized through radical polymerization. Firstly, anhydrous METAC solid was precipitated from METAC solution (80%) by adding acetone. Then 0.48 g PMA monomer, 1.87 g METAC and 9 mg azobisisobutyronitrile (AIBN) were added in 40 ml 2-methoxyethanol (anhydrous) under stirring. After all the solutes were dissolved, the solution was heated at 80 °C under N_2 gas protection for twenty hours. Resulted light-yellow solution was then stored under dry and dark environment.

4.2.6 Preparation of Cu plating bath

The Cu plating bath consisted of a 1:1 mixture of newly prepared solution A and B. Solution A was prepared by mixing $CuSO_4 \cdot 5H_2O$, (12 g/L), NaOH (12g/L), and potassium sodium tartrate (27 g/L) in deionized water. Solution B was a formalin (45 ml/L). Both solutions were filtered through 0.45 μm PTFE filter before use.

4.2.6 Growth of Cu layer on copolymer (PPMA-PMETAC) coated CVD graphene

PPMA-PMETAC copolymer were dropped onto CVD graphene followed by spin-coating. The sample was then dried by heating at 80 °Cfor 10 minutes. The copolymer-coated graphene@Cu foil was then transferred onto target substrate via the wet-etching and transfer process mentioned above. And the transferred sample was then immersed in ammonium tetrachloropalladate (II) solution for an hour. After that, the sample was immersed in freshly mixed Cu plating bath, and was taken out after 3 minutes.

4.3 Results and discussions

4.3.1 Fabrications and characterizations of the polymer brushes grafted graphene film

As shown in figure 4.1 a, CVD graphene film grown on Cu foils were decorated with polymer brushes via adopting a specific ATRP macro-initiators, the poly [2-(2-

bromoisobutyryloxy) ethyl methacrylate-co-4-(1-pyrenyl) butyl methacrylate] (Figure 4.1 b). Such an initiator was found to be anchored onto the graphene due to the strong interaction between pyrene side chains from the initiator, with the graphene basal plane, as indicated in previous studies[177,178].

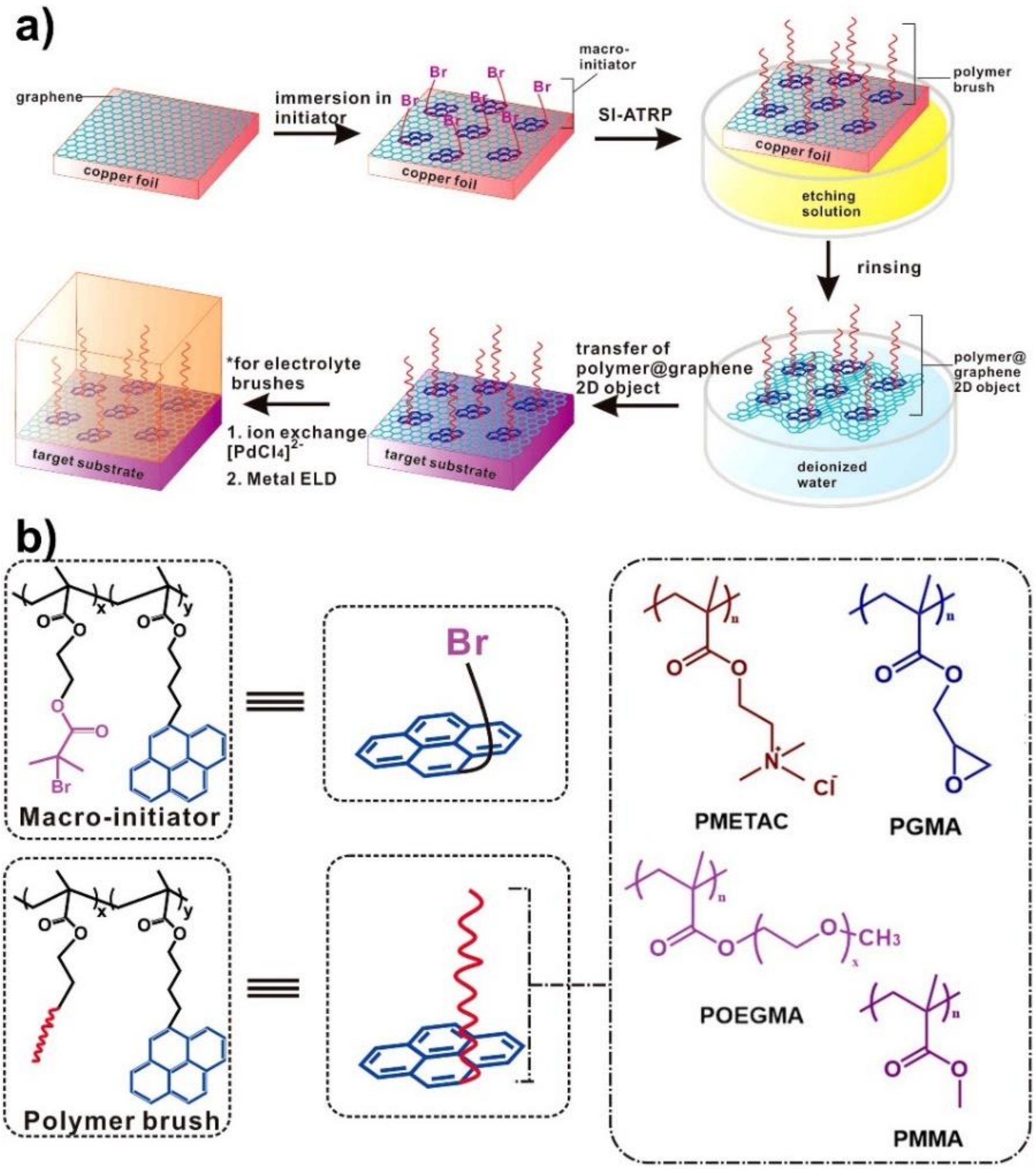

Figure 4.1 **a)** Schematic diagram of the fabrication and transfer process of polymer brushes@ CVD graphene objects. **b)** Chemical structures of the macro-initiator and polymer brushes.

Various polymer brushes were grafted on the initiator-soaked CVD graphene layer, and it was found that for the PMMA and PGMA brushes grafted graphene films, the polymer brush layers were densely grafted whilst also protecting graphene during the wet etching and transfer process. However, PMETAC and POEGMA brushes-grafted graphene films could not be wet-transferred without a protective polymeric layer spin-coated on top, which was due to their hydrophilic nature[179,180]. From the digital and microscopic images of the polymer@graphene 2D object transferred on SiO_2 wafer, textile fabrics, Au coated Si wafer and PTFE substrate, no obvious damages like cracks were observed (Figure 4.2).

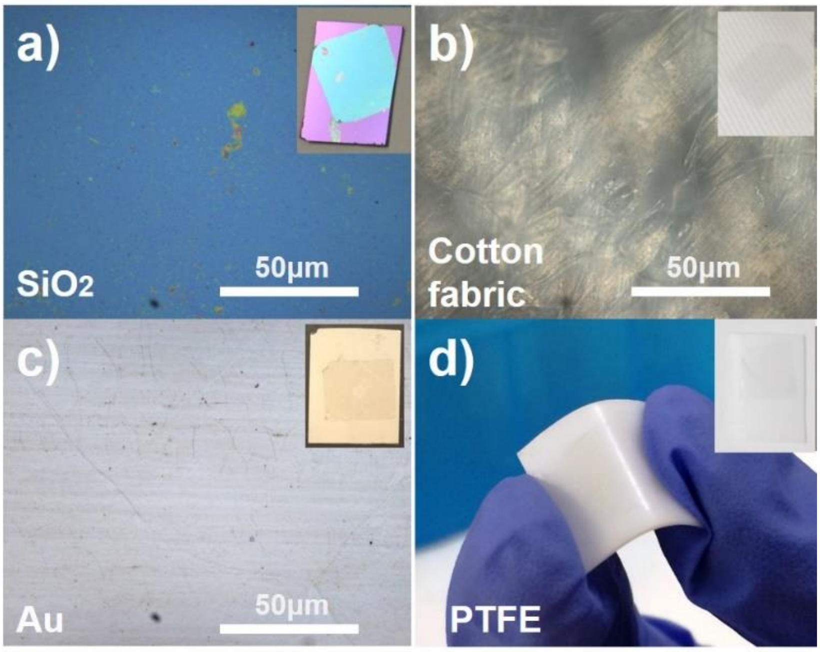

Figure 4.2 Digital images of transferred PMMA@G objects on different substrates, including **a)** SiO_2 wafer; **b)** cotton fabric; **c)** Au wafer and **d)** PTFE film.

After conducting various SI-ATRPs for grafting different polymer brushes on CVD graphene sheets, we to ensure that if such surface modification on CVD graphene surface is really feasible. Moreover, the physical properties of polymer layers as well as their underlying chemistry were also needed to be investigated. Therefore, as the first step of this studies, all the polymer brushes@CVD graphene (polymer brushes@G) films were first transferred onto target substrates and were checked under the attenuated total reflection Fourier transfer infrared spectroscopy (ATR-FTIR).

According to the ATR-FTIR spectrum, all the functional groups presented on the samples, as well as the presences of polymer brushes, could be determined. As shown in figure 4.3 a, the spectrum in the middle corresponding for PMMA@G sample consists of the obvious peak at 1108 cm^{-1} assigned to C−O−C groups; peak of C=O stretching of ester group at 1738 cm^{-1} and alkane C-H bonds stretching at 2850 cm^{-1}; which indicated the successful grafting of PMMA brushes[181,182]. Similarly, for the spectrum of PGMA@G and POEGMA@G samples, main feature peaks of PMMA are also present, in addition, C-O stretching of epoxy group at 907 cm^{-1} became the evidence of the successful grafting of PGMA brushes[183,184]; and the increase of intensity of C-O-C peak shown the presence of POEGMA brushes[185-187]. For the spectrum of PMETAC@G sample, peaks of 1486 cm^{-1} representing (CH3)$_4$N$^+$ bond bending vibration and 1728 cm^{-1} representing C=O bond stretching appeared and proved the successful grafting of it on the CVD graphene surfaces[188,189]. Distinctive peaks with corresponding binding energies and elements were further summarized in Table 1.

Polymer brushes @ CVD graphene films	**Wavenumber (cm^{-1}) of distinctive peaks of polymers**	**Corresponding functional groups**
PMMA@G, **PGMA@G,** **POEGMA@G**	~1108 ~1738 ~2850	C-O-C C=O C-H
PGMA@G	907	C-O (epoxy group)
PMETAC@G	1486 1728	$(CH_3)_4N^+$ C=O

Table 1. Summary of the ATR-FTIR data of the polymer brushes @ CVD graphene films on target substrates.

Furthermore, to check if this modification is a damage-free approach to CVD graphene film, Raman spectroscopy was carried out for investigate the completeness of graphene layer after the polymerization and transferring process. From figure 4.3 b, the resulted Raman spectra showed that D, G and 2D peaks of graphene appeared on all polymer brushes@G films; while the peak ratios and positions did not show obvious differences, suggesting that our synthesis, etching and transfer process did not destruct the basal plane structure of graphene.

By adopting the atomic force microscope (AFM), thicknesses of pure mono-to-few layer CVD graphene film, POEGMA@G, PMETAC@G, PMMA@G and PGMA@G films could reach 4, 24, 26, 103 and 115 nm, respectively (Figure 4.3 c). However, except PMMA@G samples, all of the samples exhibited a roughness higher than 40%. Further improvements of the film roughness could be achieved by further investigation of optimum thickness of each types of polymer brushes, which was determined by the polymerization kinetic, but as we did not vary the brush thickness in detail in this work.

On the other hand, all polymer brushes@G films were found to exhibit high transparency over 80 % when wavelength equals to 550 nm (Figure 4.3 d). The absorbance of light was found to be different among the four samples in this sequence: PGMA≈PMMA >PMETAC >POEGMA, which was same as the sequence of their corresponding thicknesses. Therefore, in general, the thicker the polymer brushes we grew, the stronger is the absorption of optical light. As the mono-to-few layer CVD graphene sheets adopted here were mostly 2-3 layered thick, and they absorbed ~7 % of the optical light, the actual light adsorption contributed by the polymer brush layers were only ~5~12 %.

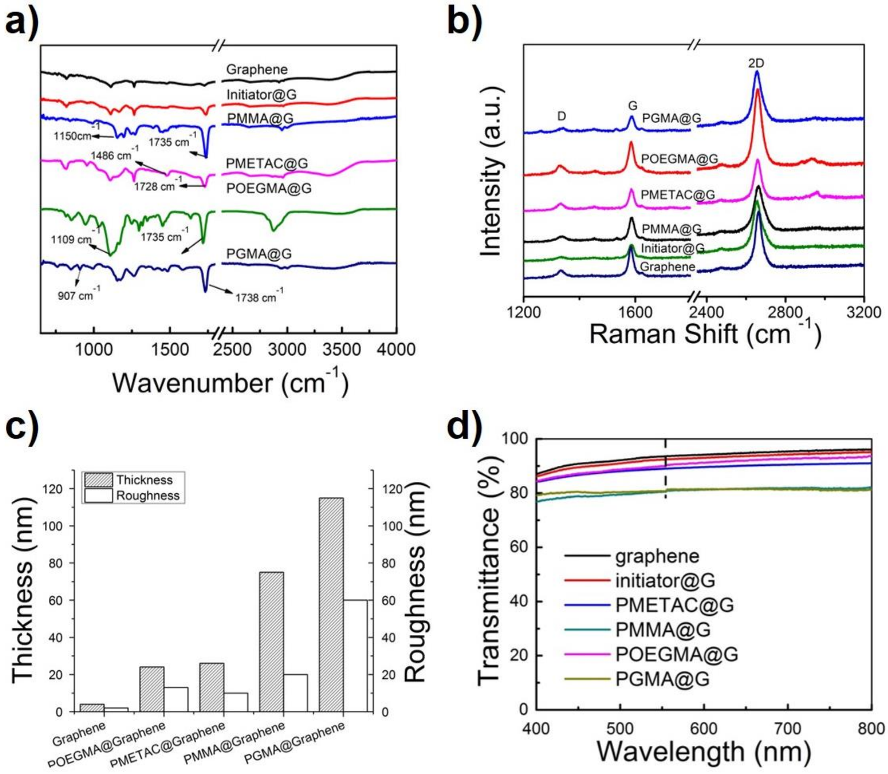

Figure 4.3 Characteristics of polymer brushes@G films transferred on SiO2 substrate. **a)** ATR-FTIR spectrum, **b)** Raman spectrum and **c)** graph showing thickness and roughness of the series of polymer brushes@G films transferred on SiO_2 substrate. **d)** Transmittance of light of the series of polymer brushes@G films transferred on 125 µm PET substrate.

As wettability of each type of polymer brushes layer carried different functional groups, water contact angle measurements of the polymer brushes@G films were conducted. Static sessile drop method was adopted to measure the water contact angle in the experiments: dropping a 5 µl water droplet onto the polymer brushes@G film which had already been transferred on a suitable wafer (SiO_2 or Au coated Si wafer in this experiment). As depicted in figure 4.4, the differences of water contact angles among graphene and polymer brushes@G objects were obvious. For pristine CVD graphene, water contact angle of Graphene@SiO_2 wafer sample was found as ~90°. After the grafting of polymer brushes, all the water contact angle measurement values were smaller than the pristine graphene film, showing that all the polymer brushes grafted on top made the graphene surface more hydrophilic. The water contact angles for PMMA, PGMA and POEGMA grafted surface were observed as 80°, 77° and 45° respectively. Furthermore, the water contact angle of PMETAC@G could not be observed via this measurement, and such a large decrease in water contact angle of PMETAC-grafted graphene surface was due to the highly hydrophilic nature of the PMETAC brushes.

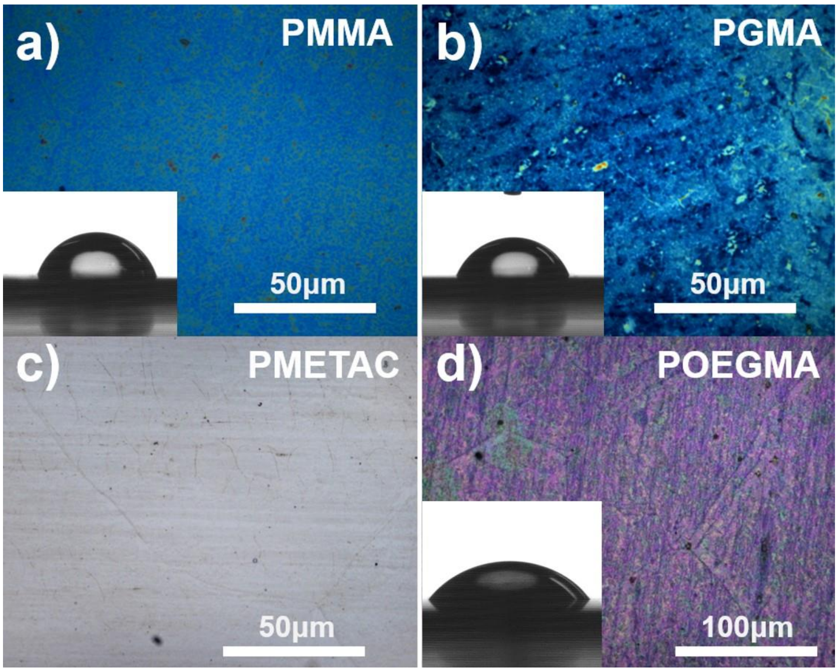

Figure 4.4 Optical images of **a)** PMMA@G and **b)** PGMA@G films t, **c)** PMETAC@G film transferred onto Au coated Si wafer, and **d)** POEGMA@G film ransferred on SiO_2 wafer. Insets: water contact angle of the corresponding samples.

4.3.2 Patterning and application of the polymer brushes grafted graphene film

By utilizing the PMMA@G objects which have the lowest roughness among all the polymer brushes@G samples, femtosecond laser was used to pattern the PMMA@G films supported by Cu foil by generating square and dot holes on them. After the etching of Cu foil and 3 times of rinsing with deionized water, the patterned PMMA@G films were transferred onto Si substrate. The as-made patterns with uniform 50 µm squares and 5 µm circles (Figure 4.5) were observed clearly under the optical microscope. Patterns distributed regularly on the substrate with a constant depth of ~43 nm was also measured with the aid of AFM.

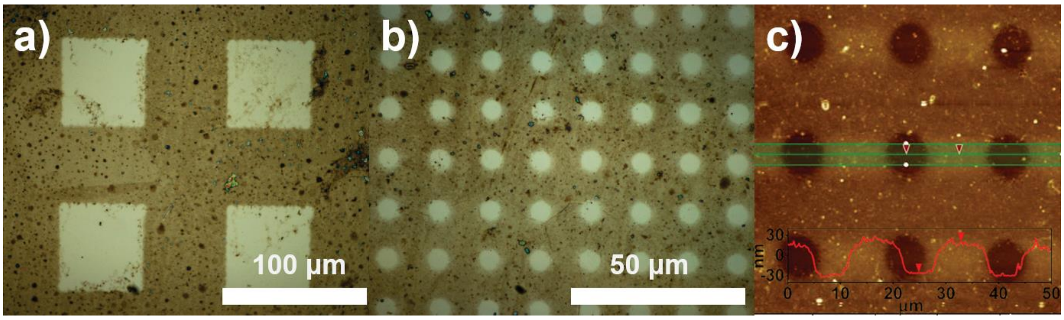

Figure 4.5 a-b) Optical images and **c)** AFM images of patterned PMMA@CVD graphene films transferred on Si substrate.

From previous researches, PGMA was proved to react with amines effectively and it has been used for immobilizing different kinds of proteins, DNAs and enzymes[190,191]. In order to investigate the reactivity of PGMA brushes grown on CVD graphene, we transferred the PGMA@G films onto PET films, and check if they could act as a reactive transparent platform for the immobilization of DNA strands.

Here, the arrays of 5'-amino-modified, 3'-TET-labeled single strand DNA oligonucleotides (TET-ssDNA) were inkjet-printed onto PGMA-G, followed by overnight incubation, in which TET-ssDNA covalently bonded to the PGMA brushes through the ring-opening reaction of epoxy groups (Figure 5g). After rinsing away the physically adsorbed molecules, green fluorescence patterns were clearly seen under blue light excitation (Figure 4.6 a & b), and the thickness of the TET-ssDNA attached on the PGMA brushes was found to be ~20 nm (Figure 4.6 c). Then the TET-ssDNA was subsequently hybridized with its complementary strand by immersing the whole sample into a 100 nM 5'-TAMRA-labeled complementary DNA oligonucleotide (TAMRA-cDNA) solution for 7 hours at 45 °C. After the hybridization and rinsing processes, orange fluorescence patterns were observed due to Forster resonance energy transfer (FRET), and the thickness of the area with printed-TET-ssDNA increased for ~100 nm. These changes did suggest that a successful hybridization of the two complementary oligonucleotide strands (Figure 4.6 d, e & h) was carried out.

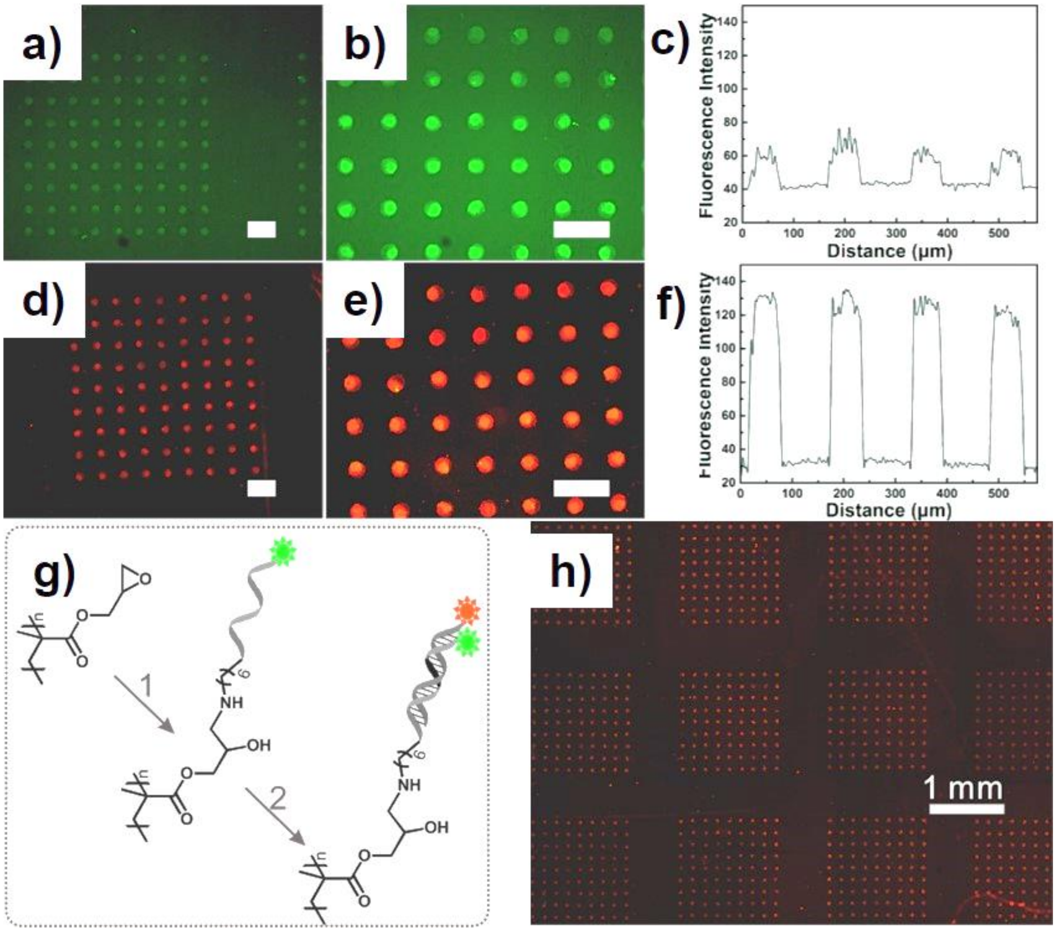

Figure 4.6 a & b) Fluorescent microscopic images of the fluorescence intensity of 5'-NH2, 3'-TET-modified ss-DNA bounded with PGMA@G with **c)** the corresponding cross-section analysis. **d & e)** Fluorescent microscope images of fluorescence intensity after hybridization with 5'-TAMRA-labeled complementary probes with **f)** the corresponding cross-section analysis. (The inserted scale bars equal to 200 μm.) **g)** Molecular structure illustration of the DNA binding and hybridization process on the layer of PGMA brushes. **h)** Microscope image of immobilized DNA arrays on the surface of PGMA@G film transferred on a 125 μm PET substrate.

4.3.3 Co-polymer coated- CVD graphene film and characterizations

In the previous part, we found that the PMETAC brushes grafted CVD graphene could not be transferred without spin-coated PMMA layer protection, which lead to an extra rinsing process after the wet-transfer process, and any PMMA residue would lower the chemical reactivity and surface hydrophilicity of the PMETAC@G films. Therefore, we synthesized a copolymer terminated with pyrene group and PMETAC group on the two ends. A uniform copolymer layer was found on the CVD graphene after 1 minute spin coating (3000 round/min) as shown in figure 4.7.

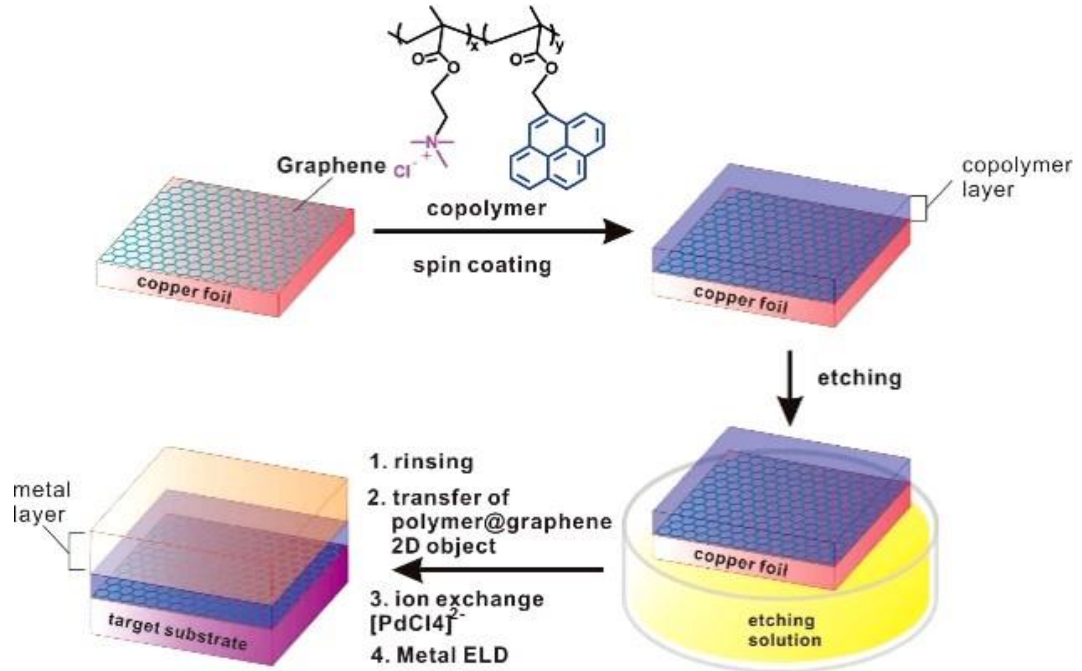

Figure 4.7 Schematic diagram of the fabrication and transfer process of copolymer@ CVD graphene films.

To investigate the ability of the copolymer layer of anchoring on CVD graphene surfaces well as its physical and chemical properties, the samples were first investigated under the ATR-FTIR characterizations. From figure 4.8 a & b, both spectrum of PMETAC@G sample and copolymer@G sample transferred on SiO_2 substrates showed the obvious peak at 1486 cm^{-1} representing the $(CH_3)_4N^+$ bond bending vibration, and the other peak at 1728 cm^{-1} representing C=O bond stretching. The PMETAC group, as well as the copolymer layer, were therefore confirmed to be successfully anchored on the graphene surface.

The transmittance of the copolymer@G samples was also measured, as shown in figure 4.8 b, the copolymer@G samples processed a transparency only 1-2% higher than that of pure CVD graphene sample. As the thickness and roughness of copolymer@G were found to be 26 nm (Figure 4.8 c), the copolymer layer was determined to exhibit a high transparency with a film thickness ~26 nm. Moreover, the roughness (Rq) of the transferred copolymer@G on Si wafer was measured as 9 nm (35%), indicated a smoother surface was achieved when compared with the PMETAC@G films fabricated via SI-ATRP method.

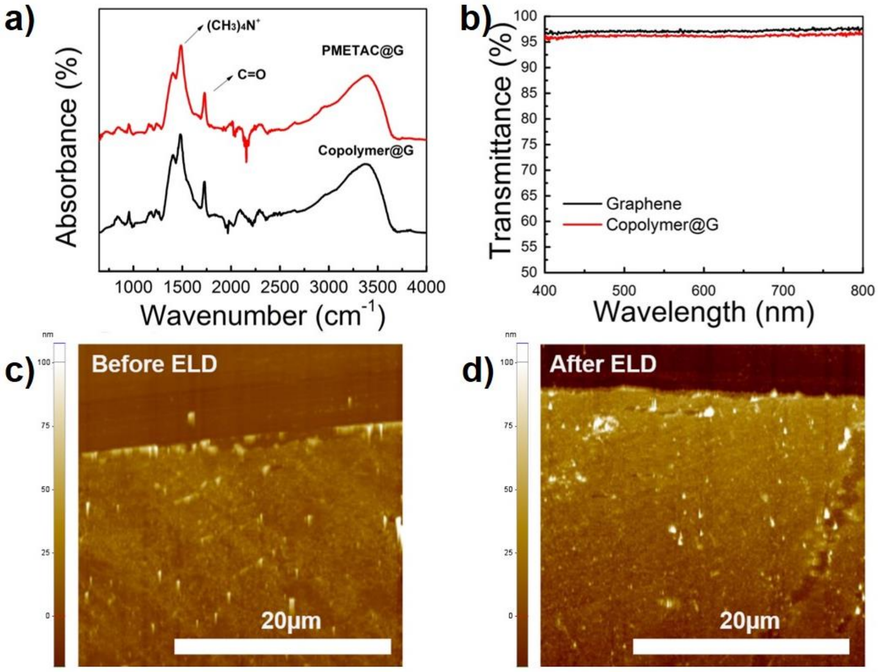

Figure 4.8 Characteristics of copolymer @G films transferred on target substrates. **a)** ATR-FTIR spectrum of copolymer@G films transferred on Au coated Si substrate. **b)** Transmittance of light of pristine CVD graphene and copolymer@G films transferred on 125 μm PET substrate. AFM images of copolymer@CVD graphene **c)** before and **d)** after Cu ELD processing on SiO_2 substrates.

Moreover, metal electroless deposition (ELD) of copper (Cu) was also performed after the copolymer@G films were transferred onto target substrates. Furthermore, after the ELD process of Cu, the thickness of the samples increased to 85 nm with a roughness of 30 nm (Figure 4.8 d), where the roughness of the samples kept constant after the deposition of metal particles was carried out. Moreover, the Cu particles were found to be attached on the samples with good solvent stability, thus further confirmed the spin-coating of copolymer is a feasible surface modification towards CVD graphene surfaces.

As the Cu coated graphene objects were fabricated with acceptable roughness and uniformity, it could be considered as a potential electrode material on flexible/stretchable devices, thus the mechanical flexibility of such samples were tested. Bending test was adopted to evaluate the mechanical stability of Cu@G objects transferred on PET substrates with the bending radius equals to 4 mm at a bending speed of 2.5 mm/s. (Figure 4.9 a & b). The resistance of the samples were measured along 1000 bending cycles. From the results, the resistance of the samples almost remained unchanged throughout the test carried out in an ambient condition. Frankly speaking, the stable resistance of Cu@G objects during the bending tests resulted as an outstanding mechanical stability of the metal structures fabricated by this method.

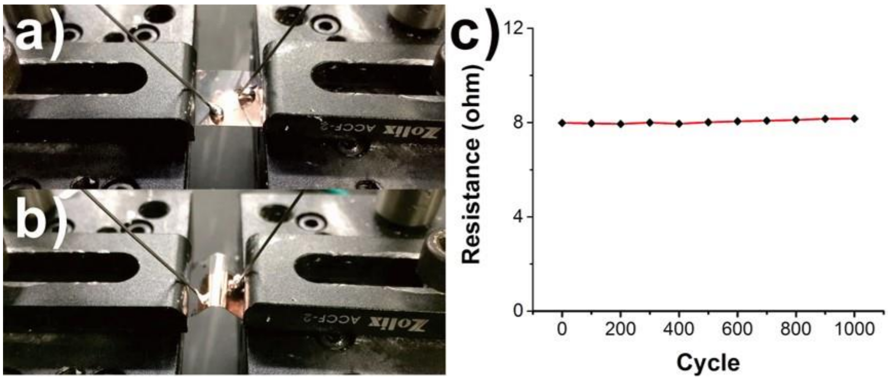

Figure 4.9 Digital images of **a)** ELD-copolymer@CVD graphene sample on PET substrate; **b)** testing system that incorporates a homemade stretch-compress machine. **c)** Graph showing the changes of resistance of the ELD-copolymer@CVD graphene sample along 1000 cycles of bending (bending radius: 4mm and bending speed: 2.5 mm/s)

4.4 Conclusion

In conclusion, via the π-π interaction between graphene film and pyrene groups on the SI-ATRP macro-initiator and copolymer, non-covalent functionalization of graphene with organic layers was achieved successfully.

The as-synthesized anchors allowed asymmetric functionalization of graphene to be carried out in two suitable approaches. Firstly, the growth of polymer brushes via SI-

ATRP with the macro-initiator, which lead to reproducible fabrication of different graphene-based 2D materials with various functional groups, and the degree of polymerization as well as thickness of the functional layers could be controlled by reactions time. Patterning of polymer brushes@CVD graphene on copper foil was also demonstrated by utilizing femtosecond laser. Moreover, a patterned PGMA layer was demonstrated via simple ink-jet printing. As the PGMA brushes are amine-reactive, the patterned PGMA layer could act as bio-microarrays which is potentially to be applied on sensor and diagnostic applications.

On the other hand, spin-coating of the pyrene-group bearing copolymer on top of the graphene was found to be another feasible method for surface decorations. As the functional group of the copolymer could be tailor-made, the coating process is short and it could be carried out under ambient conditions, it should be regarded as a high-throughput surface modifying approach for graphene film.

Also, these polymers-modified graphene objects successfully transferred onto substrates with different natures, ranging from rigid wafer substrate to soft cotton fabric. Thus, transferring of these polymer@graphene films could act as a mild functionalization method on arbitrary substrate materials in ambient environment.

Lastly, the polyelectrolyte bearing graphene 2D objects were known as able to anchor ionic species and was being active to ELD process of metals. The resulting objects fabricated with copolymer were found to possess higher uniformity and exhibit a constant resistance at ~8 Ω even after 1000 cycles of bending on PET substrates; which further supported the graphene based 2D materials as a potential candidate as interconnects in flexible and stretchable devices.

CHAPTER 5 GRAPHENE MEDIATED GROWTH AND TRANSFER OF ULTRATHIN GOLD LAYERS

Gold (Au) is always adopted as electrode material in the flexible electronics research field. However, uniform and well-control deposition of Au layers always include high-temperature physical deposition processes, which limited the choice of target substrates. Here we make use of CVD graphene layer as a deposition platform as well as the release layer that enable wet-transfer of Au thin film. The topography, mechanical stability, conductivity and crystal structure of the CVD graphene supported Au layer were discussed in detail.

5.1 Introduction

Gold is always an important electrode candidate in the flexible electronics research field due to its chemical inertness, availability in pure form, high conductivity and stability up to high pressure and temperatures. However, Au layers are usually fabricated via high-temperature physical deposition process (e.g. sputtering and evaporation), the choice of basal material is limited. Lifting-off and transfer of Au thin film is an approach to solve this problem, however, it is still a challenge nowadays. On the other hand, graphene, the one-atom-thick 2D honeycomb structure formed with carbon atoms, is well-known due to its high mechanical strength, (Young's modulus: ~1 TPa; intrinsic tensile strength: 130 GPa)[21] flexibility, transparency (only ~2.3% absorption of visible light) and electrical conductivity (mobility of charge carriers was found as high as ~ 10 000 cm^{-2} s^{-1} for single-layer graphene at room temperatures.).[1] [3] The chemical vapor deposited (CVD) graphene was also well-known for transferrable onto arbitrary substrates with any polymeric protection on top, which could be adopted for a single-to-few-atom thick conductive layer in flexible and thin-film electronics[55,65,192,193].

While not until 2012, in order to reduce the organic contamination and avoiding any decrease in conductivity of graphene caused by the incomplete removal of polymeric layer, Hsu et al. reported the first CVD graphene transfer assisted by 30 nm Au layer deposited on top[194]. Moreover, the quality of Au-assisted transferred CVD graphene films were proved to be largely improved when compared to the PMMA-assisted transferred ones.[195] The structural completeness as well as the mobility of Au-assisted graphene film was found to be higher and the measured sheet resistance were decreased for ~25 %. While from our point of view, besides these results supported that the few-ten-nanometer thick thermal-deposited or sputtered Au layers were dense enough to protect the CVD graphene film, the metal layer was also successfully transferred onto the target substrates.

Therefore, here we demonstrated that Au layers with different thickness (~10 -100 nm) thermally deposited on CVD graphene film grown on copper (Cu) foil could be transferred onto foreign substrate by simple wet etching and fishing process. In our experiment, we found that graphene acted as a supporting and adhesive layer that enable the wet-transfer of a complete Au film onto arbitrary substrates with far lower roughness when compared to transferred pure Au films. A transferred 20 nm-thick Au film supported by CVD graphene obtained a sheet resistance of 5 Ω sq^{-1}, and showed a satisfactory flexibility with only a 8 % increase in resistance after 5500 bending cycles. Also, with the assistance provided by Prof. Ye Zhu from the Applied Physics Department, we discovered that CVD graphene has acted as a buffer layer for the growth of hexagonal close-packed (hcp)-type Au layer via the TEM images, which is totally different from the ordinary face-centred cubic (fcc)-structure of Au layer fabricated through physical deposition.

In order to establish the reasons behind these extraordinary properties of these graphene-supported Au thin film, we also collaborated with Prof. Bolong Huang from the Department of Applied Biology and Chemical Technology for conducting a series of density functional theory (DFT) calculations, built up the model of Au layer grown on graphene@Cu layer. The appearance of a unique bi-layered structure of the Au layer deposited on graphene grown on Cu foil was discovered. And we believed that these special structures in Au thin film could be explained with the 2D Peierls Distortion. As graphene is a zero-bandgap semiconductor with excellent electron transfer ability, the graphene layer could be considered as the source of p electron, when Au film starts growing on graphene, delocalization of p-electrons occurred and migrated to upper layer Au atoms. Large amount of active p electrons leads to redistribution of electrons and lowered the shielding effect of metals, limited the formation of isolated island during Au growth.

5.2 Experimental section

5.2.1 Deposition of Au on CVD graphene layer

CVD-grown graphene sheets grown on Cu foil were supplied by Apex Graphene Technology CO., LTD. Au layers (10 nm, 20 nm, 50 nm or 100 nm) were deposited on CVD graphene via thermal deposition at a rate of 0.1 nm/s.

5.2.2 Wet transfer of Au@CVD graphene film

The Cu foil beneath CVD graphene layer was etched away with $FeCl_3$ solution for 30 minutes. The Au@CVD graphene film was then rinsed with deionized water, and transferred on the target substrates by a fishing action. The as-transferred Au@CVD graphene film were dried at 65°C-120°C or above depending on the nature substrates.

5.2.3 Characterizations

Optical images were taken by a Nikon Eclipse 80i optical microscope (Nikon, Tokyo, Japan). The SEM images were measured by a CARL ZEISS ULTRA 55 scanning electron microscope. The AFM topographic images were obtained by an XE-100 AFM (Park Systems, Suwon, South Korea) in non-contact mode. The transferred Au layer with and without CVD graphene supported were characterized by X-ray photoelectron spectroscopy (XPS, Kratos AXIS ULTRA HAS, monochromated Al Kα = 1486.6 eV) and X-ray diffraction (XRD, 9KW rotating anode X-Ray source Rigaku SmartLab).

The bending tests were conduct with a home-made bending machine, while the sheet resistance was measured by a 4-point probe system (RTS-9, 4 PROBES TECH).

Transmission electron microscopy (TEM) and high-resolution TEM (HRTEM) images were recorded with JEOL JEM-2100F microscope.

5.3 Results and discussions

5.3.1 Topography and crystallographic studies of the Au@Graphene films

In this part, Au thin films with different thickness ranging from 10 nm to 100 nm were deposited onto pristine Cu foil or CVD graphene grown on Cu foil. Via wet etching of Cu foil and wet transfer process, Au films ≥ 50 nm could be transferred to target substrates with or without CVD graphene support (Figure 5.1 a - d).

While the 10 nm and 20 nm thick Au film could only be transferred with the graphene support. These results suggested that the CVD graphene did provide extra mechanically strength and flexibily for the Au film, enabled the Au films to withstand the surface tension when floating on the solution during the etching and rinsing process. Moreover, the 100% completeness of the 10 - 20 nm Au@CVD graphene (Au@G) films transferred on the porous TEM grid (Figure 5.1 e & f) further demostrated their satisfying ductility, while the pure thin Au films were relatively brittle and broke down into pieces during the wet etching process of Cu foil.

Via the microscopic images and observation, the 20 – 100 nm Au films supported by graphene were transferred with a far higher integrity when compared to the pure Au films. Cracks and buckles were easily observed on the pure Au films, and the thinner was the Au layer, the more serious was the cracking problem of the film. However, there was an oppsite trend observed from the graphene supported Au film. The 20 nm –Au@G was found to be smoother than the 50 nm and 100 nm Au@G samples, and it was the only sample that did not obtain continuous buckles.

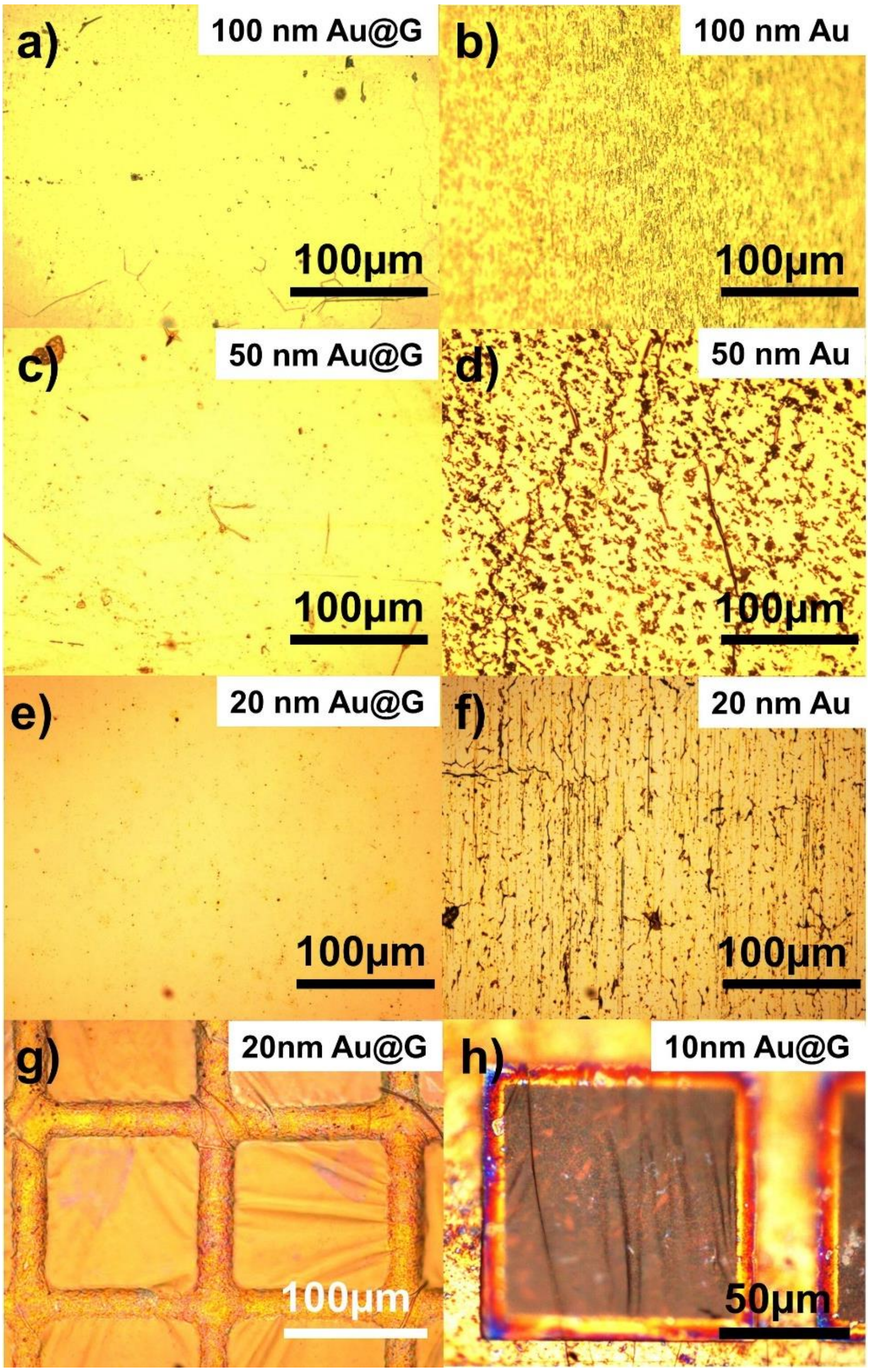

Figure 5.1 Micrscopic images of **a)** 100 nm, **c)** 50 nm and **e)** 20 nm-Au film supported by CVD graphene transferred on Si wafers; pure **b)** 100 nm Au, **d)** 50 nm and **f)** 20 nm-Au film transferred on Si wafers; and **g)** 20 nm and **h)** 10 nm-Au@CVD graphene transferred on Cu TEM grid.

For more detail studies about the morphology, integrity of the films, and any potential defects such as cracks and buckles on the transferred Au films, all the samples were studied under SEM after transferred on Si wafer. Via comparing the SEM images of 50 nm Au films transferred with and without CVD graphene underneath, we could notice that the one supported by graphene was cracks-free (Figure 5.2 a & b), though buckles in length around 2 to 8 μm were observed. While from figure 5.2 c & d, serious and large area defects (~ 10 μm × 20 μm) were spoted all over the wet-transferred 50 nm-pure Au film.

On the other hand, we found out that the 20 nm Au film could not be transferred without the graphene support, which just broken down into very tiny pieces during the wet etching process of Cu foil. While under the SEM observation of 20 nm Au@G transferred on the Si substrate, there were still no cracks or holes were found on the Au layer. Moreover, because of the Au@G film is as thin as < 25 nm, the morphology of the Cu foil which used as the substrate for CVD graphene growth was duplicated by the thermally deposited Au layer, and was observed in figure 5.2 f.

Moreover, not only the Au layer could be protected and transferred with satisfactory conpleteness, the CVD graphene layer was also well-protected by 20 nm Au layer. As shown in the Raman spectroscopy, the quality of graphene was also checked after removal of Cu foil. In this measurement, a PDMS block was attached to the pristine CVD graphene grown on Cu foil, as well as attached on the top of Au layer deposited on CVD graphene layer before the Cu etching process. As there were no obvious difference in the intensity ratio of D and G peaks in between two Raman spectrum, we believed that the graphene film was well-protected by the 20 nm Au, which agreed with the previous researches [195].

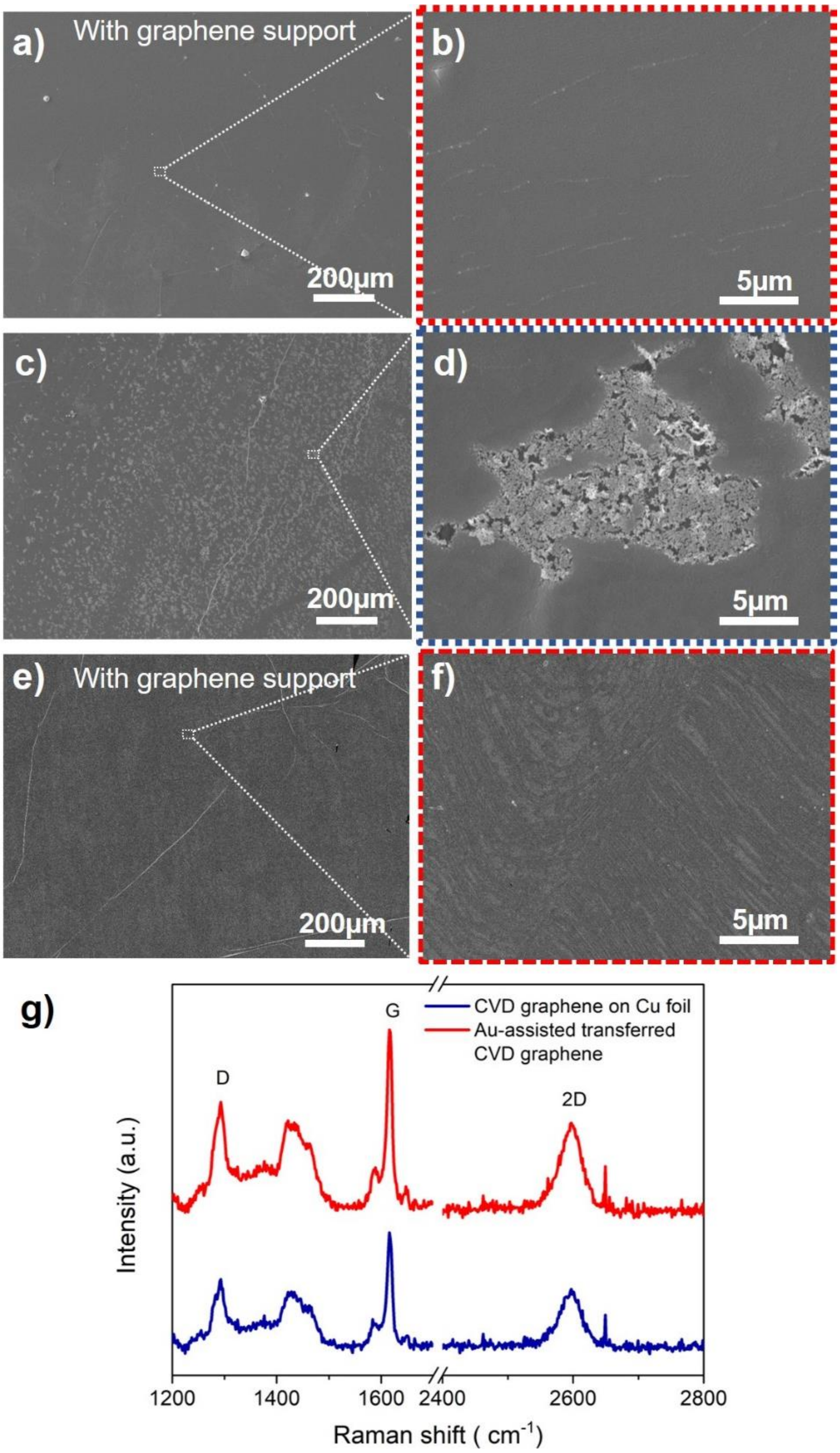

Figure 5.2 SEM images of **a & b)** 50 nm Au@G, **c & d)** pure 50 nm Au layer and **e & f)** 20 nm Au@G transferred onto Si substrates. **g)** Raman spectrum of pristine CVD graphene and 20 nm Au protected CVD graphene.

Also, from the AFM results, the differences of smoothness in between the pure and graphene-supported Au film were well-established. The 50 nm Au@CVD graphene showed a far smoother surface with less buckles (roughness ~13 nm), and the widths of the buckles were resectively small when compared with the pure 50nm Au layer (roughness ~183 nm) (Figure 5.3 a & b).

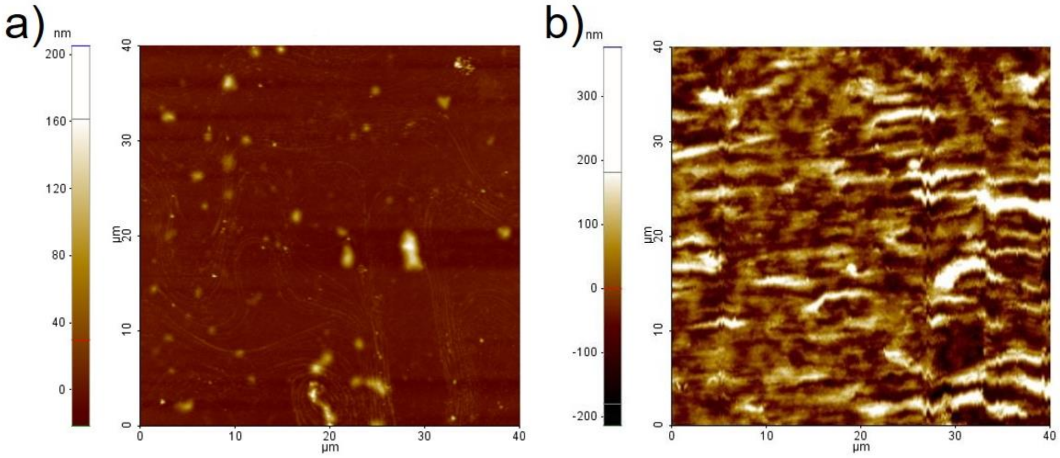

Figure 5.3 AFM images of 50 nm Au layers **a)** with graphene support and **b)** without graphene support which transferred on Si wafer.

While as shown in figure 5.4, we found that the film uniformity of Au layer themally deposited on CVD graphene-grown-Cu foil are actaully far better than that deposited on pure Cu foil. From the TEM images, holes (pointed by red arrows in Figure 5.4 a) and thickness differences could be easily be spoted on the pure 50 nm Au films, where the bulky black areas were the thicker parts, and the brighter and white areas corresponding to the holes which allowed the light to pass through. For the 20 nm Au@CVD graphene film, the Au grains are found to be nicely packed, showing a Au layer with higher crystallinity and uniform thickness.

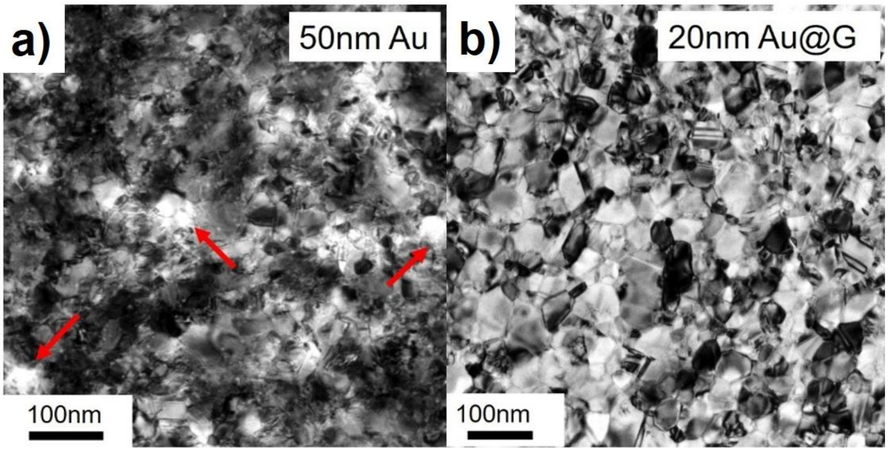

Figure 5.4. TEM images of **a)** 50nm Au and **b)** graphene supported 20nm Au layer transferred onto Cu TEM grids.

We also studied the orientation of Au crystals from the very thin (~10nm) Au@CVD graphene film. Figure 5.5 a and b showed a non-continuous Au film with a common morphology that had been reported for evaporated ultrathin Au films. Surprisingly, as shown in the HRTEM image (Figure 5.5 c) taken along the [100] zone axis, hcp nanostructure of Au was discovered. To further study the crystal nanostructure, selected area electron diffraction (SAED) data was obtained, and a typical hcp 002 ring was found, the measured lattice spacing of Au atoms under HRTEM was found to be 2.41Å along the $[002]_h$ zone axis, and 2.27Å along the $[011]_h$ zone axis. And to our best knowledge, this is the first that hcp-Au was discovered on CVD graphene via simple thermal deposition process.

To futher study the orienetation of Au particles, XRD was conducted on Au@G samples with diferent thickness. From the XRD spectra in Figure 5.6, a gradually increasing trend of Au (200) peak with increasing Au thickness could be observed for the graphene supported Au films. When the Au layer was only 10nm, there were no Au (200) peak could be observed, the XRD pattern of 10nm-Au@graphene shows a pure and strong [111] out-of-plane orientation. When the number of Au layers increased, the spectra became more complicated with observable peaks.

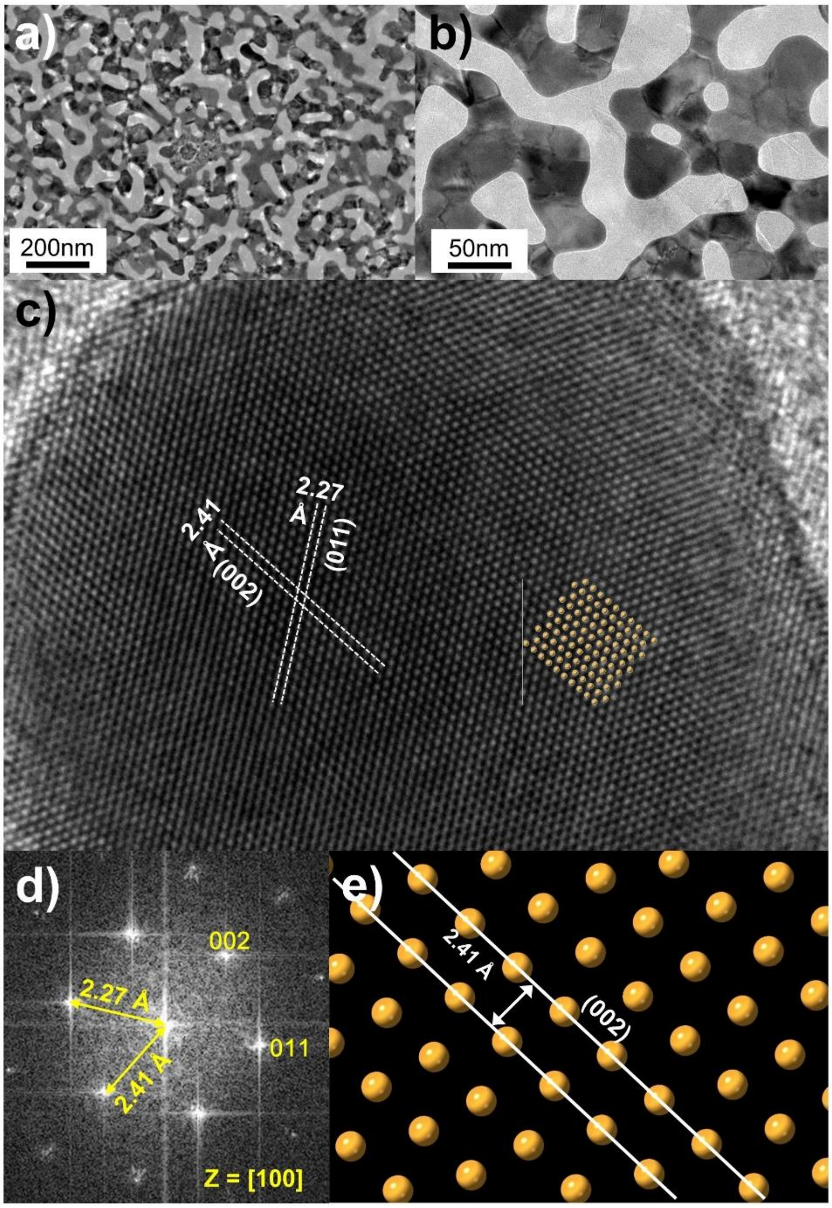

Figure 5.5 TEM analysis of Au@CVD graphene film. **a & b)** TEM images of ~10nm thick Au@CVD graphene film. **c)** HRTEM image of a small region of the Au@CVD graphene film along [100] zone axis, as indicated in the SAED in **d)**. **d)** SAED pattern of the Au, showing diffraction rings for the Au layer along [100] zone axis. **e)** Model of the atomic arrangement of hcp structure corresponding to **c)**.

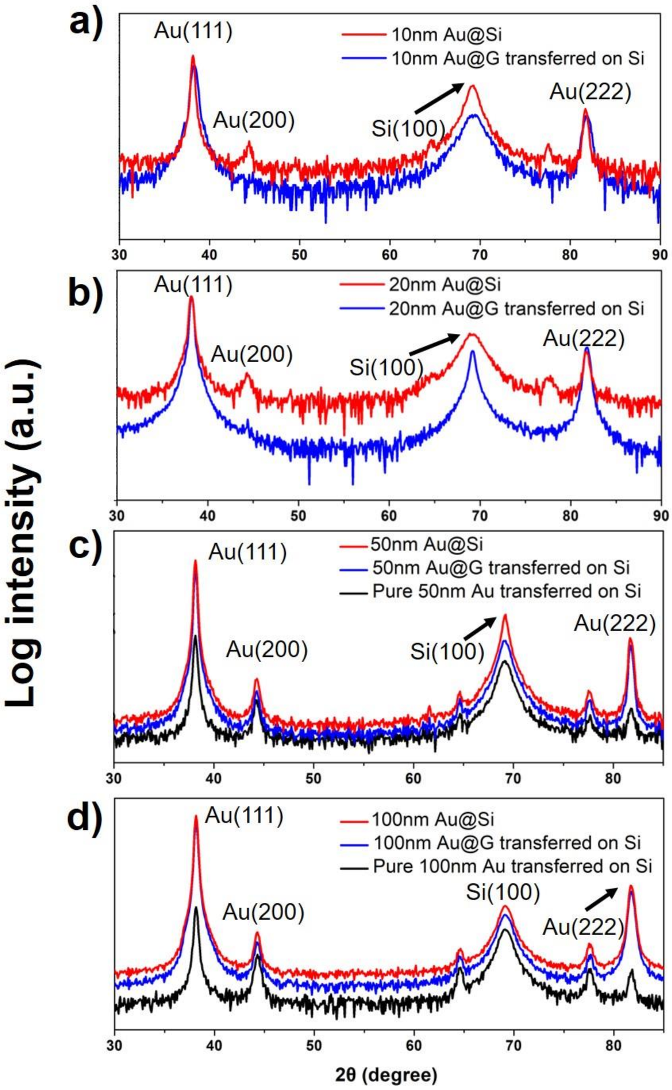

Figure 5.6 XRD patterns of **a)** 10 nm, **b)** 20 nm, **c)** 50 nm, and **d)**100nm Au layers directly deposited on Si substrates, wet-transferred on Si wafer with and without CVD graphene support.

5.3.2 Mechanical study of Au@Graphene films

On the order hand, as graphene film is well-known for its flexibilty and conductive nature, instead of the integraty of the trasnferred Au films, we investigated if the CVD graphene film can also enhance the mechanical stability of the deposited Au layer. Bending test was therefore conducted to elaborating the differences in between Au film with and without graphene support in terms of conductivity and flexibility.

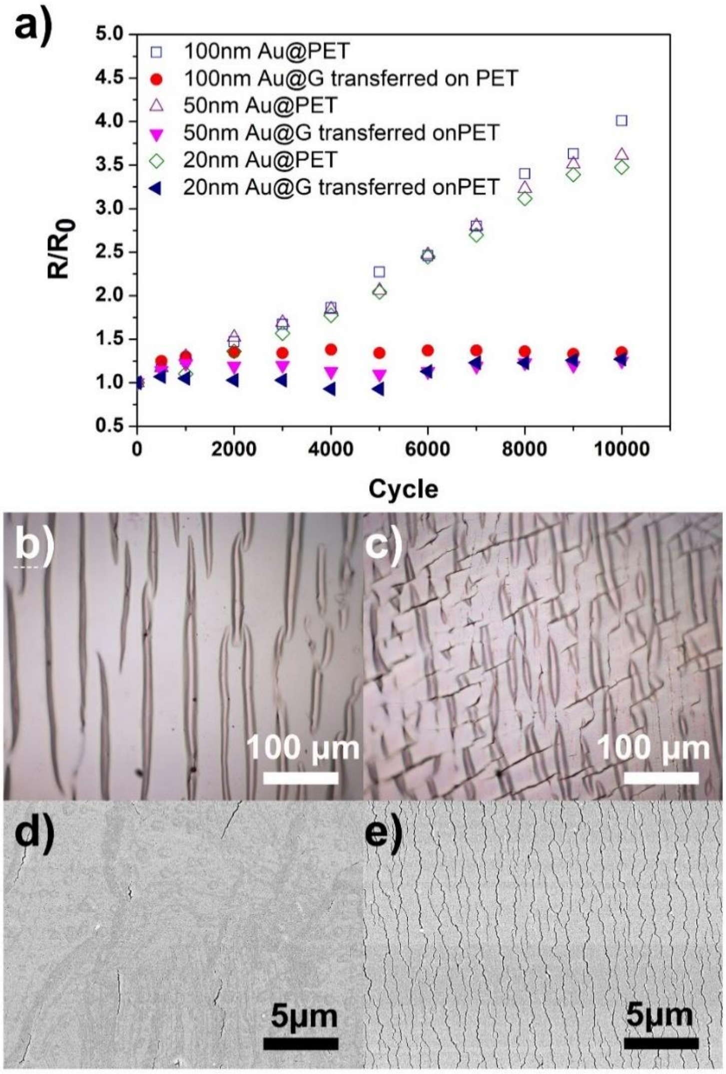

Figure 5.7 a) Sheet resistance changes of Au films (with and without CVD graphene support) transferred on 125 µm PET substrates within 10000 bending cycles with a bending radius of 2.5 mm. Microscopic images of 100 nm Au film **b)** with and **c)**without graphene support captured after 10000 bending cycles. SEM images of 20 nm Au films **d)** with and **e)** without graphene support taken after 10000 bending cycles. All the bending cycles consisted with a bending radius of 2.5 mm.

The original sheet resistance of 10 nm-, 20 nm- , 50 nm- and 100 nm- Au@G film transferred on PET substartes were measured as the followings: 11.01 Ω/sq, 4.98 Ω/sq, 1.13 Ω/sq and 0.8 Ω/sq respectively. During the bending test, the sheet resistances of all graphene supported Au films was decreasing until the 5000 cycles (Figure 5.7 a). With the aid of microscopic and SEM images (Figure 5.7 b – e), we believed that the Au films were successfully buckled up in a direction normal to the bending action, instead of breaking during the bending process, which was caused by the lubricating nature of graphene as reported in the literature[196,197]. After 10000 bending cycles, sheet resistance of the 20, 50, 100 nm-thick Au supported by CVD graphene only increased by ~25%, while the pure Au films obtained a far larger increase of sheet resistance about 350%. And this set of data definitly demostrated the enhanced flexibilty of the Au films when supported by CVD graphene films, as well as showing that the Au@G films would be a more preferrable canadidate as a conductive component in the flexible elemctronics.

5.3.3 Stimulation and crystal structure of Au deposited on CVD graphene

Since the extra ordinary mechanical strength and ductility of the Au films deposited on CVD graphene was measured, and rare hcp Au layer deposited via thermal deposition was discovered as mentioned above, DFT calculations were carried out to probe the models of the Au layers thermally grown on CVD graphene@Cu foil to seek for the mechanism behind these phenomena. The Au growth models are based on one layer of graphene and four layers of Cu (111) in bottom. Growth of Au is directly on graphene with Au (111) surfaces from 1 layer to 10 layers as shown in Figure 5.8. As the number of layers grow, we have found out that the ordered Au structure disappeared, accompanying with the appearance of a unique bi-layered structure especially in even layers of Au. This bi-layered structure showed a regular fluctuation rather than planar structure as multi-layered graphite.

As the layered increases, the fluctuation on each layer are becoming more aligned with the nearest layer that form the bi-layered structure. As the tendency of forming bi-layered structure, the distance of each bi-layered structure is larger than the internal distance in bi-layer. The distance results and other parameters are listed in Table 2. For odd layers of Au, the bottom layer of graphene will be apparently lifted to form bi-layer structure with the bottom single Au layer. Such phenomenon did not appear in even layer growth of Au until layer 10. The interactions between each bi-layer structure in odd layered films are stronger and more obvious, which even cause upward migration of Au atoms in Layer 7 and Layer 9. Therefore, the bi-layered structure becomes more obvious and ordered in the even number layer structures than the odd number layers.

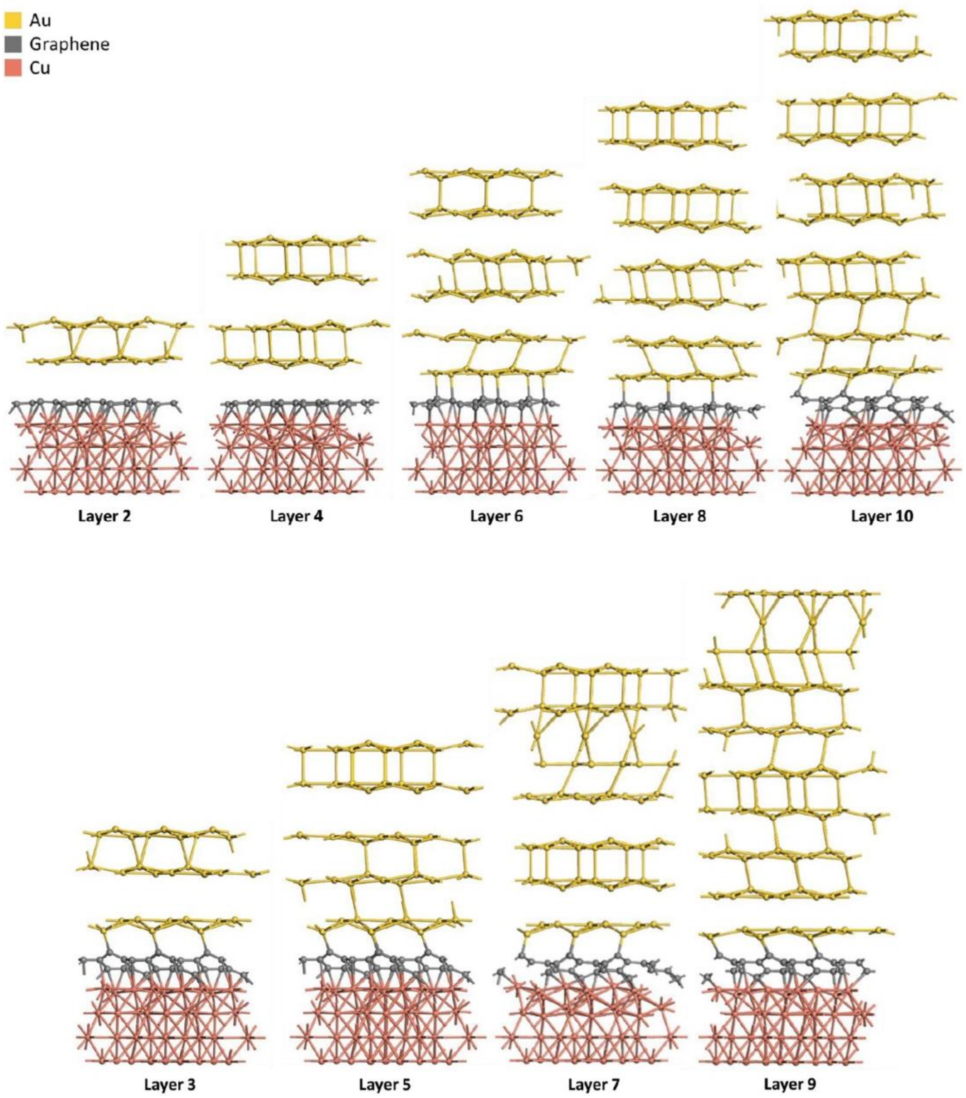

Figure 5.8 Local view of even layers and odd layers of Cu-Graphene-Au multilayer structures.

Layer number	Formation energy (eV)	Bi-layer distance (Å)
1	0.28	/
2	0.33	2.659
3	-1.83	2.597
4	0.01	2.925, 2.968
5	-2.93	2.770,2.930
6	1.00	2.713, 2.851, 2.782
7	-2.12	2.878, 2.946
8	1.16	2.610, 2.842, 2.880, 2.921
9	-1.17	2.634, 2.967, 2.793
10	-1.26	2.808, 2.962, 2.856, 2.931, 2.949

Table 2. The formation energy and layer parameters of different Au thin films

The formation energy has been calculated and are shown in Figure 5.9 a. The even layers show higher formation energies than the odd layers, which might originate from the more ordered and separated bi-layered structure shows slightly less bonding between layers. The higher energy cost might be needed to achieve more stable Peierls Distortion on each bi-layer. When over 3 layers, we can see the distortion angle on each layer are coherent around 12.5~15°. The bi-layer internal distance shows smaller ranges in even layers than odd layers due to new sandwich layer or bond formation especially in Layer 7 and Layer 9. The more complicated electrons distribution in odd layers might disturb the layer stability that lead to more interaction between bi-layer and further influence the distances between bi-layers. Overall, the internal bi-layer distance has a trend of increasing as the layers increase.

To further figure out the difference of influence by the layer numbers, we have compared the partial density of states (PDOS) of Au atoms d-orbitals for odd number layers and even number layers that is shown in Figure 5.9 b. From the pattern shape, we can see that in even number layers, the PDOS of Au atoms shows one relatively higher peak around -6 eV with three smaller and broaden peaks around -4.5 eV, which gradually shifts 0.5 eV downwards as the layer number grows.

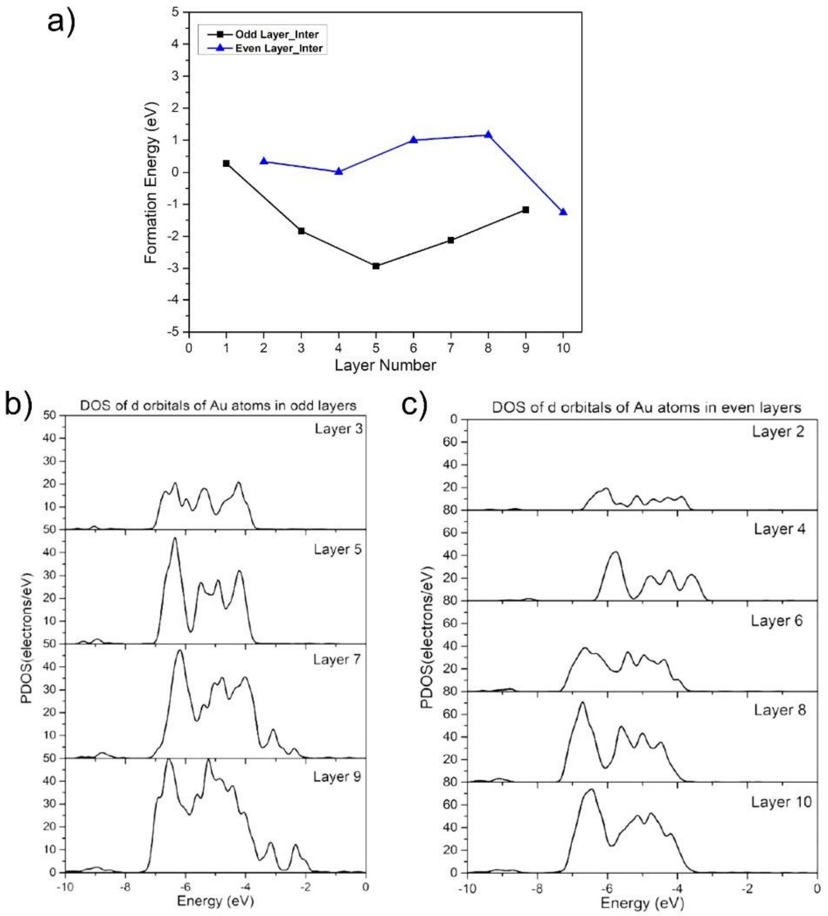

Figure 5.9 a) Formation energies of different number of layers. **b)** Comparison PDOS of Au atoms in odd layers and even layers structured films.

For odd numbers, the peaks remain basically at the same position. Moreover, comparing to the clear peaks separation in even number layers, odd number layers shows more closer peaks with relatively smaller intensity, representing a more complicated and decentralized distribution of electrons among the layers. This can also support the structure difference between odd number layers and even number layers. In Figure 5.10 and Figure 5.11, all the PDOS of Au atoms in every layer are displayed from 6 layered structure and 5 layered structure, respectively.

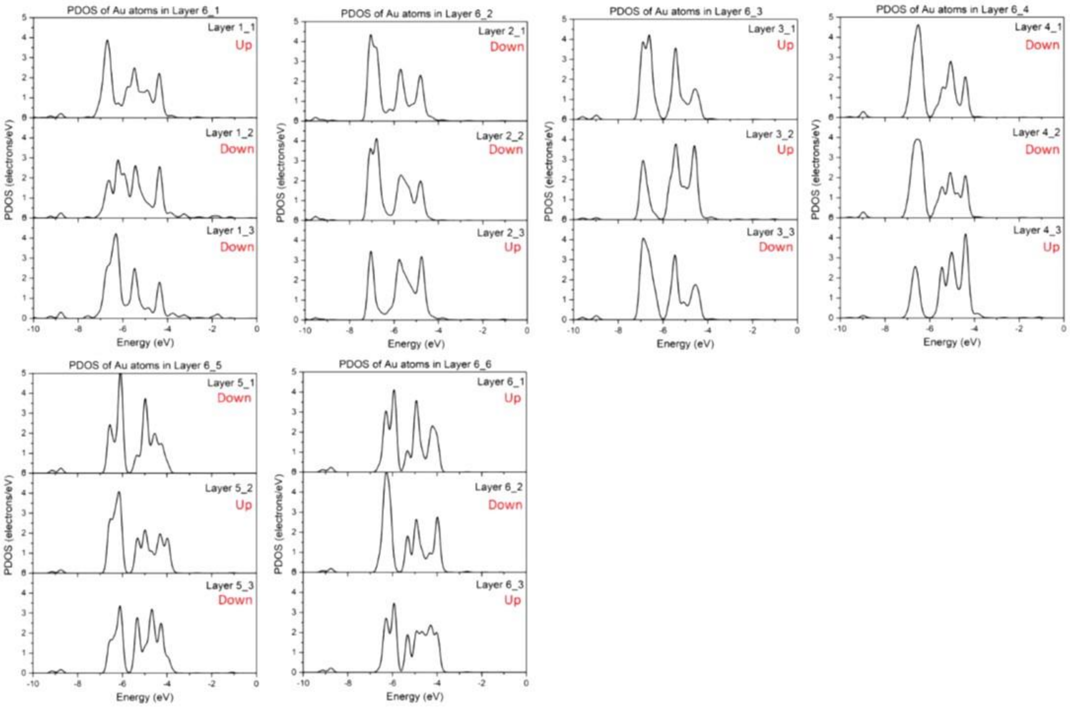

Figure 5.10 PDOS of all Au atoms on Layer 6.

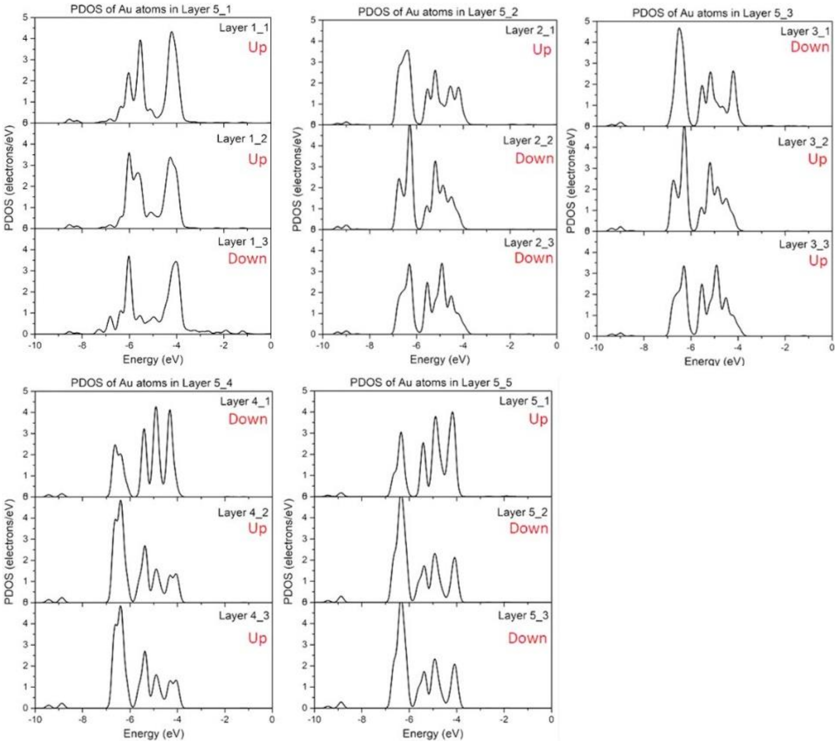

Figure 5.11 PDOS of all Au atoms on Layer 5.

It is quite obvious that Au atoms of the bottom layer shows relatively distinct pattern with other layers, which reflects the influence from p electrons causing by strong interaction with the bottom graphene.

Based on the preliminary results, we speculate that the special bi-layered structures in this Au thin films should consist the 2D Peierls Distortion. To achieve higher stability, the low dimension materials will result in Peierls Distortion, which can cause the neighboring atoms alternately to get buckled such as the fluctuated structures. On a 2D surface, the buckling phenomenon happens both in and out of the surface plane that further change the charge density wave, which is in good agreement with the Au thin films. The bottom graphene layer can be considered as a sources of p electrons, which is like a zero-bandgap semiconductor with excellent electron transfer ability. The schematic diagram of graphene electronic structure can be seen in Figure 5.12.

When Au film starts growing on graphene, the bonding originates from strong interaction will cause delocalization of p-electrons and migration to upper layer Au atoms. The large amount of active p electrons will affect the electrons density of each layer that result in the redistribution of electrons and lower the shielding effect of metals to relieve the isolated island structure during thin film growth. This is also consistent with the PDOS results that lower layers showing more complicated peaks. Since the migration distances of p-electrons are limited, the higher layers show less effect from electrons redistribution and show very clear peaks in PDOS. And this also agreed with the gradual changes of XRD spectrum of the Au layers along the increase in Au film thickness.

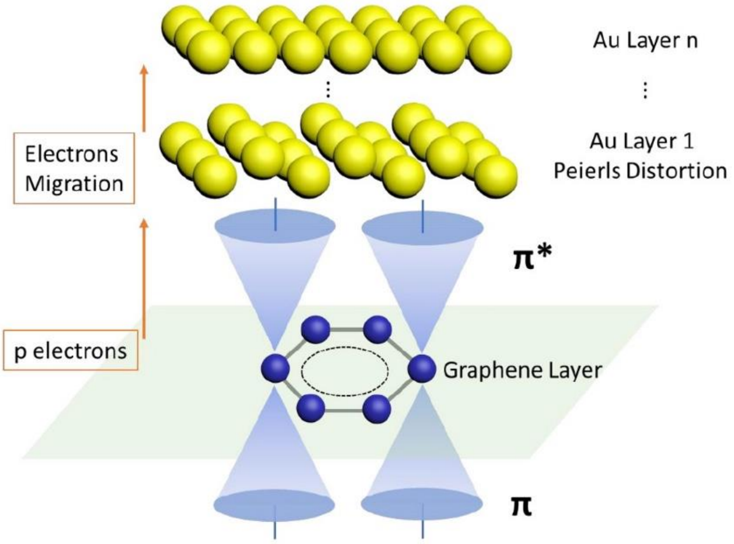

Figure 5.12 Schematic diagram of Au atoms growth on graphene.

To find out whether orbital couplings were happening in between the Au layers and graphene films as predicted by the stimulation above, Au layers (2 nm) deposited on graphene-grown Cu foil and bare Cu foil were characterized by X-ray photoelectron spectroscopy (XPS). Figure 5.13a represents the C 1s of graphene layer of the 2 nm Au@G@Cu foil sample, the sp^2 hybridized C atoms binding energy (283.4 eV) dominated the peak, showing the adopted CVD graphene was uniformly deposited on Cu foil. As shown in figure 5.13 b - d, the observed Au 4d $_{5/2}$, Au 4d $_{3/2}$, Au $4f_{7/2}$ and Au $4f_{5/2}$ binding energy of Au layer supported by CVD graphene was shifted to a lower value by 0.13 eV, 0.25 eV, 0.2 eV and 0.1 eV respectively, when compared with the pure Au layer deposited on Cu foil, which is a typical shift attributed to the strong metal-semiconductor interaction[198, 199]. In this experiment, the negative binding energy shift of the Au d and f orbitals, could be explained by a relatively negatively charged Au layer resulted from the electrons transferred from the graphene layer. And these observations agreed with the stimulation results about the p-electron donating behavior of semiconducting graphene towards Au layer.

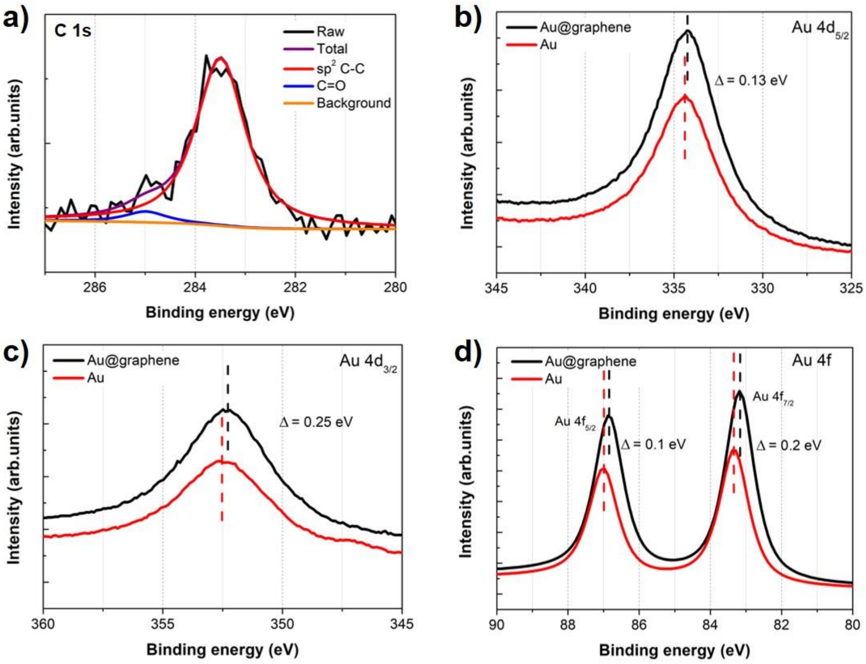

Figure 5.13 XPS analysis of **a)** C 1s of Au@G film, **b)** Au 4d 5/2, **c)** Au 4d 3/2 and **d)** Au 4f of Au layer supported by graphene (black line) and pure Au layer (red line) on Cu foils.

5.4 Conclusion

In this chapter, we successfully transfer 10 to 100 nm Au thin film supported by CVD graphene onto different substrates such as Si wafer, polymeric substrates and porous TEM grids. By adopting this approach, homogenous metal films could be transferred on arbitrary materials in ambient environment, without the concern of high temperature which always involved in the thermal deposition process of metal layers.

According to the experimental results, all of the Au@G films attached on their substrates with satisfactory integrity and smoothness, which cannot be achieved by the pure Au films grown on pure Cu foil even they had the same thicknesses. Moreover, the mechanical stability and flexibility of the Au@G films were found to be significantly higher than pure Au films, where the sheet resistance of an ultrathin 20 nm Au@G film only increase for ~25% after 10000 bending cycles, which makes the Au@G films potentially applicable in highly flexible electronic devices.

Importantly, here we discovered the hcp Au layer structure which deposited on the CVD graphene surface directly for the first time. Our results also indicated that, due to the excellent electron transfer ability and p-electron donating nature of graphene, the electrons density of each Au layers deposited on top of graphene were affected. In consequence, the formation of isolated island structure during the Au deposition was minimized, and lead to the unexpected epitaxial growth of denser and smoother Au film than on bare Cu foil.

CHAPTER 6 GRAPHENE-BASED FLEXIBLE AND TRANSPARENT ELECTRODES

In the previous chapter, we discovered that thin Au film could be wet-transferred onto different substrates without any top-coated protection when supported by graphene film. Here, we fabricated the flexible, transparent and transferable CVD graphene based electrode via metal patterning and wet-transfer approaches. And the application of the electrode on photovoltaic devices would also be demonstrated.

6.1 Introduction

Transparent electrode is the essential components in the optoelectronic devices, such as solar cells, touch screen, light-emitting diodes (LEDs) and other display devices. An ideal transparent electrode should possess a high optical transmittance (%T) and low electrical sheet resistance (R_s). Moreover, as being flexible and wearable is the trend of the advanced electronics development, flexibility of the electrodes has become another important factor needed to take into account. Therefore, a great challenge did appear to the commonly used transparent electrode, such as indium tin oxide (ITO), which is well known for its high optical transmittance (> 85 %T in visible light region) and highly conductive (<15 Ω / sq), but brittle in nature[19,20,200].

In order to meet the market demand of flexible devices, a number of researches on flexible transparent electrodes have been conducted, and the materials being studied include the conductive polymer, carbon-based materials and thin metal films or meshes. However, each of these materials possesses their own drawbacks as conductive electrodes. For example, the electrical conductivity of conductive polymer and carbon-based materials are relatively low when compared to the others. Metal meshes and thin films did show excellent performance in terms of flexibility, optical transparency and electrical conductivity in previous researches. While as same as ITO, the fabrication process of uniform metal film always involves high-temperature vacuum deposition process, which limited the choice of the substrates when they were deposited as bottom electrodes. Also, due to the concern of contamination and surface roughness of uncompleted devices, direct patterning of micro-scale metal mesh on the top of the device structure is inapplicable. Moreover, researchers had investigated on fabricating flexible transparent electrodes with metal nanowires[201-203] and metal nanoparticles[204]. Silver nanowire (AgNW) is the most promising candidate among the metal NWs due to their high conductivity, and as they could be dispersed well in solution, a thin, transparent layer of AgNWs could be achieved by spin-coating. However, spin-coating approach is not applicable when a large-area transparent conductive layer was needed. On the other hand, metal nanoparticles were always prepared as ink or pasted and be coated by printing method, e.g. screen printing. However, as the viscosity of the inks were relatively high, a uniform conductive surface with low roughness is hard to be achieved via this approach, and electrode with such a high roughness is not suitable for acting as a bottom electrode, especially for photovoltaic devices.

As there are still obstacles on applying pure metal or metal particle inks as flexible transparent electrodes, there were researches focused on developing such electrodes by combining both of the conductive polymer and the metal mesh. For example, in 2011, a transparent electrode fabricated with silver (Ag) current collecting grids screen printed on top of highly conductive PEDOT: PSS was demonstrated by Galagan et al.[18].The Ag grids was deposited with 6.4–8% surface coverage of the PEDOT: PSS layer, and a low sheet resistance of 1 Ω/sq was achieved. However, it was found to be buckled more seriously when their substrate got thinner than 130 μm, that the thickness of substrates was largely limited if a high flexibility was required for device application. Therefore, no matter the fabricating electrode which possesses high transparency, conductivity and flexibility at the same time, or depositing such electrode without harsh environment such as vacuum and high temperature, are the major challenges for researchers until now.

On the other hand, for the carbon based conductive materials, CVD graphene was reported to be highly flexible and transparent, and available for large area production due to the advanced CVD process, thus it has been applied as top and bottom electrodes via wet or dry transfer processes in the literature[67,68,205-207]. But the relative low conductivity of graphene when compared to ITO is still an obstacle in nature which needed to be overcome, and we believed that, the combination of graphene with highly conductive metal could be a solution.

Therefore, here we demonstrated the fabrication of a transferable, flexible and transparent electrode by combining the metal mesh with the mono-to-few CVD graphene films. Via photolithography and simple rinsing processes, patterned 100 nm-thick Au meshes were fabricated on CVD graphene grown on Cu foil. Via the etching of Cu, the whole Au@CVD graphene (Au@G) mesh becomes free-standing electrode, and were transferred on target substrates and devices. This Au@G mesh proceed a high transmittance of light in visible region (~92 %T) and less than 10 % increase in sheet resistance after 1000 bending cycles. As a demonstration of the transparent electrode which fabricated and transferred with this new approach, an organic solar cell was fabricated by adopting the Au@G mesh as top electrode.

6.2 Experimental section

6.2.1 Fabrication and transfer of Au@G mesh

CVD-grown graphene sheets grown on Cu foil were supplied by Apex Graphene Technology CO., LTD. Target pattern for metal mesh was first fabricated on the surface of CVD graphene via photolithography by using the negative resist (NR9-1500PY), where the area for resulted metal mesh lines were left as bare graphene. 100 nm Au layer was then deposited on top via evaporation process (0.1 nm s^{-1}).

Photoresist with the Au on top were then removed by rinsing the whole Cu foil supported sample with acetone.

The basal Cu foil was etched away afterwards by placing on a diluted $FeCl_3$ solution (50 mg/ml in deionized water) for 1.5 hours. In order to remove the Cu etchant residue, Au@G electrode was then transferred on the surface of deionized water, and ready to be fished on the target substrates.

6.2.2 Fabrication of organic solar cell

The fabrication of the semi-transparent organic solar cell began with modifying the cleaned ITO electrodes with a thin layer of PEI. To deposite a 15 nm thick PEI layer, a solution of PEI (0.5 wt% in 2-methoxylethanol) was spin-coated on the ITO substrate at 5000 rpm for 30 s. After annealing at 100 ºC for 10 min, via spin-coating a chlorobenzene solution of P3HT (20 mg/mL) and PC61BM (16 mg/mL) at 800 rpm for 30 s on top of PEI layer, a 400 nm-thick P3HT:PCBM active layer was coated.

The film was then annealed at 145 ºC for 5 minutes in a N_2-filled glove box. Afrerwards, ~170 nm thick poly(3,4-ethylenedioxythiophene) polystyrene sulfonate (PEDOT:PSS) film was coated on top of the active layer by spin-coating PH 1000 (~1 wt% PEDOT:PSS in water, doped with 5% DMSO and 1% Znoyl FS-300 surfactant) solution at 1000 round/minute for 60 seconds in air, then the substrate was transferred into glove box and annealed at 130 ºC for 10 minutes.

Finally, graphene@Au was transfer-printed on top of the PEDOT:PSS electrodes by wet-transfer. In order to avoid mechanical damage to the electrodes as well as minimize the contact resistance, silver paste was casted on the edge of the Au mesh which contact the probes during the solar cell preformance measurements.

6.2.3 Calculation for photovolatic device

The *I-V* curve of solar cells reflect the photovoltaic performance of solar cells under the irradiation of light, or the diode characteristics of solar cells under dark state. A solar simulator equipped with airmass 1.5 (AM 1.5) filter is commonly used as the standard light source for solar cell characterization, and the areal power rate of the simulated sunlight is 100 mW/cm^2. The solar cells are connected to a sourcemeter to measure the *I-V* curves. The sourcemeter applies a swept bias either from negative to positive or a reversed scan on the solar cells, and the current that passes through the solar cells is recorded.

The value of open-circuit voltage (V_{OC}) and short-circuit current (I_{SC}) of the solar cell was be obtained from I-V characterization. The current is 0 when the applied bias is equal to V_{OC}, and the photocurrent at 0 bias (i.e. at short circuit) is the I_{SC}. The short-circuit current density (J_{SC}) of the solar cells can be calculated by dividing the I_{SC} with the active area of the solar cells.

The PCE of a solar cell is:

$$PCE = \frac{P_{max}}{P_{solar}} = \frac{P_{max}}{100mW/cm^2 \times A} \tag{4}$$

where P_{max} is the maximum power output of the solar cell, P_{solar} is the power of the sunlight on device which is 100 mW/cm^2 times the active area (A) of the solar cell.

The fill factor (FF) of the solar cell is defined as:

$$FF = \frac{P_{max}}{V_{OC} \times I_{SC}} = \frac{PCE \times 100mW/cm^2 \times A}{V_{OC} \times I_{SC}} = \frac{PCE \times 100mW/cm^2}{V_{OC} \times J_{SC}} \tag{5}$$

where J_{SC} stands for short circuit current density.

6.3 Results and discussions

6.3.1 Fabrication and characterizations of metal mesh on CVD graphene

According to previous chapter, we found that Au layer could protect the graphene film for wet transfer. Due to the excellent adhesion of Au on CVD graphene, we fabricated a transferable patterned Au layer supported by the mono-to-few layer graphene.

As shown in figure 6.1, micron-scale Au mesh structure were firstly prepared on CVD graphene grown on Cu foil with negative photoresist. The photoresist was first coat and developed on the square space of the mesh, while leaving the Au mesh line area as bare graphene surface. After the thermal deposition of Au, the Au deposited on top of the photoresist was rinsed away by acetone, while the Au directly deposited on CVD graphene was found to be attached firmly on the surface. After the etching of Cu foil with $FeCl_3$, adopting deionized water as the media, the Au@G meshes were wet-transferred onto target substrates.

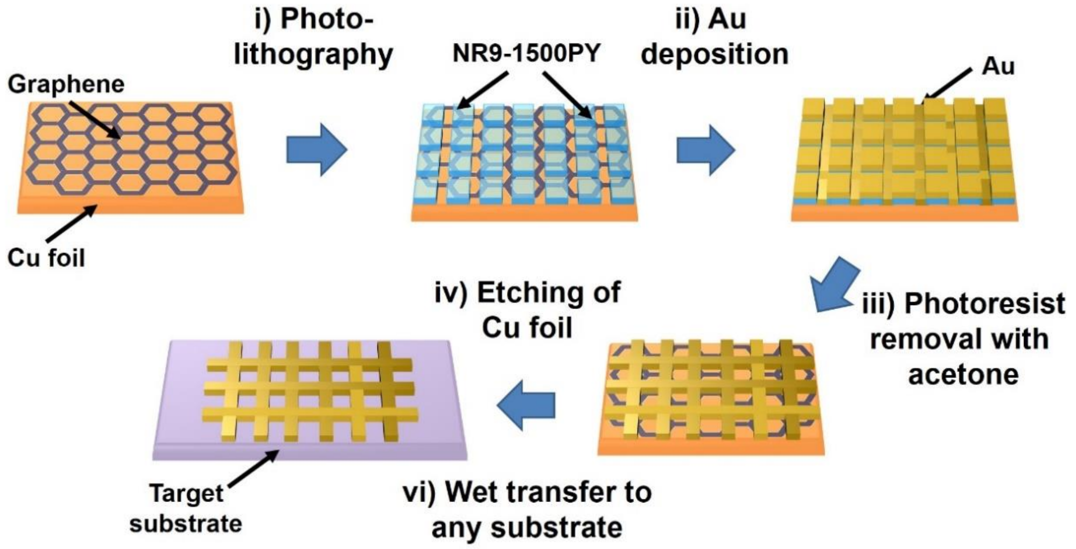

Figure 6.1 Schematic diagram of the fabrication and transfer process of Au@G mesh.

We believed that the conductivity and flexibility of Au@G mesh fabricated via this approach could be easily tunes via controlling the mesh pattern. By pre-designing the photomasks, two Au meshes with different square holes area were achieved on graphene surface. Both of them obtain lines with 5 µm width, but one of them obtained square holes of 50 x 50 μm^2 while the other obtained 100 x 100 μm^2 ones. As shown in figure. 6.2 a – d, the Au@G meshes were not damaged by the etching and transfer processes. However, as shown in figure 6.2 e, we could notice that the line width of transferred Au@G mesh was not exactly 5 µm as designed for the photomask, but 5.9 µm as measured via AFM. Here the wider line width was mainly caused by the roughness of the Cu foil which was used as the growth of graphene. As the Cu foil was not exactly flat, the photomask could not be perfectly attached on the graphene surface, thus the photoresist solidified on the graphene surface could not be perfectly duplicated the pattern of photomask. In order to solve this line widening or narrowing problem, the length of UV curing time during the photolithography process would be the key parameter.

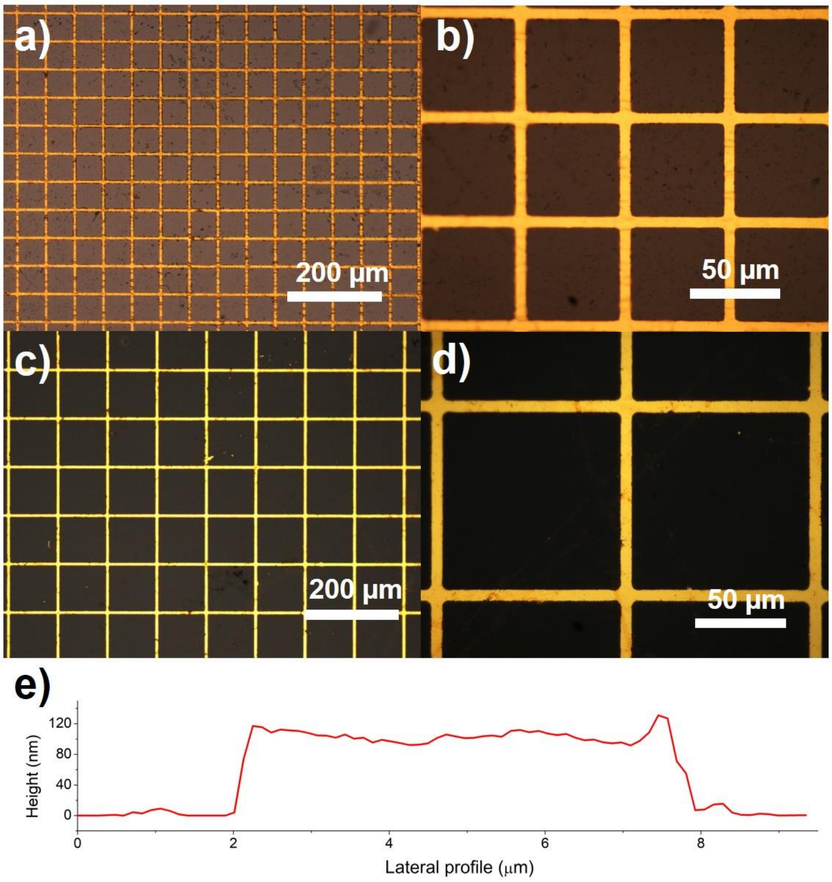

Figure 6.2 Microscopic images of transferred Au@G mesh on 125µm PET film with patterns involved **a & b)** 100 x 100 µm^2 and **c & d)** 50 x 50 µm^2 square holes. **e)** Cross-sectional profile of the Au@G mesh.

In addition, we found that the size of the square holes was significantly affecting the optical transparency of the meshes. The transparency of the electrode with 100 x 100 µm^2 space achieved a high optical transparency of light, ~92 %T at the visible region (at wavelength = 550 nm), while the one with smaller space area only obtained ~80 %T (figure 6.3 a), i.e. the double size of the holes lead to a %T decrease of ~12%.

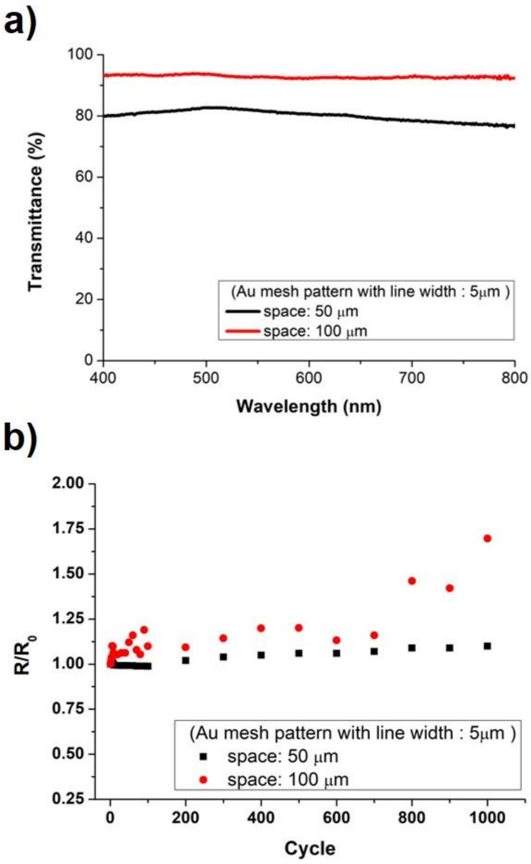

Figure 6.3 a) Graph showing transmittance of light and **b)** bending performance of the Au@G mesh transferred on 125µm PET film.

Moreover, in order to investigate whether it is a suitable candidate as transparent electrode in practical devices, the flexibility of Au@G mesh had been evaluated by bending test after transferred onto a PET substrate, and the bending radius was set as 4 mm. The original sheet resistance of the Au@G mesh with 50 x 50 µm^2 square holes was measured as 19.8 **Ω**; while Au@G mesh with 100 x 100 µm^2 square holes obtained an original 43 **Ω** sheet resistance. As plotter in figure 6.3 b, after 1000 bending cycles, the sheet resistance of Au@G mesh with smaller holes only increase ~10%, while the resistance of the mesh with larger holes increased for 70%. An indirect relationship was therefore observed in between the transmittance and flexibly for these semi-transparent electrodes.

6.3.2 Application of Au@G mesh as top electrode of organic solar cell

In order to demonstrate the practical usage of the Au@G semi-transparent electrode, an organic solar cell was further fabricated with adopting the Au@G mesh as the wet-transferred top electrode.

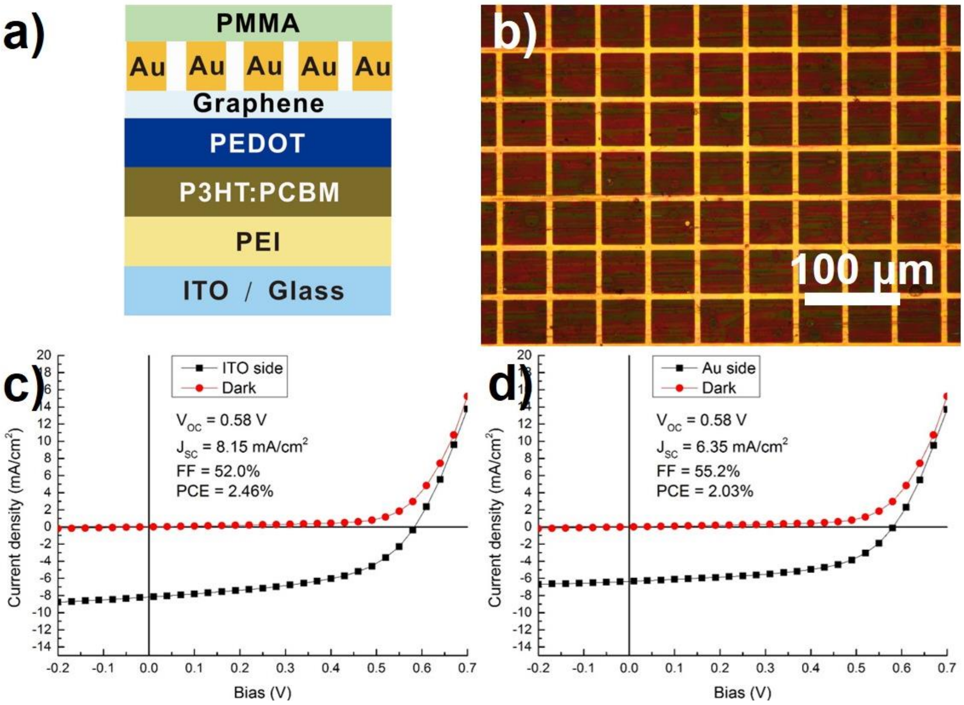

Figure 6.4 a) Schematic diagram showing the structure of the solar cell. **b)** Microscopic images of the Au@G mesh as top electrode on the solar cell. Graphs showing the J-V characteristics of the solar cell when tested from **c)** ITO side and **d)** Au mesh side.

As the Au@G mesh was confirmed to be transferable without protection, and processing a transparency >80 %T, it was believed to be an ideal top electrode of organic solar cell (Figure 6.4 a) which could be deposited on top in ambient environment. From the microscopic images capturing the top view of the as-fabricated solar cell, the Au mesh was found to be completely transferred without damages, and attached smoothly on the solar cell (Figure 6.4 b).

As the bottom electrode of the fabricated solar cell is ITO/glass, which acquired high transparency >85 %T in visible light region, the whole device was semi-transparent.

The performance of the solar cell was measured as the followings, V_{OC} is 0.58 V while the J_{SC} could reach 8.15 mA/cm^2, and the corresponding field factor (FF) and power conversion efficiency (PCE) was calculated as 2.46% when the device was tested from the ITO side (Figure 6.4 c). Moreover, as shown in figure 6.4 d, the FF can reach 55.2% while the solar cell was tested from the Au mesh side. The photovoltaic performance of solar cell was also checked in the dark state and the no serious current leakage problem was observed.

6.3 Conclusion

In summary, we developed the fabrication of transferable, flexible and semi-transparent Au@G electrode through photolithography on CVD graphene, followed by thermal deposition of Au. The patterned of Au layers were then simply achieved by removing the photoresist with acetone. With this fabricating approach, the electrode thickness and mesh pattern could be varied and controlled by photomask design. Moreover, a satisfactory mechanical stability was achieved by the Au@G mesh, where the sheet resistance only increased for 10% after 1000 bending cycles for the Au@G mesh with 50μm ×50μm space in between lines. Other than the promising flexibility the resulted Au@G mesh electrode achieved a high optical transparency ~92 %T.

Furthermore, as a demonstration of applying the Au@G mesh on electronics which require high conductivity and transparency, an organic solar cell was fabricated with the semitransparent electrode adopted as the top electrode. In this case, the final step of the photovoltaic device could be done in an ambient condition, which would be satisfactory for those devices made with components that would deform under high temperature, such as textiles and ultrathin PET films. Moreover, as the Au@G electrode is a quasi-2D materials on the surface of water, they could be applied and attached on top of any devices or substrates that were made on curved and rough surfaces.

CHAPTER 7 ULTRATHIN, FLEXIBLE, TRANSFERABLE GRAPHENE-SUPPORTED MICRO-SUPERCAPACITOR

In this chapter, fabrication and performance of the ultrathin, flexible and transferable micro-supercapacitor (μSC) based on graphene/silicon dioxide (SiO_2) bilayer are demonstrated. Highly controllable electrode patterns of the supercapacitor are obtained through applying shadow mask during metal deposition or lithography approach. The topography and performances of the transferred devices are studied in detail, and the advantages of ultrathin, flexible and transferable supercapacitor is discussed.

7.1 Introduction

Wearable and portable electronics have attracted great attentions from researchers and markets nowadays. Importantly, in order to provide all-day comfort to the users, these devices are required to be flexible, thin and light weight. Thus, one of the key challenges of the wearable electronics development is the miniaturization of the energy-storage part, which is conventionally in sandwich structure. To minimize the thickness of energy-storage elements, planar micro-energy-storage devices like μSCs were required. The basic structure of a μSC consists of a positive and a negative electrode positioned next to each other, separated by a pre-assigned gap and ionic conductor electrolyte[208]. Within the planar μSCs with interdigitated electrodes, transportation of electrolyte ions occurs in a two-dimensional way, that separator is no more necessary and this could shorten the ion travel distance. In recent ten years, intensive investigations on planar μSCs with different electrodes design have been done.

Up till now, the micro-scale electrodes were mainly fabricated via lithography[209-211], laser scribing[212-216] and printing[217,218] approaches. However, in order to ease these micro-fabrication processes, all of these μSCs were required to be built on flat and smooth substrates that would not deform under high temperature and high energy beam, which possess thickness of few tens micrometers to millimeters. Although some of the resulted μSCs achieved excellent capacitance performance and retention, the fabrication requirements largely limited the choices of supporting materials of the devices, as well as introducing poor compatibility with some basic materials of wearable and flexible electronics, such as textiles and plastic films.

While graphene, especially the CVD graphene, is well-known for its high tensile strength, flexibility and conductivity, and could be transferred onto arbitrary substrates via dry or wet transfer process with a protective layer (e.g. PMMA or thermal released tape) coated on top[6,7,57,205]. Therefore, in order to realize an ultrathin and transferable supercapacitor based on the monolayer CVD graphene, a nanoscale thick and smooth insulting layer which could be deposited on graphene under precise controlled is essential. Such a layer can separate the conductive graphene layer with the interdigitated electrodes printed on top, thus allowing a highly selective electrochemical deposition of active materials. At the same time, enable the whole structure to be transferred completely through the wet etching process of Cu foil underneath. Therefore, instead of the metal protective layer we deposited on CVD graphene in previous chapters, insulating metal oxide layers were chosen as the modifying agent of the graphene layer.

On the other hand, active materials adopted in the reported μSCs are mainly the carbon-based materials like multi-layer graphene[215,219-221], carbon nanotube (CNT)[222-224] and carbide-derived carbons (CDC)[225,226], or pseudocapacitive materials such as conductive polymer[227-229] and transition metal oxide[230-232]. Among all these materials, cabron based materials obtained satisfactory rate ability as well as the power density, while the pseudocapacitive materials showed a relatively high areal capacitance, since their charge storage mechanism rely on rapid and reversible redox reaction.

In this chapter, by combining mono-to few layer CVD graphene, SiO_2 layer (≦50 nm), patterned Au electrode (≦100 nm) and manganese dioxide (MnO_2) particles, we fabricated an ultrathin (≦180 nm), flexible and transferable μSC. The metal and metal oxide layers of this μSC was fabricated via physical vacuum deposition method, and the active materials were coated on the electrode surface via electochemical deposition, which were simple, efficient, and the thickness of every layer could be well controlled.

To the best of our knowledge, this is the first report of a wet-transferrable SiO_2 layer which possessed a nano-scale thickness assisted by the support of a mono-to-few-layer CVD graphene. Moreover, because of the extraordinary high mechanical strength and flexible nature of CVD graphene, flexible μSCs were realized by simply transferring the graphene/ SiO_2 supported planar electrodes onto suitable substrates. The micro-supercapacitors fabricated via this approach achieved a highest areal capacitance of 814 μF cm^{-2} and a specific capacitance of 21.18 F g^{-1} at scan rate of 10 mV s^{-1}, and obtained satisfactory flexibily when they were transferred and operated on polyimide (PI) tapes and paper substrates. We believed that these results are beneficial for realizing the fabrication of various kinds of wearable, flexible and thin-film electronics on a wide range of substrates in the furture.

7.2 Experimental section

7.2.1 Fabrication of micro-supercapacitor on CVD graphene

CVD-grown graphene sheets grown on Cu foil were supplied by Apex Graphene Technology CO., LTD. A SiO_2 layer (20 nm, 50 nm or 100 nm) was deposited on CVD graphene via plasma enhanced chemical vapor deposition (PECVD), where the Cu face faced down to the tray, and the graphene side was faced up to a gas mixture of 20% silane (SiH_4) and 80% nitrous oxide (N_2O), under 300°C and 0.7 Torr with a deposition rate of 1.2 Å/s. A pair of 100nm thick Au interdigitated electrodes were deposited on the SiO_2 surface through thermal evaporation process at 0.3 nm/s with the aid of a shadow mask.

Electrochemical deposition MnO_2 was carried out with a thermal release tape (TRT) attached to the Cu foil face. The whole deposition process was carried out under a constant current of 2 mA cm^{-2} in a three electrode system at room temperatre, where the reference electrode and counter electrode were silver chloride (Ag/AgCl) and platinum (Pt) foil respectively. The deposition solution consisted of 0.1 M manganese acetate ($MnAc_2$, 98% purity) and 0.1 M sodium sulfate (Na_2SO_4, 99% purity) dissolved in deionized water. After rinsing with deionized water, the TRT was deteched from the Cu foil by heating the samples to 120°C for 1 minute.

7.2.2 Transfer of graphene supported micro-supercapacitor onto target substrates

The basal Cu foil was etched away by placing on a $FeCl_3$ solution for 30 minutes. The graphene/SiO_2 supported electrodes were then rinsed by floating on deionized water, and ready to be attached on the target substrates. In order to avoid mechanical damage to the electrodes as well as minimize the contact resistance during the electrochemical measurements, silver paste was casted along the Au collectors.

7.2.3 Characterizations and electrochemical tests

SEM images of the surface of as-fabricated electrodes were obtained by a Carl Zeiss Ultra 55 scanning electron microscope. The optical transmittance of the SiO_2/CVD graphene was measured by Agilent Cary 7000 UV-Vis spectrometer.

Electrochemical measurements were carried out on an electrochemical station of a Solartron 1,255 frequency response analyzer coupled with Solartron 1,287 electrochemical interface.

Cyclic voltammetry (CV) measurements based on two-electrode and three-electrode system were performed at different scan rates (from 10mV s^{-1} to 50V s^{-1}). For three-electrode system, the tested samples were the 2 cm × 1 cm MnO_2@Au@graphene electrodes transferred onto 125 μm PET films, where 1M Na_2SO_4 was prepared as aqueous electrolyte, Ag/AgCl and Pt foil acted as the reference electrode and counter electrode, respectively. The voltage window of the measurments were set as 0 to 1 V. While for two-electrode system, a gel elecroltye was prepared by mixing 3 g polyvinyl alcohol (PVA) with 30 ml deionized water at 85°C with continuous stirring for 4 hours at first; followed by adding 6.3 g lithium chloride (LiCl) and kept stirring until all the components were fully dissolved. The gel electrolyte was dropped on top of the graphene/SiO_2 supported electrodes which had already been transferred on substrate of interest. The voltage window of the measurments here were set as 0 to 0.8 V.

Galvanostatic charge and discharge (GCD) data and impedance spectra of the planar μSC were also obtained under the two-electrode system. The GCD measurements were carried out at 0.02 mA cm^{-2} to 0.4 mA cm^{-2}, and the impedance data were obtained under a sine wave with 5 mV amplitude over a frequency range of 100 kHz to 0.01 Hz.

7.2.4 Calculations for electrochemical performance

The capacitance C (mF) of the supercapacitor electrodes and the fabricated planar supercapacitors were calculated from the GCD curve by the following equation [219,225]:

$$C = \frac{It}{V} \tag{6}$$

where I (mA) is the discharging current, t (s) is the time for discharge, V(V) is the value of potential window during the discharging process of the devices.
Thus the areal capacitance C_a (mF/cm^{-2}) was calculated by :

$$C_a = \frac{It}{VS} \tag{7}$$

where S (cm^2) is the surface area of the electrodes.

7.3 Results and discussions

7.3.1 Deposition and transfer of SiO_2@CVD graphene bilayer

First of all, via PECVD process, we grew SiO_2 layer on the CVD graphene surface with different thickness to investigate the minimum thickness for the wet transfer of the SiO_2@CVD graphene bilayer. As shown in Figure 7.1 a & c, 50 nm and 100 nm SiO_2

layer deposited on CVD graphene layer were transferred and attached well on the Si wafer. Although some defects were introduced to the graphene films during the PECVD process, as indicated by the decreased D/G peak ratio observed from the Raman spectrum of graphene after SiO_2 deposition (Figure 7.1e), the uniformity of the transferred SiO_2 layers was still satisfying.

On the other hand, the 50 nm and 100 nm SiO_2 films deposited on bare Cu foils which were used for the grown of CVD graphene adopted in the experiments, they could not be transferred as a uniform film via the wet Cu etching process and they peeled off from the Si wafer after they were let dried (Figure 7.1 b & d).

The thinnest SiO_2@CVD graphene bilayer we successfully transferred was 20 nm thick, and the transmittance of the bilayers with different thickness (20 nm, 50 nm and 100 nm) were measured. We found that all of these samples achieved a high transmittance of ~97 % at visible range (~550 nm) (Figure 7.1 f), which is close to the theoretical optical transparency of single-layer graphene (97.7 %) [22,65]. These results therefore suggested the possibility of adopting the SiO_2@CVD graphene bilayer as a basal material of transferable devices which require high optical transparency, such as the photovoltaic devices and light emitting diodes (LEDs).

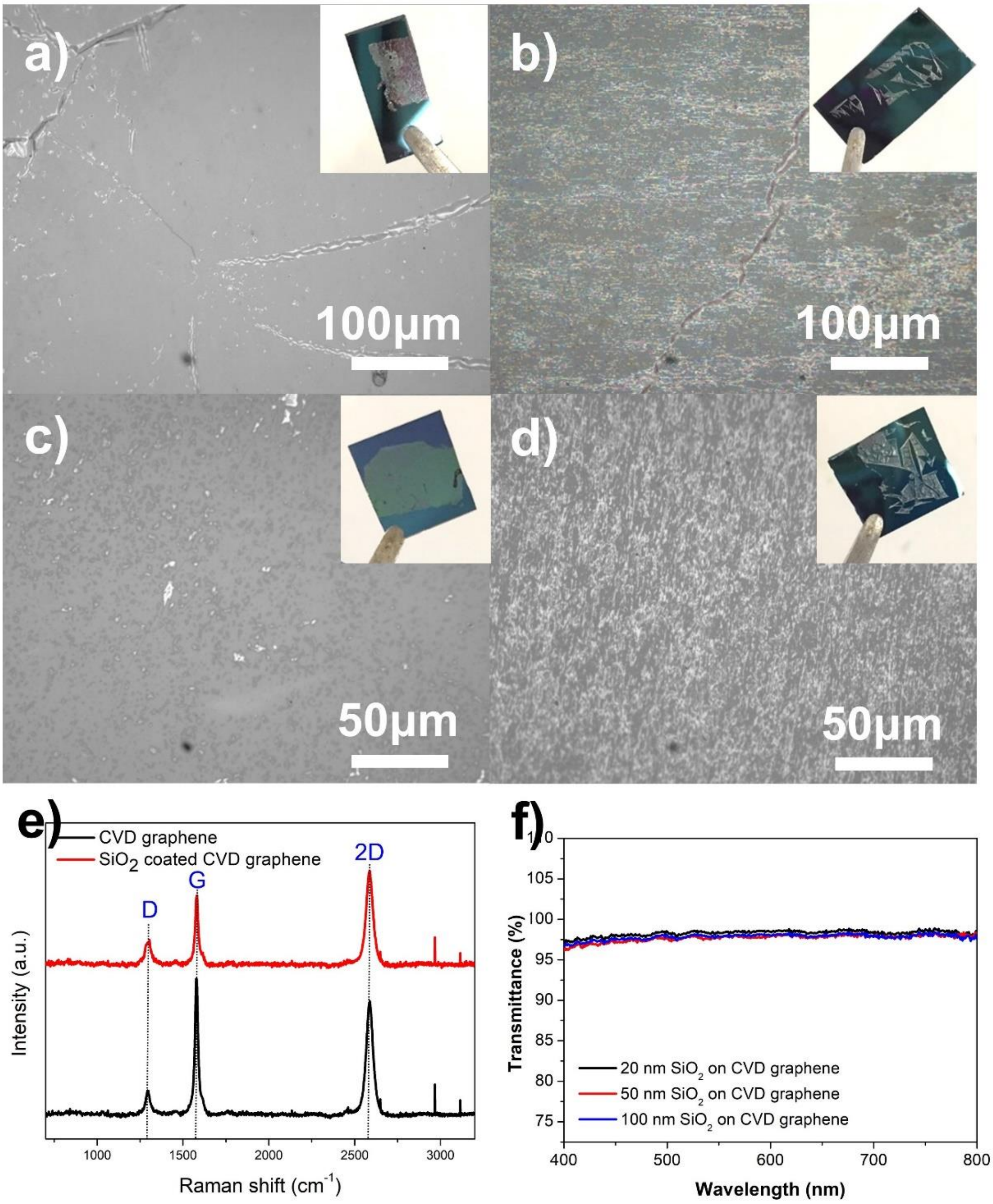

Figure 7.1 Microscopic images of wet-transferred 100nm SiO$_2$ layer **a)** with and **b)** without CVD graphene support on Si wafer; and wet-transferred 50nm SiO$_2$ layer **c)** with and **d)** without CVD graphene support on Si wafer. Inset: Digital images of the corresponding SiO$_2$@CVD graphene bilayer attached on Si wafer. **e)** Raman spectrum of CVD graphene layers before and after the deposition of 50 nm SiO$_2$ layer. **f)** Transmittances of SiO$_2$@CVD graphene bilayer with different thickness transferred on 125 μm PET film.

7.3.2 Fabrication and device structure

As illustrated in Figure 7.2 a, ~50 nm thick SiO_2 film was deposited on top of the CVD graphene as the protective insulating layer via PECVD process, and a pair of interdigitated electrodes was fabricated on top by applying a shadow mask during thermal deposition of Au, or by photolithography method. As the PECVD and thermal deposition process were both operated under high temperature (>300 °C), it is worth to note that graphene is an ideal material to make these fabrication processes well-established due to its stability under high temperature and pressure[67], while many of the flexible substrates such as paper, textiles and few-ten-micron-thick PET films will deform under such conditions.

To complete the fabrication of the μSC electrodes, MnO_2 particles were coated on Au surface via electrochemical deposition. There was a pair of interdigitated electrodes patterns designed and evaporated on the SiO_2 layer, their widths and gaps in-between the electrode-fingers were set as 150 μm and 400 μm respectively.

The as-fabricated μSC electrodes on CVD graphene supported by Cu foil was shown in Figure 7.2 b and c, which was made up of 24 integrated electrodes (i.e. 12 pairs of positive and negative electrodes) that are 8 mm in length. Both of the width and gap in-between the electrode fingers are 150 μm. Figure 7.2 d is the digital image of the graphene/ SiO_2 bilayer supported μSC transferred onto a 125 μm PET substrate, and a satisfactory attachement without cracks and buckles, as well as a excellent completeness of the transferred elecrode fingers could be observed under the mircoscope (figure 7.2 e & f).

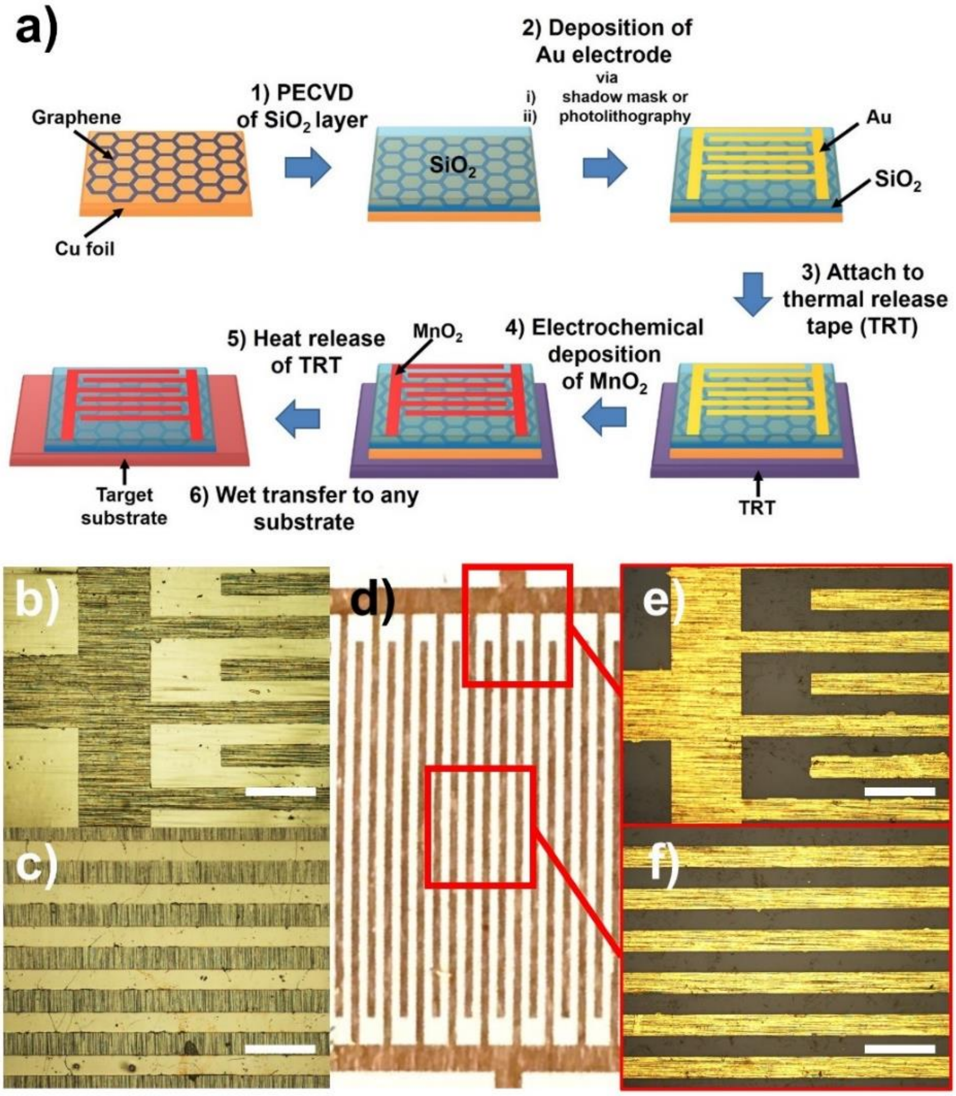

Figure 7.2 a) Fabrication and transfer of the ultrathin, transferable graphene/ SiO_2 bilayer supported µSC. SEM images of **b & c)** microelectrode as-fabricated on SiO2@CVD graphene grown on Cu foil. **d)** Digital image and **e & f)** SEM images of µSC shown in b & c transferred onto 125 µm PET substrate

7.3.3 Electrochemical deposition of MnO_2

In order to obtain the highest possible capacitance of the fabricated µSC, the optimum amount of deposited MnO_2 on the Au electrode was first investigated. From the previous researches involved the deposition of MnO_2 on Au substrates, different amounts of MnO_2 could be deposited by controlling the deposition time under a fixed current density[233,234]. To start with, we simply deposited 100nm Au onto the surface of

50 nm SiO_2 coated-CVD graphene that support by Cu foil. The Au electrodes were then connected to a three electrode system as the working electrode for anodic deposition at room temperature. The current density for MnO_2 deposition was always set as 2 mA cm^{-2}, while the deposition time was varied from 5 s to 900s.

By utilizing the 3-electrode system, capacitances of the whole series of fabricated MnO_2 coated Au electrodes were measured, and the relationship between the areal capacitance of the electrode and the MnO_2 deposition time is shown in Figure 7.3 a. When the deposition time increased from 5 s, the areal capacitance of the eletrodes increase gradually until the deposition time reached 80 s, where the areal capacitance is 14.6 mF cm^{-2}. While the deposition time further increase to >80 s, the areal capacitance started to drop dramatically. The optimum anodic deposition time of MnO_2 was therefore considered as 80 s at 2 mA cm^{-2}.

For further investigating the trend of capacitance changes according to the deposition time, the structure and topography of MnO_2 layer fabricated on Au electrode with different deposition time were observed. From the SEM image figure 7.3 c, we could find that found that MnO_2 particles were deposited through electrochemical successfully, obtaining a flower-like morphology, coated on top of Au electrode as individual particles and islands. While from figure 7.3 d, an Au surface was first observed to be fully covered by MnO_2 particles, thus we could only achieve a uniform MnO_2 layer on the electrode when the electrochemical deposition time is ≥50 s. With further prolonged deposition time, the MnO_2 layers were found to get denser and denser, and bulk MnO_2 clusters were observed when the deposition time is longer than 100s (Figure 7.3 e). And this could be the reason of the capacitances to drop dramatically afterwards. And from figure 7.3 f, we could ensure the SiO_2 substrate allowed a highly selective deposition of MnO_2 on the electrode surface, as no MnO_2 particles were found in the gap between the electrode gaps.

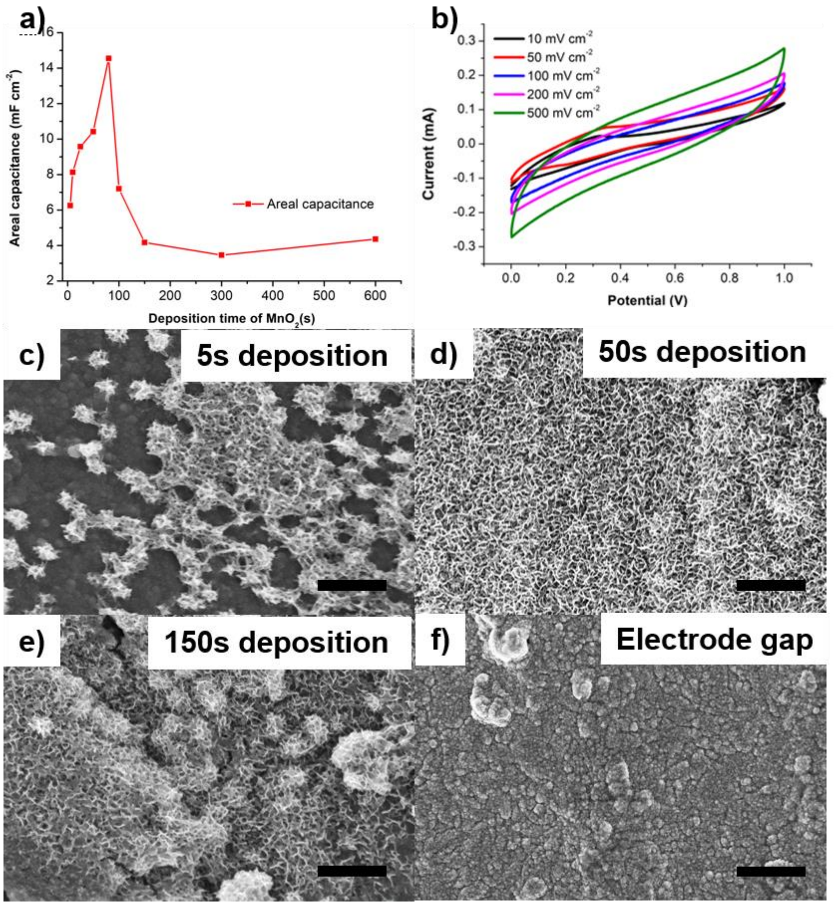

Figure 7.3 a) Corresponding plot showing the relationship of areal capacitance of the electrode versus the electochemical deposition time of MnO_2. **b)** CV curves of the electrode at 80 s-MnO_2-deposition at different scan rates. SEM images of the deposited MnO_2 layer on top of patterned Au electrodes with different electochemical deposition time: **c)** 5 s, **d)** 50 s and **e)** 150 s, and the exposed SiO_2 area in between the electrode fingers. All scale bars equal to 500μm.

7.3.4 Performance of the micro-supercapacitor

Based on the above measurements, all the planar Au μSCs fabricated on the surface of SiO_2@CVD graphene grown on Cu foil were coated with active materials via 80 s MnO_2 deposition. And after etching away the Cu foil underneath the CVD graphene layer, the μSCs were transferred onto 125μm PET film (Figure 7.4 a). After dropping the PVA/LiCl gel electrolyte on top, electrochemical performances of the μSCs were evaluated using 2-electrode system.

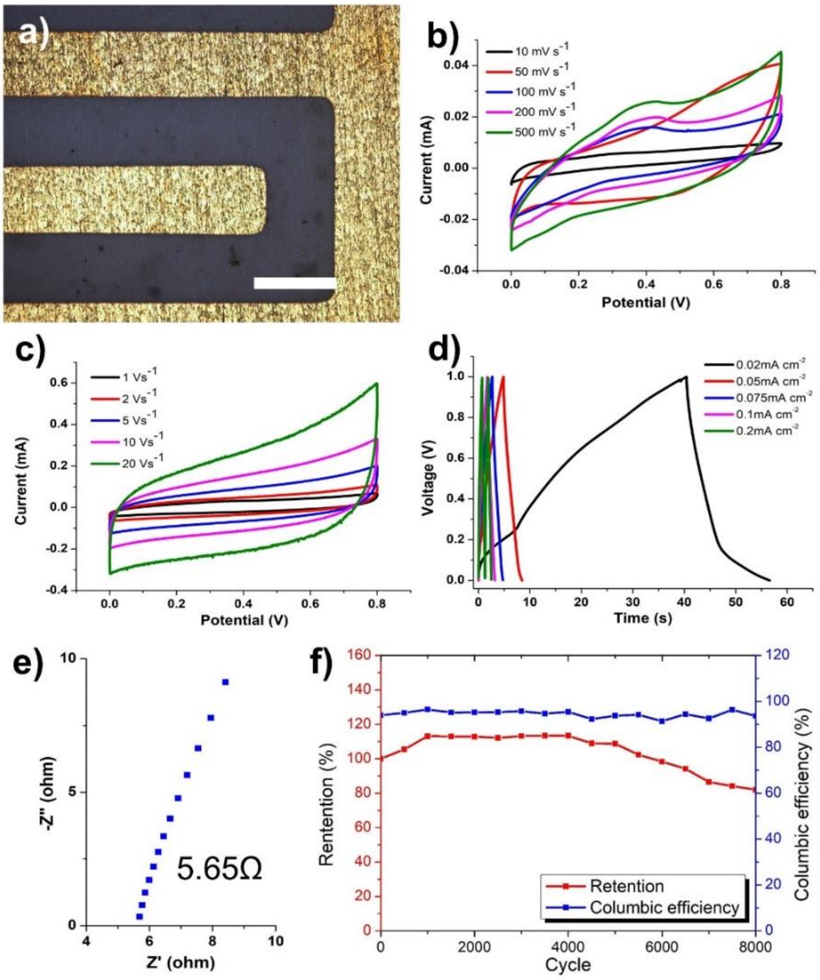

Figure 7.4 CV curves of the micro-supercapacitor at different scan rates **a)** 10 mV s^{-1} to 500 mV s^{-1}, and **b)** 1 V s^{-1} to 20 V s^{-1}. **c)** GCD curves of the supercapacitor device with different current densities (0.02 mA cm^{-2} to 0.2mA cm^{-2}). **d)** Nyquist plot of the micro-supercapacitor. **f)** Cycling performance of the device during 8000 cycles at a scan rate of 0.02 mA cm^{-2}.

Cyclic voltammetry (CV) measurements of µSCs obtaining 400 µm-wide electrode fingers and gaps were conducted with with voltage ranging from 0 to 0.8 V, at scan rates from 10 mV s^{-1} to 20 V s^{-1} as shown in Figure 7.4 b & c. Galvanostatic charge–discharge (GCD) curves with different current densities from 0.02 mA cm^{-2} to 0.2 mA cm^{-2} were also plotted in Fig. 7.4 d. The areal capacitance for the device was found as 295 µF cm^{-2} at scan rate of 10 mV s^{-1}. The electrochemical impedance spectra (EIS) as shown in figure 7.4 e further demonstrate a low internal resistance (~ 5.6 Ω) of the µSC electrode. While from figure 7.4 f, nearly 94% of the initial capacitance value was retained after

6500 cycles and 82% after 8000 cycles when operating under 0.02 mA cm^{-2}, showing a satisfying cycling stability.

In order to improve the capaitance of the μSCs, interdigitated electrodes with finer width and smaller gap distance was adopted. Electrode fingers and gaps width were narrowed down to 150 μm via photolithography process. Although a higher resistance value was obtained (figure 7.5 d), capacitance which is almost 3 times higher was achieved. The areal capacitance for the finer device was found as 814 μF cm^{-2} at scan rate of 10 mV s^{-1}, and it was found to perform well even under high scan rate (up to 50 V s^{-1}) (figure 7.5 a & b), and operated under a wider range of current density (0.08 mA cm^{-2} to 0.4 mA cm^{-2}) as shown in figure 7.5 c.

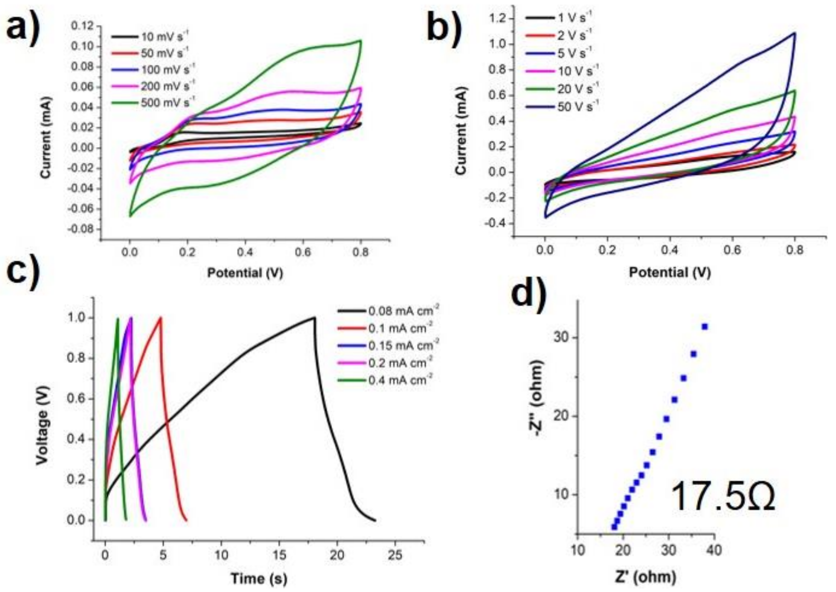

Figure 7.5 CV curves of the finer micro-supercapacitor at different scan rates **a)** 10 mV s^{-1} to 500 mV s^{-1}, and **b)** 1 V s^{-1} to 50 V s^{-1}. **c)** GCD curves of the supercapacitor device with different current densities (0.08 mA cm^{-2} to 0.4mA cm^{-2}). **d)** Nyquist plot of the micro-supercapacitor.

Furthermore, flexibilty of the μSCs were also studied. The μSCs were transferred and attached onto soft substrates including A4 paper, cotton fabric and PI tape (Figure 7.6 a-c). Due to the softness of the substrates, buckles were observed on the transferred μSCs under microscope (Figure 7.6 d), but no serious electrode breakages were observed. These demostrated the tremendous compatibility of this SiO_2/graphene bilayer supported μSC with those common basic materials of wearable electronics, their stability upon bending action were measured. The μSCs (with 400μm width electrode fingers and gaps) was attached on the PI tape, and the capacitance performance was measureed under flat and bending state as shown in Figure 7.6 d and f.

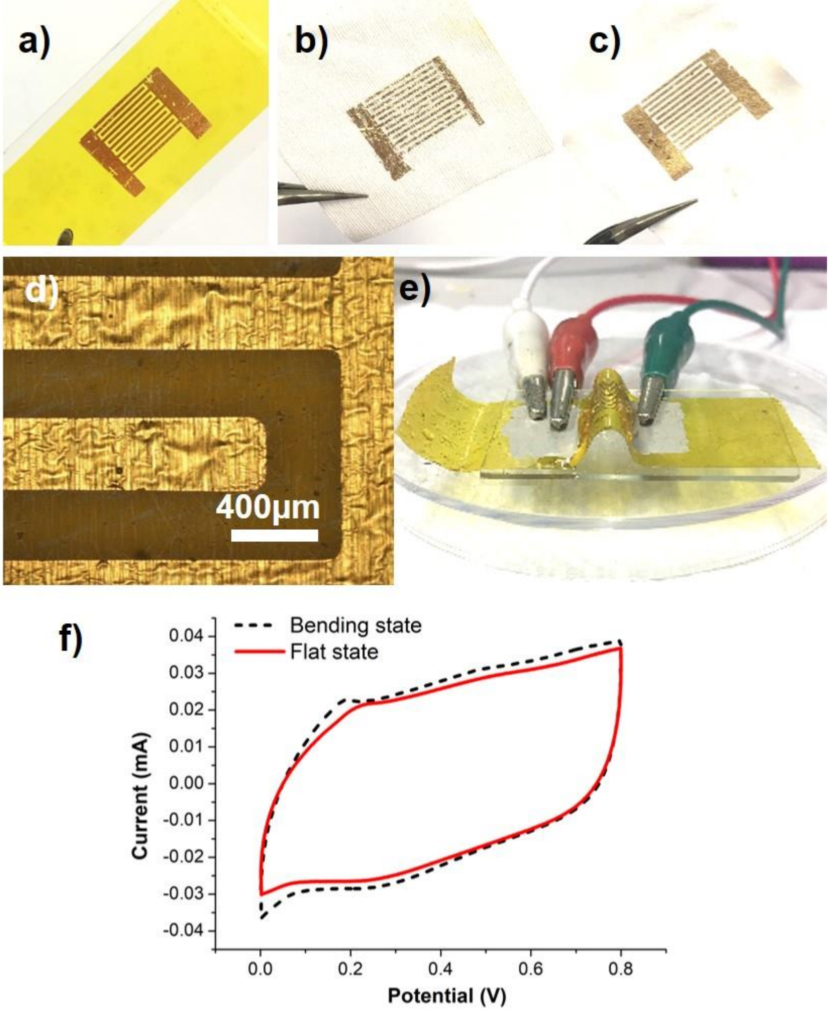

Figure 7.6 Digital images of μSCs transferred onto **a)** PI tape, **b)** cotton fabric and **c)** A4 paper. **d)** SEM image of μSC transferred onto PI tape. **e)** Digital image of the bent μSC on PI tape and **f)** CV curves of the μSC on PI tape at flat and bending state.

The device was measured at 100 mV s^{-1}, and it shown a stable performance under the bending state with bending radius equals to 4 mm at a bending speed of 2.5 mm/s, and the capacitance value of the bended μSC is 9 % higher than the flat state. The enhanced capacitnace could be resulted from more serious buckling occurred along the surface of μSC, which shortened the travel distance of the electrolyte ions.

7.4 Conclusion

We have developed a facile strategy of fabricating an ultrathin, transferrable micro-supercapacitor based on a SiO_2/graphene bilayer. The transferred μSCs obtained an highest areal capacitance of 814 μF cm^{-2} at scan rate of 10 mV s^{-1}, and had shown good cycling stabilities and mechanical flexibilities. More importantly, the μSC was built with less than 200 nm thick, which is one of the thinnest among all the reported supercapacitors.

And based on making use of CVD graphene grown on Cu foil as the building block, high temperature physical deposition processes which allow precise thickness control of metal oxide or metal layers could be carried out without the concern of substrate deformation. Furthermore, they could be transferred onto arbitrary substrates including PET films, tapes, papers and even fabrics.

Other than supercapacitor, the SiO_2/graphene bilayer could definitely a substrate for building any other electronic devices, especially for photovoltaic devices due to their high transparency. We believed that this newly designed strategy could open up a new avenue for fabricating transferable and flexible devices in an efficient way.

CHAPTER 8 CONCLUSIONS AND OUTLOOK

8.1 Conclusions

In this thesis, we had investigated different modifications of graphene films with organic (polymer brushes) and inorganic substances (metal and metal oxide). In order to protect the natural conjugated structure as well as the electronic merits of pristine graphene, only non-covalent modifying approaches were considered. We had studied and discusses about the chemistry and structures of the modified graphene-based materials, as well as applying them in various applications.

In Chapter 4, for widening the applications of chemically inert pure graphene films in the biochemical or electrochemical fields, we utilized the ATRP strategy to enrich the surface functionality of CVD graphene. Via the π-π stacking interaction between basal plane of graphene and the pyrene-group bearing ATRP initiator, four kinds of polymer brushes with different functional group and nature were successfully grafted onto the surface of graphene. These results suggested that desired surface reactivity towards different biological and chemicals substances can be tailored on graphene by this strategy.

In Chapter 5, we deposited 10 – 100 nm Au thin film on CVD graphene grown on Cu foil via simple thermal deposition. We successfully transfer the graphene-supported Au films onto flat and rigid or porous substrates with high integrity, and they attached on the substrates with satisfactory smoothness. Moreover, the mechanical stability and flexibility of the Au@G films were also found to be significantly enhanced than the pure Au films. Also, we are the first to discover the hcp Au structure could occur on the CVD graphene surface by simple physical vacuum deposition.

In Chapter 6, we reported the fabrication process of a transferable, flexible and semi-transparent graphene-based electrodes. Such an electrode was achieved via patterning Au mesh on the CVD graphene, where the Au layer also acted as a protective layer of the graphene film underneath. The as-fabricated Au@G electrode possessed a promising flexibility that the sheet resistance of the mesh (with 5-6μm line width and 2500μm^2 space) only increased for 10% after 1000 bending cycles. Also, satisfactory transmittance to visible light ~92% and sheet resistance ~19.8 Ω were also achieved by the Au@G meshes. Moreover, the transferrable electrode was successfully transferred onto the top of an organic solar cell and worked as the top electrode, while the corresponding FF and PCE reached 55.2% and 2.46%, which are a promising result for semi-transparent organic solar cell.

In Chapter 7, a facile strategy of fabricating transferable ultra-thin devices built on transparent few-ten-nanometer SiO_2 layer was introduced. It was the first report of wet-transferable PECVD SiO_2 layer assisted by mono-to-few layer graphene.
Planar micro-supercapacitors with different patterns were fabricated with a thickness less than 200 nm, and were transferred onto different substrates, including the rigid wafer, PET substrates, fabrics and tape. The highest areal capacitance that could be achieved by the μSCs was 814 μF cm^{-2}.

For the highlights in this thesis, the major contributions of our work on the fabrication of ultrathin functional graphene-based materials falls into three major areas: first, providing the surface properties modifications, such as specific reactivity and wettability which are required in practical sensor and actuator; second, the growth and stabilization of hcp-phased Au structures on CVD graphene surface; third, the realization of transferable, flexible, transparent and lightweight conducting or insulating materials, which are potentially applied in flexible and wearable electronics no matter in large scale or micro-scale. Moreover, these transferable ultrathin graphene-based would definitely open the pathway of fabricating or integrating various devices on more kinds of soft, curved, rough or even fragile materials.

8.2 Outlooks

This research has demonstrated non-covalent modification on CVD graphene with organic polymers, and inorganic layer like metal and metal oxides, which resulted in different ultrathin graphene-supported 2D materials, and their applications were demonstrated. Although several examples of the graphene-supported 2D materials have been illustrated in this thesis, further studies and mass-scale production development based on these graphene-modifying technologies still needed to be conducted in the future:

1. Although mono-to-few layer graphene possess the properties closest to the ideal graphene films as reported in the literature, most of the applications demonstrated with graphene sheets until now were based on GO or rGO. This is due to the relatively high production cost for producing large area and high quality pristine graphene film via epitaxial growth or CVD processes; special handling skills are also needed for such ultra-thin carbon-based materials. In order to realize their applications in the reality, the next step should be investigated more sufficient and low-cost graphene fabrication strategies.
2. We would like to deepen understanding of the following phenomena:

   i) In this research project, only Au and SiO_2 layer were deposited and transferred via graphene-support, a wider range of inorganic layers should be adopted in the future, to investigate the feasibilities and effects of depositing different inorganic layers onto basal plane of graphene. Moreover, to widen the application of graphene-supported transferable inorganic layers.

   ii) hcp Au layer was resulted from thermal deposition on CVD graphene. Hence, depositing metal on CVD graphene layer could be a new strategy for controlling the crystallographic structure of different inorganic layer. On this basis, in aid with the lithography method, we hope to fabricate inorganic layers with well-designed heterogenous crystallographic orientation, through patterning CVD graphene into different structure. We believed that such ultrathin graphene-supported 2D materials, especially for the noble metals with programmed dimension, would be desirable candidates for applications in plasmonic and catalysis field.

REFERENCES

1 Novoselov, K. S. *et al.* Electric Field Effect in Atomically Thin Carbon Films. *Science* **306**, 666-669 (2004).

2 Geim, A. K. & Novoselov, K. S. The rise of graphene. *Nature Materials* **6**, 183-191 (2007).

3 Morozov, S. V. *et al.* Giant intrinsic carrier mobilities in graphene and its bilayer. *Phys. Rev. Lett.* **100**, 4 (2008).

4 Nair, R. R. *et al.* Fine Structure Constant Defines Visual Transparency of Graphene. *Science* **320**, 1308-1308 (2008).

5 Novoselov, K. S. *et al.* Room-Temperature Quantum Hall Effect in Graphene. *Science* **315**, 1379-1379 (2007).

6 Caldwell, J. D. *et al.* Technique for the Dry Transfer of Epitaxial Graphene onto Arbitrary Substrates. *ACS Nano* **4**, 1108-1114 (2010).

7 Lee, Y. *et al.* Wafer-Scale Synthesis and Transfer of Graphene Films. *Nano Letters* **10**, 490-493 (2010).

8 Mattevi, C., Kim, H. & Chhowalla, M. A review of chemical vapour deposition of graphene on copper. *Journal of Materials Chemistry* **21**, 3324-3334 (2011).

9 Suk, J. W. *et al.* Transfer of CVD-Grown Monolayer Graphene onto Arbitrary Substrates. *Acs Nano* **5(9)**, 6916-6924 (2011).

10 Bekyarova, E. *et al.* Chemical Modification of Epitaxial Graphene: Spontaneous Grafting of Aryl Groups. *Journal of the American Chemical Society* **131(4)**, 1336-1337 (2009).

11 Salavagione, H. J., Martinez, G. & Ellis, G. Recent Advances in the Covalent Modification of Graphene With Polymers. *Macromol. Rapid Commun.* **32**, 1771-1789 (2011).

12 Choi, E. Y. *et al.* Noncovalent functionalization of graphene with end-functional polymers. *J. Mater. Chem.* **20**, 1907-1912 (2010).

13 Georgakilas, V. *et al.* Functionalization of Graphene: Covalent and Non-Covalent Approaches, Derivatives and Applications. Chemical Reviews **112(11)**, 6156-6214 (2012).

14 Steenackers, M. *et al.* Polymer Brushes on Graphene. *Journal of the American Chemical Society* **133**, 10490-10498 (2011).

15 Chang, H. *et al.* Thin Film Field-Effect Phototransistors from Bandgap-Tunable, Solution-Processed, Few-Layer Reduced Graphene Oxide Films. *Advanced Materials* **22**, 4872-4876 (2010).

16 Hong, J.-Y. & Jang, J. Micropatterning of graphene sheets: recent advances in techniques and applications. *Journal of Materials Chemistry* **22**, 8179-8191 (2012).

17 Lee, J., Tao, L., Hao, Y., Ruoff, R. S. & Akinwande, D. Embedded-gate graphene transistors for high-mobility detachable flexible nanoelectronics. *Applied Physics Letters* **100**, 152104 (2012).

18 Galagan, Y. *et al.* ITO-free flexible organic solar cells with printed current collecting grids. *Solar Energy Materials and Solar Cells* **95**, 1339-1343 (2011).

19 Kim, Y. H. *et al.* Highly conductive PEDOT: PSS electrode with optimized solvent and thermal post-treatment for ITO-free organic solar cells. *Advanced Functional Materials* **21**, 1076-1081 (2011).

20 Na, S. I., Kim, S. S., Jo, J. & Kim, D. Y. Efficient and flexible ITO-free organic solar cells using highly conductive polymer anodes. *Advanced Materials* **20**, 4061-4067 (2008).

21 Lee, C., Wei, X., Kysar, J. W. & Hone, J. Measurement of the elastic properties and intrinsic strength of monolayer graphene. *Science* **321**, 385-388, doi:10.1126/science.1157996 (2008).

22 Nair, R. R. *et al.* Fine structure constant defines visual transparency of graphene. *Science* **320**, 1308-1308 (2008).

23 Balandin, A. A. *et al.* Superior Thermal Conductivity of Single-Layer Graphene. *Nano Letters* **8**, 902-907 (2008).

24 Eda, G., Fanchini, G. & Chhowalla, M. Large-area ultrathin films of reduced graphene oxide as a transparent and flexible electronic material. *Nat. Nanotechnol.* **3**, 270-274 (2008).

25 Wu, Z. C. *et al.* Transparent, conductive carbon nanotube films. *Science* **305**, 1273-1276 (2004).

26 Zhang, M. *et al.* Strong, transparent, multifunctional, carbon nanotube sheets. *Science* **309**, 1215-1219 (2005).

27 Bourlinos, A. B. *et al.* Graphite oxide: Chemical reduction to graphite and surface modification with primary aliphatic amines and amino acids. *Langmuir* **19**, 6050-6055 (2003).

28 Stankovich, S. *et al.* Synthesis of graphene-based nanosheets via chemical reduction of exfoliated graphite oxide. *Carbon* **45**, 1558-1565 (2007).

29 Novoselov, K. S. *et al.* A roadmap for graphene. *Nature* **490**, 192-200 (2012).

30 Coleman, J. N. *et al.* Two-Dimensional Nanosheets Produced by Liquid Exfoliation of Layered Materials. *Science* **331**, 568-571 (2011).

31 Coleman, J. N. Liquid Exfoliation of Defect-Free Graphene. *Accounts Chem. Res.* **46**, 14-22 (2013).

32 Ciesielski, A. & Samori, P. Graphene via sonication assisted liquid-phase exfoliation. *Chem. Soc. Rev.* **43**, 381-398 (2014).

33 Li, X. *et al.* Large-Area Synthesis of High-Quality and Uniform Graphene Films on Copper Foils. *Science* **324**, 1312 (2009).

34 Obraztsov, A. N. Chemical vapour deposition: Making graphene on a large scale. *Nat Nano* **4**, 212-213 (2009).

35 Reina, A. *et al.* Large Area, Few-Layer Graphene Films on Arbitrary Substrates by Chemical Vapor Deposition. *Nano Letters* **9**, 30-35 (2009).

36 Wang, Y. *et al.* Toward High Throughput Interconvertible Graphane-to-Graphene Growth and Patterning. *ACS Nano* **4**, 6146-6152 (2010).

37 Boyd, D. A. *et al.* Single-step deposition of high-mobility graphene at reduced temperatures. *Nature Communications* **6**, 6620 (2015).

38 Li, X. S. *et al.* Large-Area Synthesis of High-Quality and Uniform Graphene Films on Copper Foils. *Science* **324**, 1312-1314 (2009).

39 Srivastava, A. *et al.* Novel Liquid Precursor-Based Facile Synthesis of Large-Area Continuous, Single, and Few-Layer Graphene Films. *Chem. Mat.* **22**, 3457-3461 (2010).

40 Zhang, B. *et al.* Low-Temperature Chemical Vapor Deposition Growth of Graphene from Toluene on Electropolished Copper Foils. *ACS Nano* **6**, 2471-2476 (2012).

41 Dong, X. C. *et al.* Growth of large-sized graphene thin-films by liquid precursor-based chemical vapor deposition under atmospheric pressure. *Carbon* **49**, 3672-3678 (2011).

42 Li, X. S. *et al.* Graphene Films with Large Domain Size by a Two-Step Chemical Vapor Deposition Process. *Nano Lett.* **10**, 4328-4334 (2010).

43 Vlassiouk, I. *et al.* Large scale atmospheric pressure chemical vapor deposition of graphene. *Carbon* **54**, 58-67 (2013).

44 Sun, Z. Z. *et al.* Growth of graphene from solid carbon sources (vol 468, pg 549, 2010). *Nature* **471**, 124-124 (2011).

45 Eizenberg, M. & Blakely, J. M. CARBON MONOLAYER PHASE CONDENSATION ON NI(111). *Surf. Sci.* **82**, 228-236 (1979).

46 Edwards, R. S. & Coleman, K. S. Graphene Film Growth on Polycrystalline Metals. *Accounts of Chemical Research* **46**, 23-30 (2013).

47 Starr, D. E., Pazhetnov, E. M., Stadnichenko, A. I., Boronin, A. I. & Shaikhutdinov, S. K. Carbon films grown on Pt(111) as supports for model gold catalysts. *Surf. Sci.* **600**, 2688-2695 (2006).

48 Sutter, E., Acharya, D. P., Sadowski, J. T. & Sutter, P. Scanning tunneling microscopy on epitaxial bilayer graphene on ruthenium (0001). *Appl. Phys. Lett.* **94**, 3 (2009).

49 Sutter, P. W., Flege, J. I. & Sutter, E. A. Epitaxial graphene on ruthenium. *Nat. Mater.* **7**, 406-411 (2008).

50 Coraux, J., N'Diaye, A. T., Busse, C. & Michely, T. Structural coherency of graphene on Ir(111). *Nano Lett.* **8**, 565-570 (2008).

51 Bae, S. *et al.* Roll-to-roll production of 30-inch graphene films for transparent electrodes. *Nat. Nanotechnol.* **5**, 574-578 (2010).

52 Lee, J. S., Ahn, H. J., Yoon, J. C. & Jang, J. H. Three-dimensional nano-foam of few-layer graphene grown by CVD for DSSC. *Phys. Chem. Chem. Phys.* **14**, 7938-7943 (2012).

53 Huang, H., Chen, W., Chen, S. & Wee, A. T. S. Bottom-up Growth of Epitaxial Graphene on 6H-SiC(0001). *ACS Nano* **2**, 2513-2518 (2008).

54 Zhao, L. B. *et al.* Generation of Janus alginate hydrogel particles with magnetic anisotropy for cell encapsulation. *Lab on a Chip* **9**, 2981-2986 (2009).

55 Kim, K. S. *et al.* Large-scale pattern growth of graphene films for stretchable transparent electrodes. *Nature* **457**, 706-710 (2009).

56 Gao, L. B. *et al.* Face-to-face transfer of wafer-scale graphene films. *Nature* **505**, 190-194 (2014).

57 Suk, J. W. *et al.* Transfer of CVD-Grown Monolayer Graphene onto Arbitrary Substrates. *ACS Nano* **5**, 6916-6924 (2011).

58 Yang, H. *et al.* Graphene Barristor, a Triode Device with a Gate-Controlled Schottky Barrier. *Science* **336**, 1140 (2012).

59 Yoo, E. *et al.* Large Reversible Li Storage of Graphene Nanosheet Families for Use in Rechargeable Lithium Ion Batteries. *Nano Letters* **8**, 2277-2282 (2008).

60 Yang, S., Feng, X., Ivanovici, S. & Müllen, K. Fabrication of Graphene-Encapsulated Oxide Nanoparticles: Towards High-Performance Anode Materials for Lithium Storage. *Angewandte Chemie International Edition* **49**, 8408-8411 (2010).

61 Wang, H. *et al.* Mn3O4−Graphene Hybrid as a High-Capacity Anode Material for Lithium Ion Batteries. *Journal of the American Chemical Society* **132**, 13978-13980 (2010).

62 Huang, Y., Liang, J. & Chen, Y. An Overview of the Applications of Graphene-Based Materials in Supercapacitors. *Small* **8**, 1805-1834 (2012).

63 Zhang, B., Yu, B., Zhou, F. & Liu, W. Polymer brush stabilized amorphous MnO2 on graphene oxide sheets as novel electrode materials for high

performance supercapacitors. *Journal of Materials Chemistry A* **1**, 8587-8592 (2013).

64 Li, J., Niu, L., Zheng, Z. & Yan, F. Photosensitive Graphene Transistors. *Advanced Materials* **26**, 5239-5273 (2014).

65 Gomez De Arco, L. *et al.* Continuous, Highly Flexible, and Transparent Graphene Films by Chemical Vapor Deposition for Organic Photovoltaics. *ACS Nano* **4**, 2865-2873 (2010).

66 Lee, J.-S., Ahn, H.-J., Yoon, J.-C. & Jang, J.-H. Three-dimensional nano-foam of few-layer graphene grown by CVD for DSSC. *Physical Chemistry Chemical Physics* **14**, 7938-7943 (2012).

67 Wang, X., Zhi, L. & Müllen, K. Transparent, Conductive Graphene Electrodes for Dye-Sensitized Solar Cells. *Nano Letters* **8**, 323-327 (2008).

68 Wang, X. *et al.* Transparent Carbon Films as Electrodes in Organic Solar Cells. *Angewandte Chemie International Edition* **47**, 2990-2992 (2008).

69 Wang, Y., Chen, X., Zhong, Y., Zhu, F. & Loh, K. P. Large area, continuous, few-layered graphene as anodes in organic photovoltaic devices. *Applied Physics Letters* **95**, 063302 (2009).

70 Yan, J., Ye, Q., Wang, X., Yu, B. & Zhou, F. CdS/CdSe quantum dot co-sensitized graphene nanocomposites via polymer brush templated synthesis for potential photovoltaic applications. *Nanoscale* **4**, 2109-2116 (2012).

71 Sim, U. *et al.* N-doped monolayer graphene catalyst on silicon photocathode for hydrogen production. *Energy & Environmental Science* **6**, 3658-3664 (2013).

72 Li, Y. *et al.* MoS2 Nanoparticles Grown on Graphene: An Advanced Catalyst for the Hydrogen Evolution Reaction. *Journal of the American Chemical Society* **133**, 7296-7299 (2011).

73 Schedin, F. *et al.* Detection of individual gas molecules adsorbed on graphene. *Nat Mater* **6**, 652-655 (2007).

74 Shao, Y. *et al.* Graphene Based Electrochemical Sensors and Biosensors: A Review. *Electroanalysis* **22**, 1027-1036 (2010).

75 Marchesan, S., Ballerini, L. & Prato, M. Nanomaterials for stimulating nerve growth. *Science* **356**, 1010 (2017).

76 Zhou, J. *et al.* Ferromagnetism in Semihydrogenated Graphene Sheet. *Nano Letters* **9**, 3867-3870 (2009).

77 Xiang, H. J., Kan, E. J., Wei, S.-H., Gong, X. G. & Whangbo, M. H. Thermodynamically stable single-side hydrogenated graphene. *Physical Review B* **82**, 165425 (2010).

78 Haberer, D. *et al.* Evidence for a New Two-Dimensional C4H-Type Polymer Based on Hydrogenated Graphene. *Advanced Materials* **23**, 4497-4503 (2011).

79 Li, Y. & Chen, Z. Patterned Partially Hydrogenated Graphene (C4H) and Its One-Dimensional Analogues: A Computational Study. *The Journal of Physical Chemistry C* **116**, 4526-4534 (2012).

80 Bahr, J. L. *et al.* Functionalization of Carbon Nanotubes by Electrochemical Reduction of Aryl Diazonium Salts: A Bucky Paper Electrode. *Journal of the American Chemical Society* **123**, 6536-6542 (2001).

81 Yang, M., Zhou, L., Wang, J., Liu, Z. & Liu, Z. Evolutionary Chlorination of Graphene: From Charge-Transfer Complex to Covalent Bonding and Nonbonding. *The Journal of Physical Chemistry C* **116**, 844-850 (2012).

82 Singh, R. & Bester, G. Hydrofluorinated graphene: Two-dimensional analog of polyvinylidene fluoride. *Physical Review B* **84**, 155427 (2011).

83 Li, F. & Li, Y. Band gap modulation of Janus graphene nanosheets by interlayer hydrogen bonding and the external electric field: a computational study. *Journal of Materials Chemistry C* **3**, 3416-3421 (2015).

84 Yang, M. *et al.* Bandgap opening in Janus-type mosaic graphene. *Journal of Applied Physics* **113**, 084313 (2013).

85 Ong, M. T. & Reed, E. J. Engineered Piezoelectricity in Graphene. *ACS Nano* **6**, 1387-1394 (2012).

86 Ong, M. T., Duerloo, K.-A. N. & Reed, E. J. The Effect of Hydrogen and Fluorine Coadsorption on the Piezoelectric Properties of Graphene. *The Journal of Physical Chemistry C* **117**, 3615-3620 (2013).

87 Kim, H. J., Noor-A-Alam, M., Son, J. Y. & Shin, Y.-H. Origin of piezoelectricity in monolayer halogenated graphane piezoelectrics. *Chemical Physics Letters* **603**, 62-66 (2014).

88 Nair, R. R. *et al.* Fluorographene: A Two-Dimensional Counterpart of Teflon. *Small* **6**, 2877-2884 (2010).

89 Wu, J. *et al.* Controlled Chlorine Plasma Reaction for Noninvasive Graphene Doping. *Journal of the American Chemical Society* **133**, 19668-19671 (2011).

90 Zhang, L. *et al.* Janus graphene from asymmetric two-dimensional chemistry. **4**, 1443 (2013).

91 Yuan, L., Li, Z., Yang, J. & Hou, J. G. Diamondization of chemically functionalized graphene and graphene-BN bilayers. *Physical Chemistry Chemical Physics* **14**, 8179-8184 (2012).

92 Barboza, A. P. *et al.* Room-Temperature Compression-Induced Diamondization of Few-Layer Graphene. *Advanced Materials* **23**, 3014-3017 (2011).

93 Delamar, M., Hitmi, R., Pinson, J. & Saveant, J. M. Covalent modification of carbon surfaces by grafting of functionalized aryl radicals produced from electrochemical reduction of diazonium salts. *Journal of the American Chemical Society* **114**, 5883-5884 (1992).

94 Liu, Y.-C. & McCreery, R. L. Reactions of organic monolayers on carbon surfaces observed with unenhanced Raman spectroscopy. *Journal of the American Chemical Society* **117**, 11254-11259 (1995).

95 Kamaras, K., Itkis, M. E., Hu, H., Zhao, B. & Haddon, R. C. Covalent Bond Formation to a Carbon Nanotube Metal. *Science* **301**, 1501 (2003).

96 Bahr, J. L. *et al.* Functionalization of carbon nanotubes by electrochemical reduction of aryl diazonium salts: a bucky paper electrode. *Journal of the American Chemical Society* **123**, 6536-6542 (2001).

97 Sinitskii, A. *et al.* Kinetics of Diazonium Functionalization of Chemically Converted Graphene Nanoribbons. *ACS Nano* **4**, 1949-1954 (2010).

98 Farmer, D. B., Golizadeh-Mojarad, R., Perebeinos, V., Lin, Y. M., Tulevski, G. S., Tsang, J. C., & Avouris, P. Chemical doping and electron− hole conduction asymmetry in graphene devices. Nano letters, 9(1), 388-392 (2008).

99 Bissett, M. A., Takesaki, Y., Tsuji, M. & Ago, H. Increased chemical reactivity achieved by asymmetrical 'Janus' functionalisation of graphene. *RSC Advances* **4**, 52215-52219 (2014).

100 Kim, H., Miura, Y. & Macosko, C. W. Graphene/Polyurethane Nanocomposites for Improved Gas Barrier and Electrical Conductivity. *Chem. Mat.* **22**, 3441-3450 (2010).

101 Barroso-Bujans, F. *et al.* Permanent adsorption of organic solvents in graphite oxide and its effect on the thermal exfoliation. *Carbon* **48**, 1079-1087 (2010).

102 Wei, T. *et al.* Preparation of graphene nanosheet/polymer composites using in situ reduction-extractive dispersion. *Carbon* **47**, 2296-2299 (2009).

103 Sreeprasad, T. S. *et al.* Transparent, Luminescent, Antibacterial and Patternable Film Forming Composites of Graphene Oxide/Reduced Graphene Oxide. *ACS Appl. Mater. Interfaces* **3**, 2643-2654 (2011).

104 Han, T. H. *et al.* Peptide/Graphene Hybrid Assembly into Core/Shell Nanowires. *Adv. Mater.* **22**, 2060 (2010).

105 Rafiee, M. A. *et al.* Enhanced Mechanical Properties of Nanocomposites at Low Graphene Content. *ACS Nano* **3**, 3884-3890 (2009).

106 Ramanathan, T. *et al.* Functionalized graphene sheets for polymer nanocomposites. *Nat. Nanotechnol.* **3**, 327-331 (2008).

107 Liu, J. Q., Yang, W. R., Zareie, H. M., Gooding, J. J. & Davis, T. P. pH-Detachable Polymer Brushes Formed Using Titanium-Diol Coordination Chemistry and Living Radical Polymerization (RAFT). *Macromolecules* **42**, 2931-2939 (2009).

108 Sutter, P., Sadowski, J. T. & Sutter, E. A. Chemistry under Cover: Tuning Metal-Graphene Interaction by Reactive Intercalation. *J. Am. Chem. Soc.* **132**, 8175-8179 (2010).

109 Gao, T. T. *et al.* Noncovalent Microcontact Printing for Grafting Patterned Polymer Brushes on Graphene Films. *Langmuir* **29**, 1054-1060 (2013).

110 Wang, Y., Chen, X. H., Zhong, Y. L., Zhu, F. R. & Loh, K. P. Large area, continuous, few-layered graphene as anodes in organic photovoltaic devices. *Appl. Phys. Lett.* **95**, 3 (2009).

111 Bai, H., Xu, Y. X., Zhao, L., Li, C. & Shi, G. Q. Non-covalent functionalization of graphene sheets by sulfonated polyaniline. *Chem. Commun.* **13**, 1667-1669 (2009).

112 Wei, Q. B., Wang, X. L. & Zhou, F. A versatile macro-initiator with dual functional anchoring groups for surface-initiated atom transfer radical polymerization on various substrates. *Polym. Chem.* **3**, 2129-2137 (2012).

113 Loh, K. P., Bao, Q. L., Ang, P. K. & Yang, J. X. The chemistry of graphene. *J. Mater. Chem.* **20**, 2277-2289 (2010).

114 Wagner, M., Yu, K., Kvarnstrom, C. & Ivaska, A. Synthesis and characterization of electroactive films based on benzo(a)pyrene. *Electrochim. Acta* **56**, 3443-3446 (2011).

115 Xu, Y. X., Bai, H., Lu, G. W., Li, C. & Shi, G. Q. Flexible graphene films via the filtration of water-soluble noncovalent functionalized graphene sheets. *J. Am. Chem. Soc.* **130**, 5856 (2008).

116 Wang, Y., Li, Y. M., Tang, L. H., Lu, J. & Li, J. H. Application of graphene-modified electrode for selective detection of dopamine. *Electrochem. Commun.* **11**, 889-892 (2009).

117 Coletti, C. *et al.* Charge neutrality and band-gap tuning of epitaxial graphene on SiC by molecular doping. *Physical Review B* **81**, 235401 (2010).

118 Stachowiak, T. B., Svec, F. & Fréchet, J. M. J. Patternable Protein Resistant Surfaces for Multifunctional Microfluidic Devices via Surface Hydrophilization of Porous Polymer Monoliths Using Photografting. *Chemistry of Materials* **18**, 5950-5957 (2006).

119 Deng, J. P., Yang, W. T. & Ranby, B. Auto-initiating performance of styrene on surface photografting polymerization. *Macromolecular Rapid Communications* **22**, 535-538 (2001).

120 Steenackers, M., Kuller, A., Stoycheva, S., Grunze, M. & Jordan, R. Structured and Gradient Polymer Brushes from Biphenylthiol Self-Assembled Monolayers by Self-Initiated Photografting and Photopolymerization (SIPGP). *Langmuir* **25**, 2225-2231 (2009).

121 Wu, H., Yi, W., Chen, Z., Wang, H. & Du, Q. Janus graphene oxide nanosheets prepared via Pickering emulsion template. *Carbon* **93**, 473-483 (2015).

122 Barner, L., Davis, T. P., Stenzel, M. H. & Barner-Kowollik, C. Complex macromolecular architectures by reversible addition fragmentation chain transfer chemistry: Theory and practice. *Macromol. Rapid Commun.* **28**, 539-559 (2007).

123 Boyer, C. *et al.* Bioapplications of RAFT Polymerization. *Chem. Rev.* **109**, 5402-5436 (2009).

124 Zhou, N. *et al.* Synthesis of polystyrene end-capped with pyrene via reversible additionfragmentation chain transfer polymerization. *Polymer* **48**, 1255-1260 (2007).

125 Meuer, S., Braun, L. & Zentel, R. Solubilisation of multi walled carbon nanotubes by alpha-pyrene functionalised PMMA and their liquid crystalline self-organisation. *Chem. Commun.*, 3166-3168 (2008).

126 Xu, J. T., Tao, L., Boyer, C., Lowe, A. B. & Davis, T. P. Facile Access to Polymeric Vesicular Nanostructures: Remarkable omega-End group Effects in Cholesterol and Pyrene Functional (Co)Polymers. *Macromolecules* **44**, 299-312 (2011).

127 Meuer, S., Braun, L., Schilling, T. & Zentel, R. alpha-Pyrene polymer functionalized multiwalled carbon nanotubes: Solubility, stability and depletion phenomena. *Polymer* **50**, 154-160 (2009).

128 Liu, J. Q. *et al.* Thermosensitive Graphene Nanocomposites Formed Using Pyrene-Terminal Polymers Made by RAFT Polymerization. *J. Polym. Sci. Pol. Chem.* **48**, 425-433 (2010).

129 Xiao, P. *et al.* A microcontact printing induced supramolecular self-assembled photoactive surface for patterning polymer brushes. *Chemical Communications* **49**, 11167-11169 (2013).

130 Kim, B. H. *et al.* Mussel-Inspired Block Copolymer Lithography for Low Surface Energy Materials of Teflon, Graphene, and Gold. *Advanced Materials* **23**, 5618-5622 (2011).

131 Ren, Y. *et al.* Controlling the electrical transport properties of graphene by in situ metal deposition. *Applied Physics Letters* **97**, 053107 (2010).

132 Zhou, H. *et al.* Thickness-Dependent Morphologies of Gold on N-Layer Graphenes. *Journal of the American Chemical Society* **132**, 944-946 (2010).

133 Li, Y. *et al.* in *2014 International Conference on Manipulation, Manufacturing and Measurement on the Nanoscale (3M-NANO).* 117-121 (2014).

134 Sun, S. *et al.* Single-atom Catalysis Using Pt/Graphene Achieved through Atomic Layer Deposition. *Scientific Reports* **3**, 1775 (2013).

135 Wang, X., Tabakman, S. M. & Dai, H. Atomic Layer Deposition of Metal Oxides on Pristine and Functionalized Graphene. *Journal of the American Chemical Society* **130**, 8152-8153 (2008).

136 George, S. M. Atomic Layer Deposition: An Overview. *Chemical Reviews* **110**, 111-131 (2010).

137 Yu, D., Nagelli, E., Naik, R. & Dai, L. Asymmetrically Functionalized Graphene for Photodependent Diode Rectifying Behavior. *Angewandte Chemie International Edition* **50**, 6575-6578 (2011).

138 Toth, P. S., Velický, M., Ramasse, Q. M., Kepaptsoglou, D. M. & Dryfe, R. A. W. Symmetric and Asymmetric Decoration of Graphene: Bimetal-Graphene Sandwiches. *Advanced Functional Materials* **25**, 2899-2909 (2015).

139 Gutes, A. *et al.* Graphene decoration with metal nanoparticles: Towards easy integration for sensing applications. *Nanoscale* **4**, 438-440 (2012).

140 Compton, O. C. & Nguyen, S. T. Graphene Oxide, Highly Reduced Graphene Oxide, and Graphene: Versatile Building Blocks for Carbon-Based Materials. *Small* **6**, 711-723 (2010).

141 Zhu, Y. *et al.* Graphene and Graphene Oxide: Synthesis, Properties, and Applications. *Advanced Materials* **22**, 3906-3924 (2010).

142 Xiao, P. *et al.* Micro-contact printing of graphene oxide nanosheets for fabricating patterned polymer brushes. *Chemical Communications* **50**, 7103-7106 (2014).

143 Han, D. et al. Polymer brush functionalized Janus graphene oxide/chitosan hybrid membranes. RSC Advances 4, 22759-22762 (2014).

144 Xiao, P. *et al.* 2D Janus Hybrid Materials of Polymer-Grafted Carbon Nanotube/Graphene Oxide Thin Film as Flexible, Miniature Electric Carpet. *Advanced Functional Materials* **25**, 2428-2435 (2015).

145 Wu, S. *et al.* Electrochemical Deposition of Semiconductor Oxides on Reduced Graphene Oxide-Based Flexible, Transparent, and Conductive Electrodes. *The Journal of Physical Chemistry C* **114**, 11816-11821 (2010).

146 Zhang, L. *et al.* Macroscopic Ultrathin Film as Bio-Inspired Interfacial Reactor for Fabricating 2D Freestanding Janus CNTs/AuNPs Hybrid Nanosheets with Enhanced Electrical Performance. *Advanced Materials Interfaces* **3**, 1600170 (2016).

147 McGrail, B. T. *et al.* Selective mono-facial modification of graphene oxide nanosheets in suspension. *Chemical Communications* **52**, 288-291, (2016).

148 Wang, Y. *et al.* Fluorinated Graphene for Promoting Neuro-Induction of Stem Cells. *Advanced Materials* **24**, 4285-4290 (2012).

149 Singh, M. *et al.* Noncovalently Functionalized Monolayer Graphene for Sensitivity Enhancement of Surface Plasmon Resonance Immunosensors. *Journal of the American Chemical Society* **137**, 2800-2803 (2015).

150 Liu, G., Ahsan, S., Khitun, A. G., Lake, R. K. & Balandin, A. A. Graphene-based non-Boolean logic circuits. *Journal of Applied Physics* **114**, 154310 (2013).

151 Sarkar, S. *et al.* Organometallic Hexahapto Functionalization of Single Layer Graphene as a Route to High Mobility Graphene Devices. *Advanced Materials* **25**, 1131-1136 (2013).

152 Yang, Y. *et al.* Ultrafine Graphene Nanomesh with Large On/Off Ratio for High-Performance Flexible Biosensors. *Advanced Functional Materials* **27**, 1604096 (2017).

153 Xie, X. *et al.* An Asymmetrically Surface-Modified Graphene Film Electrochemical Actuator. *ACS Nano* **4**, 6050-6054 (2010).

154 Mu, J. *et al.* Origami-inspired active graphene-based paper for programmable instant self-folding walking devices. *Science Advances* **1** (2015).

155 Ding, B., Li, C., Miyauchi, Y., Kuwaki, O., & Shiratori, S. Formation of novel 2D polymer nanowebs via electrospinning. *Nanotechnology*, **17(15)**, 3685 (2006).

156 Zhuang, T. Z. *et al.* Rational integration of polypropylene/graphene oxide/nafion as ternary-layered separator to retard the shuttle of polysulfides for lithium–sulfur batteries. *Small* **12**, 381-389 (2016).

157 Suzana P. Nunes, Ali Reza Behzad, Bobby Hooghan, Rachid Sougrat, Madhavan Karunakaran, Neelakanda Pradeep, Ulla Vainio, and Klaus-Viktor Peinemann. Switchable pH-responsive polymeric membranes prepared via block copolymer micelle assembly. *ACS nano,* **5(5)**, 3516-3522 (2011).

158 Zhou, G. *et al.* A Flexible Sulfur-Graphene-Polypropylene Separator Integrated Electrode for Advanced Li–S Batteries. *Advanced Materials* **27**, 641-647 (2015).

159 Edmondson, S. & Huck, W. T. S. Quasi-2D polymer objects from patterned, crosslinked polymer brushes. *Adv. Mater.* **16**, 1327 (2004).

160 Stroock, A. D., Kane, R. S., Weck, M., Metallo, S. J. & Whitesides, G. M. Synthesis of free-standing quasi-two-dimensional polymers. *Langmuir* **19**, 2466-2472 (2003).

161 Amin, I. *et al.* Polymer Carpets. *Small* **6**, 1623-1630 (2010).

162 Mattsson, J., Forrest, J. A. & Börjesson, L. Quantifying glass transition behavior in ultrathin free-standing polymer films. *Physical Review E* **62**, 5187-5200 (2000).

163 Ionov, L. Soft microorigami: self-folding polymer films. *Soft Matter* **7**, 6786-6791 (2011).

164 Ohm, C. & Ober, C. K. From surface coatings to polymer nanofilms: lifting off polymer brushes. *RSC Adv.* **3**, 18482-18488 (2013).

165 Lynn, D. M. Layers of opportunity: nanostructured polymer assemblies for the delivery of macromolecular therapeutics. *Soft Matter* **2**, 269-273 (2006).

166 Srivastava, S. & Kotov, N. A. Composite Layer-by-Layer (LBL) Assembly with Inorganic Nanoparticles and Nanowires. *Accounts Chem. Res.* **41**, 1831-1841, (2008).

167 Wohnrath, K. *et al.* Langmuir and Langmuir-Blodgett films containing a porphyrin-ruthenium complex. *J. Nanosci. Nanotechnol.* **5**, 909-916 (2005).

168 McQuade, D. T., Pullen, A. E. & Swager, T. M. Conjugated polymer-based chemical sensors. *Chem. Rev.* **100**, 2537-2574 (2000).

169 Brinker, C. J., Lu, Y. F., Sellinger, A. & Fan, H. Y. Evaporation-induced self-assembly: Nanostructures made easy. *Adv. Mater.* **11**, 579 (1999).

170 Park, M., Harrison, C., Chaikin, P. M., Register, R. A. & Adamson, D. H. Block copolymer lithography: Periodic arrays of similar to 10(11) holes in 1 square centimeter. *Science* **276**, 1401-1404 (1997).

171 Colfen, H. & Mann, S. Higher-order organization by mesoscale self-assembly and transformation of hybrid nanostructures. *Angew. Chem.-Int. Edit.* **42**, 2350-2365 (2003).

172 Jeong, B. H. *et al.* Interfacial polymerization of thin film nanocomposites: A new concept for reverse osmosis membranes. *J. Membr. Sci.* **294**, 1-7 (2007).

173 Freger, V. Nanoscale heterogeneity of polyamide membranes formed by interfacial polymerization. *Langmuir* **19**, 4791-4797 (2003).

174 Kemperman, A. J. B., Rolevink, H. H. M., Bargeman, D., van den Boomgaard, T. & Strathmann, H. Stabilization of supported liquid membranes by interfacial polymerization top layers. *J. Membr. Sci.* **138**, 43-55 (1998).

175 Frank, C. W. *et al.* Structure in thin and ultrathin spin-cast polymer films. *Science* **273**, 912-915 (1996).

176 Walheim, S., Boltau, M., Mlynek, J., Krausch, G. & Steiner, U. Structure formation via polymer demixing in spin-cast films. *Macromolecules* **30**, 4995-5003 (1997).

177 Gao, T. *et al.* Noncovalent Microcontact Printing for Grafting Patterned Polymer Brushes on Graphene Films. *Langmuir* **29**, 1054-1060 (2013).

178 Xu, Y., Bai, H., Lu, G., Li, C. & Shi, G. Flexible Graphene Films via the Filtration of Water-Soluble Noncovalent Functionalized Graphene Sheets. *Journal of the American Chemical Society* **130**, 5856-5857 (2008).

179 Tan, K. Y. *et al.* Decoupling geometrical and chemical cues directing epidermal stem cell fate on polymer brush-based cell micro-patterns. *Integrative Biology* **5**, 899-910 (2013).

180 Friis, J. E. *et al.* Hydrophilic Polymer Brush Layers on Stainless Steel Using Multilayered ATRP Initiator Layer. *ACS applied materials & interfaces* **8**, 30616-30627 (2016).

181 Mandal, T. K., Fleming, M. S. & Walt, D. R. Preparation of polymer coated gold nanoparticles by surface-confined living radical polymerization at ambient temperature. *Nano Lett.* **2**, 3-7 (2002).

182 Sutandar, P., Ahn, D. J. & Franses, E. I. FTIR ATR ANALYSIS FOR MICROSTRUCTURE AND WATER-UPTAKE IN POLY(METHYL METHACRYLATE) SPIN CAST AND LANGMUIR-BLODGETT THIN-FILMS. *Macromolecules* **27**, 7316-7328 (1994).

183 Lian, X. M., Wu, D. X., Song, X. H. & Zhao, H. Y. Synthesis and Self-Assembly of Amphiphilic Asymmetric Macromolecular Brushes. *Macromolecules* **43**, 7434-7445 (2010).

184 Barbey, R. & Klok, H. A. Room Temperature, Aqueous Post-Polymerization Modification of Glycidyl Methacrylate-Containing Polymer Brushes Prepared via Surface-Initiated Atom Transfer Radical Polymerization. *Langmuir* **26**, 18219-18230 (2010).

185 Li, X. *et al.* Block Copolymer Modified Surfaces for Conjugation of Biomacromolecules with Control of Quantity and Activity. *Langmuir* **29**, 1122-1128 (2013).

186 Tugulu, S., Arnold, A., Sielaff, I., Johnsson, K. & Klok, H. A. Protein-functionalized polymer brushes. *Biomacromolecules* **6**, 1602-1607 (2005).

187 van Poll, M. L., Zhou, F., Ramstedt, M., Hu, L. & Huck, W. T. S. A self-assembly approach to chemical micropatterning of poly(dimethylsiloxane). *Angew. Chem.-Int. Edit.* **46**, 6634-6637 (2007).

188 Combellas, C., Kanoufi, F., Sanjuan, S., Slim, C. & Tran, Y. Electrochemical and Spectroscopic Investigation of Counterions Exchange in Polyelectrolyte Brushes. *Langmuir* **25**, 5360-5370 (2009).

189 Azzaroni, O., Moya, S., Farhan, T., Brown, A. A. & Huck, W. T. S. Switching the properties of polyelectrolyte brushes via "Hydrophobic collapse". *Macromolecules* **38**, 10192-10199 (2005).

190 Pirri, G., Chiari, M., Damin, F. & Meo, A. Microarray glass slides coated with block copolymer brushes obtained by reversible addition chain-transfer polymerization. *Anal. Chem.* **78**, 3118-3124 (2006).

191 Xie, Z. *et al.* Massively Parallel Patterning of Complex 2D and 3D Functional Polymer Brushes by Polymer Pen Lithography. ACS Appl. Mater. Interfaces, **6(15)**, 11955-11964 (2014)

192 Bae, S. *et al.* Roll-to-roll production of 30-inch graphene films for transparent electrodes. *Nature Nanotechnology* **5**, 574 (2010).

193 Zhang, H., Tang, D., Zhao, L., Bao, Q. & Loh, K. Large energy mode locking of an erbium-doped fiber laser with atomic layer graphene. *Optics Express* **17**, 17630-17635 (2009).

194 Hsu, C.-L. *et al.* Layer-by-Layer Graphene/TCNQ Stacked Films as Conducting Anodes for Organic Solar Cells. *ACS Nano* **6**, 5031-5039 (2012).

195 Choi, J. *et al.* Enhanced performance of graphene by using gold film for transfer and masking process. *Current Applied Physics* **14**, 1045-1050 (2014).

196 Kim, K.-S. *et al.* Chemical Vapor Deposition-Grown Graphene: The Thinnest Solid Lubricant. *ACS Nano* **5**, 5107-5114 (2011).

197 Berman, D., Erdemir, A. & Sumant, A. V. Graphene: a new emerging lubricant. *Materials Today* **17**, 31-42 (2014).

198 Arshad, Muhammad Shahid, Špela Trafela, Kristina Žužek Rožman, Janez Kovač, Petar Djinović, and Albin Pintar. Determination of Schottky barrier height and enhanced photoelectron generation in novel plasmonic immobilized multisegmented (Au/TiO2) nanorod arrays (NRAs) suitable for solar energy conversion applications. Journal of Materials Chemistry C **5(40)**: 10509-10516 (2017)

199 Luo, Zhiqiang, Sanhua Lim, Zhiqun Tian, Jingzhi Shang, Linfei Lai, Brian MacDonald, Chao Fu, Zexiang Shen, Ting Yu, and Jianyi Lin. Pyridinic N doped graphene: synthesis, electronic structure, and electrocatalytic property. Journal of Materials Chemistry **21(22),** 8038-8044 (2011)

200 Emmott, C. J., Urbina, A. & Nelson, J. Environmental and economic assessment of ITO-free electrodes for organic solar cells. *Solar Energy Materials and Solar Cells* **97**, 14-21 (2012).

201 Seo, J. H. *et al.* Cold Isostatic-Pressured Silver Nanowire Electrodes for Flexible Organic Solar Cells via Room-Temperature Processes. *Advanced Materials* **29** (2017).

202 Leem, D. S. *et al.* Efficient organic solar cells with solution-processed silver nanowire electrodes. *Advanced Materials* **23**, 4371-4375 (2011).

203 Koga, H. *et al.* Uniformly connected conductive networks on cellulose nanofiber paper for transparent paper electronics. *NPG Asia Materials* **6**, e93 (2014).

204 Hösel, M., Søndergaard, R. R., Angmo, D. & Krebs, F. C. Comparison of Fast Roll-to-Roll Flexographic, Inkjet, Flatbed, and Rotary Screen Printing of Metal Back Electrodes for Polymer Solar Cells. *Advanced engineering materials* **15**, 995-1001 (2013).

205 Bae, S. *et al.* Roll-to-roll production of 30-inch graphene films for transparent electrodes. *Nature Nanotechnology* **5**, 574-578 (2010).

206 Kim, K. S. *et al.* Large-scale pattern growth of graphene films for stretchable transparent electrodes. *Nature* **457**, 706 (2009).

207 Li, X. S. *et al.* Transfer of Large-Area Graphene Films for High-Performance Transparent Conductive Electrodes. *Nano Letters* **9**, 4359-4363 (2009).

208 Kyeremateng, N. A., Brousse, T. & Pech, D. Microsupercapacitors as miniaturized energy-storage components for on-chip electronics. *Nature nanotechnology* **12**, 7 (2017).

209 Tian, X. *et al.* Arbitrary shape engineerable spiral micropseudocapacitors with ultrahigh energy and power densities. *Advanced Materials* **27**, 7476-7482 (2015).

210 Qi, D. *et al.* Suspended wavy graphene microribbons for highly stretchable microsupercapacitors. *Advanced Materials* **27**, 5559-5566 (2015).

211 Kim, S. K., Koo, H. J., Lee, A. & Braun, P. V. Selective Wetting-Induced Micro-Electrode Patterning for Flexible Micro-Supercapacitors. *Advanced Materials* **26**, 5108-5112 (2014).

212 Huang, H.-C., Chung, C.-J., Hsieh, C.-T., Kuo, P.-L. & Teng, H. Laser fabrication of all-solid-state microsupercapacitors with ultrahigh energy and power based on hierarchical pore carbon. *Nano Energy* **21**, 90-105 (2016).

213 Cai, J., Lv, C. & Watanabe, A. Cost-effective fabrication of high-performance flexible all-solid-state carbon micro-supercapacitors by blue-violet laser direct writing and further surface treatment. *Journal of Materials Chemistry A* **4**, 1671-1679 (2016).

214 Lobo, D. E., Banerjee, P. C., Easton, C. D. & Majumder, M. Miniaturized supercapacitors: Focused ion beam reduced graphene oxide supercapacitors with enhanced performance metrics. *Advanced Energy Materials* **5** (2015).

215 El-Kady, M. F., Strong, V., Dubin, S. & Kaner, R. B. Laser scribing of high-performance and flexible graphene-based electrochemical capacitors. *Science* **335**, 1326-1330 (2012).

216 Cao, L. *et al.* Direct Laser-Patterned Micro-Supercapacitors from Paintable MoS2 Films. *Small* **9**, 2905-2910 (2013).

217 Liu, Z. *et al.* Ultraflexible in-plane micro-supercapacitors by direct printing of solution-processable electrochemically exfoliated graphene. *Advanced Materials* **28**, 2217-2222 (2016).

218 Wang, Y. *et al.* Printed all-solid flexible microsupercapacitors: towards the general route for high energy storage devices. *Nanotechnology* **25**, 094010 (2014).

219 El-Kady, M. F. & Kaner, R. B. Scalable fabrication of high-power graphene micro-supercapacitors for flexible and on-chip energy storage. *Nature communications* **4**, ncomms2446 (2013).

220 Yoo, J. J. *et al.* Ultrathin planar graphene supercapacitors. *Nano letters* **11**, 1423-1427 (2011).

221 Niu, Z. *et al.* All-solid-state flexible ultrathin micro-supercapacitors based on graphene. *Advanced Materials* **25**, 4035-4042 (2013).

222 Hsia, B. *et al.* Highly flexible, all solid-state micro-supercapacitors from vertically aligned carbon nanotubes. *Nanotechnology* **25**, 055401 (2014).

223 Lin, J. *et al.* 3-dimensional graphene carbon nanotube carpet-based microsupercapacitors with high electrochemical performance. *Nano letters* **13**, 72-78 (2012).

224 Kim, D., Shin, G., Kang, Y. J., Kim, W. & Ha, J. S. Fabrication of a stretchable solid-state micro-supercapacitor array. *Acs Nano* **7**, 7975-7982 (2013).

225 Chmiola, J., Largeot, C., Taberna, P.-L., Simon, P. & Gogotsi, Y. Monolithic carbide-derived carbon films for micro-supercapacitors. *Science* **328**, 480-483 (2010).

226 Huang, P. *et al.* Micro-supercapacitors from carbide derived carbon (CDC) films on silicon chips. *Journal of Power Sources* **225**, 240-244 (2013).

227 Zhu, M. *et al.* A Highly Durable, Transferable, and Substrate-Versatile High-Performance All-Polymer Micro-Supercapacitor with Plug-and-Play Function. *Advanced Materials* **29** (2017).

228 Liu, Z. *et al.* High Power In-Plane Micro-Supercapacitors Based on Mesoporous Polyaniline Patterned Graphene. *Small* **13** (2017).

229 Wang, K. *et al.* An All-Solid-State Flexible Micro-supercapacitor on a Chip. *Advanced Energy Materials* **1**, 1068-1072 (2011).

230 Peng, L. *et al.* Ultrathin two-dimensional MnO2/graphene hybrid nanostructures for high-performance, flexible planar supercapacitors. *Nano letters* **13**, 2151-2157 (2013).

231 Liu, W., Lu, C., Wang, X., Tay, R. Y. & Tay, B. K. High-performance microsupercapacitors based on two-dimensional graphene/manganese dioxide/silver nanowire ternary hybrid film. *ACS nano* **9**, 1528-1542 (2015).

232 Xue, M. *et al.* Microfluidic etching for fabrication of flexible and all-solid-state micro supercapacitor based on MnO 2 nanoparticles. *Nanoscale* **3**, 2703-2708 (2011).

233. Gao, Y. *et al.* Highly flexible and transferable supercapacitors with ordered three-dimensional MnO $_2$/Au/MnO $_2$ nanospike arrays. *Journal of Materials Chemistry A* **3**, 10199-10204 (2015).

234. Xu, H. *et al.* Flexible fiber-shaped supercapacitors based on hierarchically nanostructured composite electrodes. *Nano Research* **8**, 1148-1158 (2015).